TITLE: **INVESTIGATION OF WO_3-BASED H_2S SENSOR MATERIALS FOR COAL GASIFICATION SYSTEMS**

TYPE OF REPORT: Final Scientific/Technical Report

GRANT NO.: DENT0008022

AUTHOR: **Dr. Felicia S. Manciu (PI)**
Department of Physics
Tel: 915 747 8472; Fax 915 747 5447;
E-mail: fsmanciu@utep.edu

Dr. Chintalapalle V. Ramana (Co-PI)
Department of Mechanical Engineering
Tel: 915 747 8630; Fax 915 747 8036
E-mail: rvchintalapalle@utep.edu

INSTITUTION: The University of Texas at El Paso
500 West University Ave.
El Paso, TX 79968-0521

PHONE NO.: (915) 747 8472

FAX NO.: (915) 747 5447

E-MAIL: fsmanciu@utep.edu

DOE PROJECT MANAGER: **Richard J. Dunst**
Phone: 412-386-6694
E-mail: Richard.Dunst@netl.doe.gov

PERIOD OF PERFORMANCE: January 15, 2009 – December 15,2013

DATE: January 20, 2014

DISCLAMER

ABSTRACT

The aim of this project was to engineer the materials studied to enhance the so-called 3S criteria: Sensitivity, Selectivity, and Stability, by using the advantage of controlling structure and properties at nanometer dimensions. It targeted sensor materials that are able to detect poisonous gases resulting from coal-gasification processes, especially sulfur containing emissions. Research findings based on this award demonstrate that doping tungsten oxide (WO_3) with a small amount of Ti (e.g. 5% in our work) results in a new material that has a higher structural symmetry (e.g. tetragonal morphology) as well as narrower crystalline particle size distribution. As high quality materials with excellent ordered structure and narrower particle-size distributions (which can also withstand high-temperature technological environments such as those encountered in furnaces and coal gasification systems without their structure being affected by phase transformations) are needed for developing new, more sensitive sensor materials, W-Ti-O thin films grown by RF sputtering are valuable candidates for such roles. It is well known that pure WO_3 will change its structure at elevated temperatures. Our work indicates that, Ti doping not only increases the stability of the resultant material by promoting structural phase modifications, but also increases its sensitivity by increasing the effective surface area exposed to the poisonous gas (fine microstructure and uniform distribution were observed).

TABLE OF CONTENTS

EXECUTIVE SUMMARY

The overall efforts proposed were to develop high-quality new sensor materials for achieving improved response time, controlled microstructure for long-term stability, and narrow particle size distribution for improved sensor characteristics and performance. The aim was to identify methods to enhance the so-called 3S criteria: sensitivity, selectivity, and stability, by utilizing the advantages of controlling structure and properties at nanometer dimensions.

The milestones of the proposed research were: (1) to study the characteristics of undoped WO_3 thin films synthesized by RF sputtering, (2) to explore the stabilization and structural modifications of Ti-doped WO_3 thin films, (3) to determine computationally the amount of Ti doping that will maximize material structural stability, (4) to investigate sensitivity and stability of WO_3 thin films under gas testing, and (5) to promote research and education in the area of sensors and controls.

The effect of processing conditions on the growth and microstructural evolution of undoped and doped WO_3 thin-films and nanostructures were systematically studied by X-ray diffraction (XRD), scanning electron microscopy (SEM), atomic force microscopy (AFM), energy dispersive X-ray spectrometry (EDS), Fourier transform infrared absorption (FT-IR), Raman, and X-ray photoelectron spectroscopy (XPS). These measurements allowed us to understand the structure-property relationships and the electronic structure changes associated with the oxide surfaces, which in turn permitted the development of stable microstructures that will address long-term stability and H_2S selectivity issues. This comprehensive suite of measurements, together with temperature-dependent electrical characterizations and performance evaluation tests, were performed on the WO_3 and Ti- doped WO_3 materials to asses their feasibility for use in coal gasification systems.

REPORT DETAILS

The analysis of the research findings presented here integrates multi-technique experimental measurements with computational investigations, as outlined below and described in detail in the attached pier-reviewed articles.

(1) Study the characteristics of undoped WO_3 thin films synthesized by RF sputtering

Of the different types of metal oxides, WO_3-based materials are known to be valuable candidates for gas sensing. However, the properties of undoped or doped WO_3 are strongly dependent on the conditions and methods used in its deposition, as revealed in our earlier reports. In order to achieve stable, selective, and reliable sensors, accurate preparation of the functional material is crucial; many factors must be taken into account to warrant homogeneous grain characteristics such as shape and size, distribution, porosity, and surface conditions. Moreover, stabilization of electronic properties is of utmost importance to avoid changes during sensor use, thereby allowing the high operating temperatures required for fast responses and short recovery times.

To address the above-mentioned issues of the effect of processing conditions on the growth and microstructure evolution of WO_3 thin films, we analyzed them by XRD, SEM, AFM, FT-IR absorption, Raman, and XPS. These measurements allowed us to understand the structure-property relationships and the electronic structure changes associated with the oxide and to addresses material long-term stability.

The outcomes of this part of the research are as follows:

- The fabrication of WO_3 thin films using reactive deposition of W-metal targets for sputtering was achieved under the optimum reactive gas pressure of $Ar:O_2$ = 1:6 and under the condition of substrate temperatures varying from room temperature (RT) to 500 ^{0}C.

- The effect of temperature variation on the morphology of WO_3 thin films, which was investigated by HRSEM, XRD, and AFM, revealed an increase in average crystallite size and surface roughness with increasing temperature. The fine microstructure and uniform distribution of WO_3 particles grown at 100^0 – 200 ^{0}C, with average sizes ranging between 10 - 14 nm, transformed to large crystallites with dimensions of about 62 nm. No features were observed for temperatures < 100 ^{0}C, suggesting a completely amorphous nature for the samples. Also, the cross-sectional SEM analysis indicates that the WO_3 films grow in columnar structures on Si surfaces.

- The abovementioned microscopic observations were in agreement with the XRD, FT-IR, and Raman data, suggesting that a further increase in temperature beyond 200 ^{0}C results in changes in the crystal structure and morphology.

The results obtained from these investigations were published in the following six peer-reviewed articles, which are attached (please see appendix):

- "*Tungsten Oxide (WO_3) Thin Films for Application in Advanced Energy Systems*" by Satya K. Gullapalli, Rama S. Vermuri, Felicia S. Manciu, Jose L. Enriquez, and Chintalapalle V. Ramana, *Journal of Vacuum Science and Technology A,* vol. 28, Issue 4, 824-828 (2010);

- "*Structural transformation induced changes in the optical properties of nanocrystalline tungsten oxide thin films"* by Satya K. Gullapalli, Rama S. Vemuri, and Chintalapalle V. Ramana, *Applied Physics Letters*, vol. 96, Issue 17, 171903 (2010);

- "*Effect of Structure and Size on the Electrical Properties of Nanocrystalline WO_3 Films"* by Rama S. Vemuri, Kamala K. Bharathi, Satya K. Gullapalli, and Chintalapalle V. Ramana, *ACS Applied Materials & Interfaces*, vol. 2, Issue 9, 2623-2628 (2010);

- "*Spectroscopic Analysis of WO_3 Thin Films*" by Felicia S. Manciu, Jose L. Enriquez, William G. Durrer, Young Yun, Chintalalpalle V. Ramana, and Satya K. Gullapalli, *Journal of Materials Research*, vol. 25, Issue 12, 2401-2406 (2010);

- "*Physical properties and surface/interface analysis of nanocrystalline WO_3 films grown under variable oxygen gas flow rates*" by Rama S. Vemuri, Guillermo Carbjal-Franco, D.A. Ferrer, M.H. Engelhard, Chintalapalle V. Ramana, *Applied Surface Science*, vol. 259, 172-177, DOI: 10.1016/j.apsusc.2012.07.014 (2012);

- "*Correlation between Surface Chemistry, Density, and Band Gap in Nanocrystalline WO_3 Thin Films*" by Rama S. Vemuri, M.H. Engelhard, Chintalapalle V. Ramana, *ACS Applied Materials & Interfaces*, vol. 4, Issue 3, 1371-1377, DOI: 10.1021/am2016409 (2012).

(2) Explore the stabilization and structural modifications of Ti-doped WO_3 thin films

We anticipate that Ti-doped WO_3 could be a better candidate for selective detection of H_2S and other sulfur containing emissions. The reason for this anticipation is that Ti^{4+} ions form

acceptor-type centers in a WO_3 crystal (with respect to undoped material), resulting in oxidation of Ti and the formation of TiO_2, which strongly interacts with and absorbs H_2S. Alternatively, when WO_3 is exposed to H_2S, the formation of additional surface oxygen vacancies and the generation of W^{5+} centers are expected. Potential reaction products are SO_2 and H_2O, which will subsequently desorb. Therefore, the detection of H_2S with Ti-doped WO_3 is due to a combination of titania and WO_3 interacting with the specific gas. Furthermore, by doping with Ti we expect to widen the operating temperature range of the sensor material and, consequently, to enhance its quality in industrial use. We consider Ti doping of WO_3 with different percentages of Ti.

The outcomes of this part of the research, which again implies the samples being subjected to multi-technique investigations, are as follows:

- The thin films with Ti (5%) dopant were fabricated under conditions similar to those of the undoped WO_3 samples. However, for the doped samples, a custom made alloy-target target containing W-95% and Ti-5% was used for sputtering. Also, the optimum reactive gas pressure ratio of $Ar:O_2$ was in this case 1:9. Again, in order to understand the effect of temperature on the microstructure and grain-distribution characteristics, the substrate temperature was varied from RT to 500 ^{0}C.

- Ti-doping induces disorder into the structure of WO_3 thin films. The HRSEM and AFM microscopic data demonstrate that the films grown at temperatures ≤ 200 ^{0}C are completely amorphous. The nano-crystalline W-Ti oxide formation occurs at a temperature of at least 200 ^{0}C. However, the grain-sizes are extremely small at this temperature. The crystallinity and grain-size increases with increasing temperature. A comparison indicates that a higher temperature is required in order to obtain microstructure for W-Ti oxide films that is comparable to that of W-oxide films.

- The microscopic data corroborate with morphological XRD results, where a tetragonal structure was found for $W_{0.95}Ti_{0.05}O_3$ films. Broader and shifted bands were observed in Raman spectroscopic investigations. Their frequency positions support the finding of a distorted, potential tetragonal structure.

- Since some properties of Ti(5%) doped WO_3 are controlled by surface defects rather than by the intrinsic nature of the material, the samples were analyzed by XPS, too. These measurements revealed a reduced WO_{3-x} stoichiometry at the surface for the doped samples.

- The results obtained on the Ti(5%)-doped WO_3 films also motivated us to explore the advantages of higher Ti concentration. Thus, samples with Ti(20%) were grown using a set of conditions similar to those employed for Ti(5%)-doped WO_3 films. The experimental analysis of these samples demonstrate that Ti(20%) incorporation induces a complete disorder into the material structure, leading to an amorphous nature for these films, even at an increased substrate growth temperature. Furthermore, annealing the Ti-doped samples didn't make a significant change in the crystallinity of these samples.

The scientific outcomes of these analyses were published in four peer-reviewed articles that are also attached (please see appendix):

- *"The disordering effect of Ti observed in the microstructure and electrical properties of $W_{0.95}Ti_{0.05}O_3$ thin films"* by Narasimha R. Kalidindi, Kamala K. Bharathi, and Chintalapalle V. Ramana, *Applied Physics Letters*, vol. 97, Issue 14, 142107 (2010).

- "*Crystal Structure, Phase, and Electrical Conductivity of Nanocrystalline $W_{0.95}Ti_{0.05}O_3$ Thin Films"* by Narasimha R. Kalidindi, Felicia S. Manciu, and Chintalapalle V. Ramana, *ACS Applied Materials & Interfaces*, vol. 3, 863 (2011).

- *"Comparative microscopic and spectroscopic analysis of temperature dependent growth of WO_3 and $W_{0.95}Ti_{0.05}O_3$ thin films"* by Felicia S. Manciu, Young Yun, William G. Durrer, James Howard, Ute Schmidt, and Chintalapalle V. Ramana, *Journal of Materials Science*, vol. 47, 6593–6600, DOI 10.1007/s10853-012-6591-z (2012).

- "*Optical Constants of Amorphous, Transparent Titanium-Doped Tungsten Oxide Thin Films*" by Chintalapalle V. Ramana, Gaurav Baghmar, Ernesto J. Rubio, Manuel J. Hernandez, *ACS Applied Materials & Interfaces*, vol. 5, Issue 11, 4659-4666, DOI: 10.1021/am4006258 (2013).

(3) Determine computationally the amount of Ti doping that will maximize material structural stability

Computational analysis was used to provide means for quick determination of the suitability of different amounts of Ti doping that will maximize material structural stability as well as the probability of its transformation to a tetragonal or higher symmetry phase. Structural and electronic properties of Ti-doped WO_3 with incremental amounts of Ti dopant were simulated with different programs (e.g., Cerius (Accelrys Inc.), Gaussian, and other QM/MM software).

Whereas the WO_3 crystal structure is known to be monoclinic at room temperature, its structure changes with the temperature and so far four different crystal structures have been found: triclinic from 25-30 ^{0}C, monoclinic from 30-330 ^{0}C, orthorhombic from 330-740 ^{0}C, and tetragonal from 740-1437 ^{0}C.

The three different crystalline morphologies of WO_3 which are of interest for this study, are the monoclinic (space group $P2_1/n$), the orthorhombic (space group P_{mnb}), and the tetragonal (space group P4/*nmm*). The schematic representation of the unit cells associated with these morphologies, together with their X-ray diffraction spectra, are presented in Figures 1, 2, and 3. They are in good agreement with the literature data. They were obtained using Accelrys 4.0 software.

The higher symmetry of the tetragonal phase is revealed in Figure 3 by the expected smaller number of diffraction peaks. However, it is worth pointing out that there is still a debate in the literature regarding XRD structural assignments to higher symmetry phases such as the tetragonal one, for doped, as well as for undoped WO_3 materials. One main reason for this difference of opinion is the fact that the strongest diffraction peaks for monoclinic, orthorhombic, and tetragonal structures are very slightly separated, with 2θ values ranging from about 23^0 to 25^0.

Furthermore, if thin films versus powder samples are considered, the assignment is even more difficult due to the broadness of the peaks and to the film preferential growth direction as observed in Figure 4, where a comparison between these diffraction lines and our previous XRD experimental results for pure WO_3 is presented.

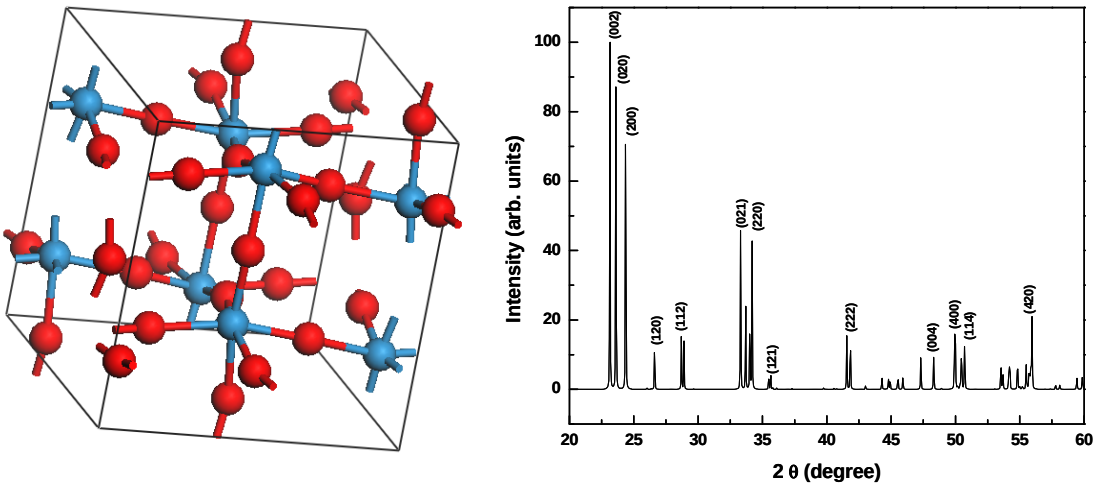

Figure 1: Schematic representation of WO_3 unit cell for monoclinic structure (W atom - blue and O atom - red) and the characteristic X-ray diffraction spectrum with the Miller indices determined for the monoclinic structure.

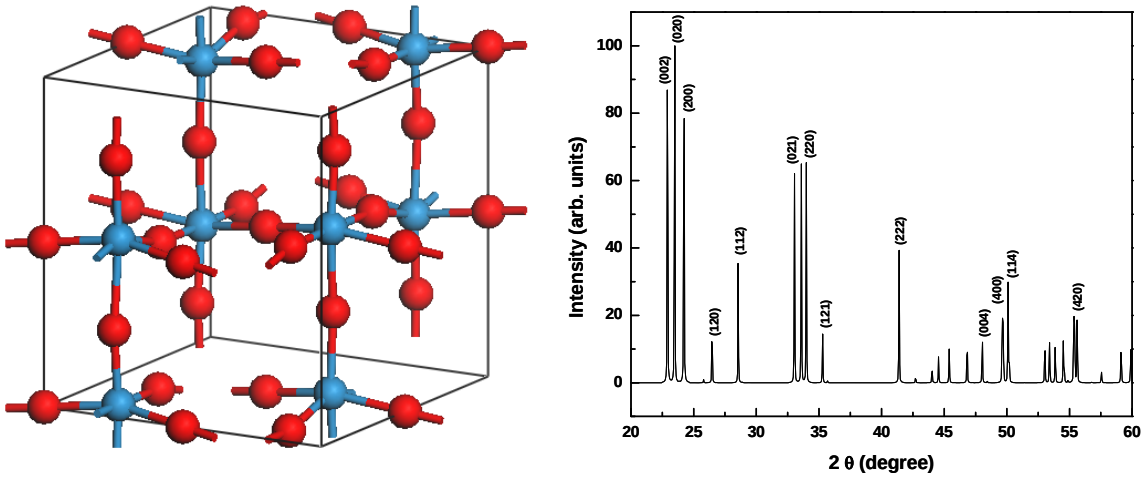

Figure 2: Schematic representation of WO_3 unit cell for orthorhombic structure (W atom – blue and O atom - red) and the characteristic X-ray diffraction spectrum with the Miller indices for the orthorhombic structure.

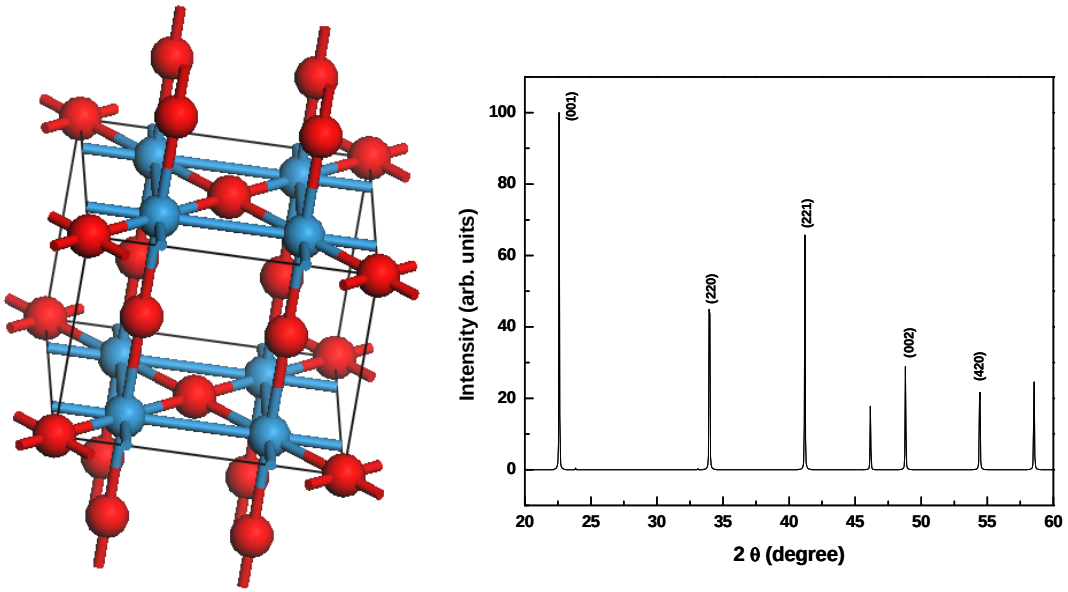

Figure 3: Schematic representation of WO_3 unit cell for tetragonal structure (W atom - blue and O atom - red) and the characteristic X-ray diffraction spectrum with the Miller indices for the tetragonal structure.

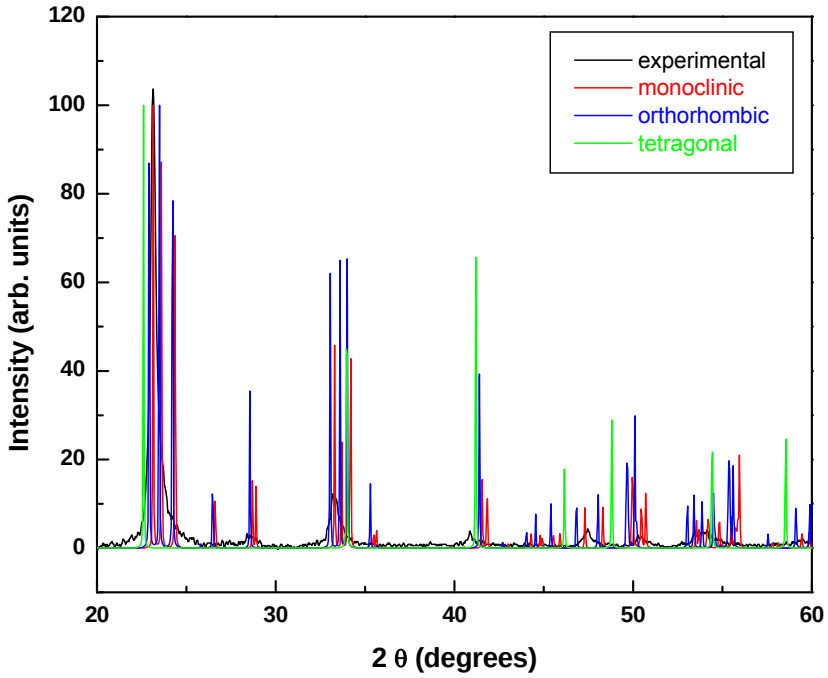

Figure 4: Comparison of experimental results obtained for pure WO_3 thin films (black line) with characteristic X-ray diffraction spectra for monoclinic (red line), orthorhombic (blue line), and tetragonal (green line) WO_3 structures.

We also performed calculations for Ti-doped WO_3 using a semi-empirical Molecular Orbital method, based on Dewar and Thiel's version of the Neglect of Diatomic Differential Overlap (NDDO) approximation. These calculations were implemented in the software MOPAC2012, which introduced new parameterizations for the atoms, including the heavy atoms such as tungsten (Parameterization Model 7, PM7).

To validate the outcomes of these theoretical simulations that suggest the likelihood of tetragonal structure achievement for a value of ~10% Ti doping, samples with about this Ti percentage were synthesized. This set of samples was grown at different substrate temperatures ranging between room temperature (RT) and 500 ^{0}C, in increments of 100 ^{0}C. The samples were again investigated using the same multi-technique analysis such as HRSEM, XRD, Raman, and infrared absorption.

Comparison from microscopic, spectroscopic, structural, and conductive perspectives, of the newly synthesized 8% Ti-doped WO_3 samples with our previous results, suggest better sample quality for doping of just 5% Ti.

(4) Investigate sensitivity and stability of WO_3 thin films under gas testing

Pure WO_3 films were tested by measuring their electrical properties under gas exposure. Sulfur containing gas (sulfur dioxide in this case) was employed for such measurements. The test chamber was first evacuated to measure the base line electrical performance of pure WO_3 films under vaccum. Then, 70 ppm of SO_2 test gas was introduced to measure the material performance as a function of temperature. The results obtained are shown in Figure 5. The following key points can be noted from the curves shown in this figure.

- Base line current of about 0.9 μA
- Negligible change for the current in vacuum (10^{-3} torr) with increasing temperature
- Linear increase of the current in the presence of SO_2 gas (75 ppm) with temperature increasing from 100 ^{0}C to 400 ^{0}C, indicating the SO_2 gas sensing property of the material
- Response time of about a millisecond

These characteristics demonstrate that the pure WO_3 film works as a sensor material to detect the sulfur containing emissions at higher temperatures (~300 - 400 ^{0}C). It is clear from the linear trend that these films can even work for temperatures higher than 400 ^{0}C.

The stability performance of WO_3 films was further investigated. This set of materials was additionally exposed to higher temperatures under the same processing conditions as utilized in SO_2 sensing. No significant structural changes were evident in the range of 25 - 725 ^{0}C. However, the size of the grains slightly increased upon extended exposure at 800 ^{0}C (for more than 16 hours).

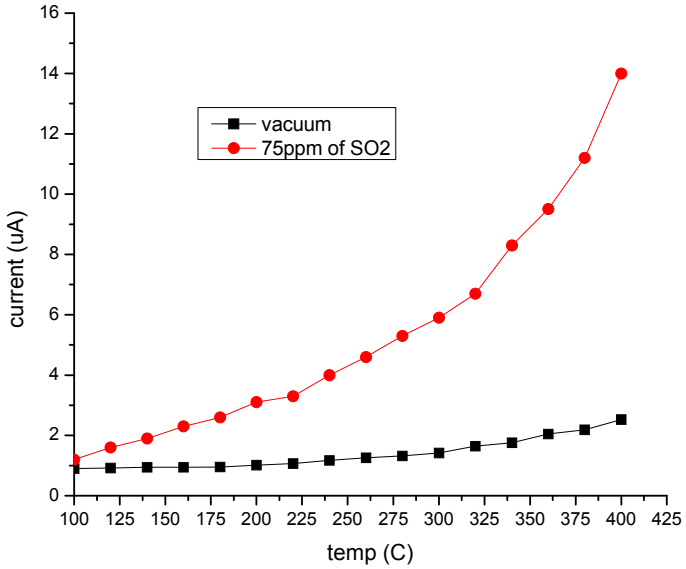

Figure 5. The response of WO_3 films grown on Si(100) substrates to sulfur containing test gas. The test gas was sulfur dioxide (SO_2), as allowed for use in laboratory testing.

(5) Promoting research and education in the area of sensors and controls

Through this grant, UTEP science and engineering students such as Satya Gullapalli, Jose Luis Enriquez, Rama Vermuri, Young Yun, Jose Mares, Narasimha Kalidindi, James Howard, and Aurelio Paez had the opportunity to receive financial support during their graduate studies. This grant contributed not only to the increase in the number of graduate students in engineering and science at UTEP, but, more importantly, it contributed to augmenting student understanding of fundamental concepts as applied to sensor materials, which is one of the DOE imperative objectives. This affirmation is supported by the number of students who received their degrees performing research in this project:

Jose Luis Enriquez (M.S., 2010) – continued his Ph.D studies at UTEP

Satya Gullapalli (M.S., 2010) – continued Ph.D. studies at UTEP

Narasimha Kalidindi (M.S., 2010) – Safety Engineer / Working in Industry

Rama Vemuri – Partially supported by the project during Ph.D. studies – Postdoctoral Research Associate at Pacific Northwest National Laboratory

Jose Luis Enriquez (Ph.D., 2012) – Assistant Professor, Universidad Autonoma De Ciudad Juarez, Juarez, Mexico

Jose Mares – Partially supported by the project – Currently working in Industry

James Howard (Ph.D., 2012) – Partially supported by the project during Ph.D. studies – Veteran and minority disabled naval lieutenant

Young Yun (Ph.D., 2012) – Partially supported by the project during Ph.D. studies – Assistant Professor, Seokyung University, Korea.

Aurelio Paez (M.S., 2014) – Partially supported by the project

CONCLUSIONS

During the grant period, we found that Ti-incorporation into WO_3 induces disorder into the material structure. While a low concentration could be practical, a high concentration leads to an amorphous nature for these films, even with an increased substrate growth temperature. Furthermore, annealing the Ti-doped samples didn't make a significant change in the crystallinity of these samples.

Comparative experimental approaches such as AFM, SEM, XRD, and Raman revealed that the growth temperature influences the morphology of the material, such as the roughness, the mean grain size of the nanoparticles on the surface layer, and the crystallinity of undoped and doped WO_3 thin films. The results show that a higher temperature is required to obtain crystalline microstructure for Ti-doped WO_3 films than for WO_3 films. With increasing growth temperature, the results for WO_3 films show increases in the average crystallite size from 10-14 nm at RT to ~60 nm at 500 ^{0}C, and in the surface roughness from 4 nm at RT to about 12 nm at 500 ^{0}C. Much smaller average grain sizes are attained for crystalline $W_{0.95}Ti_{0.05}O_3$ samples grown at the same high temperatures as the WO_3 material, *e.g.*, at 500 ^{o}C, a ~30 nm average grain size is observed for the Ti-doped samples versus the ~60 nm average grain size for pure WO_3 thin films.

Also, in order to understand the physics of Ti-doped WO_3 films and the effect of growth temperature on their electronic structure, the refractive index as a function of temperature was determined. The observed linear increase in the refractive index values for films grown at higher temperatures was attributed to the improved packing density of the material.

The gas testing performance of undoped WO_3 films, which was done by measuring the electrical properties of the material under SO_2 exposure, demonstrate that WO_3 works as a sensor material to detect the sulfur containing emissions at higher temperatures (~300-400 ^{o}C). The observed trend of increasing current with temperature increase suggests that these films can even work for temperatures higher than 400 ^{o}C.

As high quality materials with excellent ordered structure and narrower particle-size distributions (which can also withstand high-temperature technological environments such as those encountered in furnaces and coal gasification systems, without their structure being affected by phase transformations) are needed for developing new, more sensitive sensors, the research presented here demonstrates that W-Ti-O thin films grown by RF sputtering could be valuable candidates. The observed higher structural symmetry (with a possible tetragonal morphology as demonstrated in our previous reports) for the samples grown at 500 ^{o}C, which also suggests a favorable crystalline size distribution, is indicative of the future potential of these films in such applications.

APPENDIX

ACS APPLIED MATERIALS & INTERFACES

Research Article

www.acsami.org

Correlation between Surface Chemistry, Density, and Band Gap in Nanocrystalline WO_3 Thin Films

R.S. Vemuri,[†,‡,§] M.H. Engelhard,[§] and C.V. Ramana*[,†,‡]

[†]Department of Mechanical Engineering and [‡]Department of Materials Science and Engineering, University of Texas at El Paso, El Paso, Texas 79968, United States

[§]Environmental Molecular Sciences Laboratory (EMSL), Pacific Northwest National Laboratory (PNNL), Richland, Washington 99352, United States

ABSTRACT: Nanocrystalline WO_3 thin films were produced by sputter-deposition by varying the ratio of argon to oxygen in the reactive gas mixture during deposition. The surface chemistry, physical characteristics, and optical properties of nanocrystalline WO_3 films were evaluated using X-ray photoelectron spectroscopy (XPS), scanning electron microscopy (SEM), atomic force microscopy (AFM), X-ray reflectivity (XRR), and spectrophotometric measurements. The effect of ultramicrostructure was significant on the optical properties of WO_3 films. The XPS analyses indicate the formation of stoichiometric WO_3 with tungsten existing in fully oxidized valence state (W^{6+}). However, WO_3 films grown at high oxygen concentration (>60%) in the sputtering gas mixture were over stoichiometric with excess oxygen. XRR simulations based on isotropic WO_3 film−SiO_2 interface−Si substrate modeling indicate that the density of WO_3 films is sensitive to the oxygen content in the sputtering gas. The spectral transmission of the films increased with increasing oxygen. The band gap of these films increases from 2.78 to 3.25 eV with increasing oxygen. A direct correlation between the film density and band gap in nanocrystalline WO_3 films is established on the basis of the observed results.

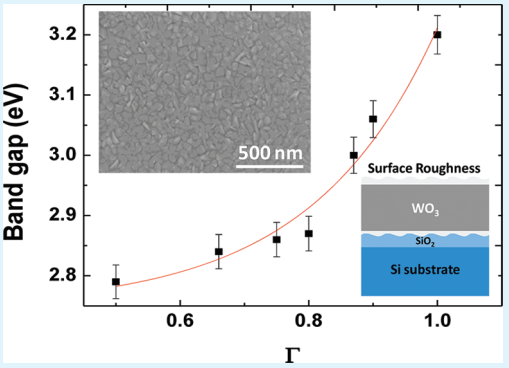

KEYWORDS: *WO_3 thin films, surface chemistry, XPS density, X-ray reflectivity, spectrophotometry, optical properties, band gap*

1. INTRODUCTION

Tungsten oxide (WO_3) is an intensely studied representative of a group of "chromogenic" materials because of the coloration effects associated with various processes.[1−6] There has been a great deal of recent interest in low-dimensional structures of WO_3 for a wide variety of applications in optoelectronics, microelectronics, selective catalysis, and environmental engineering.[2−20] WO_3 has been in use for the development of smart windows for energy-efficient architecture of buildings and automobiles, flat-panel displays, optical memory and writing−reading−erasing devices, and electronic information displays.[1−6] It has been demonstrated that WO_3 films exhibit chemical sensing properties that have numerous applications in environmental and industrial pollution monitoring.[7−18] WO_3 films exhibit excellent functional activity to various gases (e.g., H_2S, NO_x, trimethylamine, and other organics) and are suitable for use in integrated sensors.[13−18] Most recently, the attractive properties of WO_3-based materials have increased their consideration for application in photoelectrochemical cells (PECs) for hydrogen production by water splitting.[19−21] In addition, Zheng et al. have proposed and demonstrated new applications of WO_3 in emerging dye-sensitized solar cells (DSSC) technology.[22] Although the efficiency is not comparable to those that employ the best known TiO_2-based DSSCs, there are options to tailor the microstructure and chemistry in order to improve the efficiency.[22] A very detailed account of structure, synthesis, and application of nanostructured WO_x can be found in a current review article where the opportunities and scope for further exploitation of nanostructured WO_3 materials in emerging technological applications is presented.[23]

WO_3 is a complicated material with respect to crystal structure and thermal stability because of several structures, such as monoclinic, triclinic, tetragonal, orthorhombic, cubic, and hexagonal for pure and oxygen deficient WO_3.[1−3,24−28] At room temperature, WO_3 crystallizes in a triclinic structure and exhibits structural transformation at higher temperatures. Investigations on bulk WO_3 report the following sequence: triclinic (~30 °C) → monoclinic (330 °C) → orthorhombic (740 °C) → tetragonal.[1,3,24−29] Additionally, formation of pyrochlore WO_3 structure at about 373 K has been reported.[30] The ideal WO_3 crystal structure can be represented as a cubic ReO_3 structure.[31,32] In fact, the polymorphs of WO_3 can be described as distortions from the cubic ReO_3 structure.[1,24−29] However, WO_3 thin films prepared by a wide variety of chemical and physical techniques employing various processing conditions usually exhibit different crystal structure, morphology, surface/interface chemistry, and electronic and electrochemical properties.[1−17,33−40]

Received: November 22, 2011
Accepted: January 10, 2012
Published: February 14, 2012

The optical, photochemical, and electrical properties of metal oxide thin films grown from chemical or physical vapor deposition methods are sensitive to the physical and chemical characteristics, which in turn depend on the processing conditions and precursor materials. For instance, the density and index of refraction for TiO_2, SiO_2 HfO_2, and ZrO_2 thin films was shown to be sensitive to the processing conditions.[41−43] From this point of view, a detailed understanding and control over the physical parameters (e.g., crystal structure and density) and chemical parameters (e.g., valence state of W ions and composition) in WO_3 thin films is required in order to optimize performance for a given application. The present work was, therefore, performed on sputter-deposited nanocrystalline WO_3 films under varying the oxygen partial pressure at a fixed deposition temperature. Earlier we reported on the effect of deposition temperature on the microstructure and electrical properties of nanocrystalline WO_3 films.[34−36] We found that the effect of growth temperature is significant on the structure, phase, grain-size and electrical conductivity of nanocrystalline WO_3 films.[34−36] The objective of the present work is to derive a detailed understanding of the surface chemistry, density and optical properties, which will have profound influence on the optical, electronic, and photochemical device performance of WO_3 films. Interestingly, a correlation is found between surface chemistry, density, and band gap in nanocrystalline WO_3 films as presented and discussed in this paper.

2. EXPERIMENTAL SECTION

A. Fabrication. WO_3 thin films were deposited onto optical grade quartz and silicon (Si) (100) wafers by radio frequency (RF) (13.56 MHz) magnetron sputtering. All the substrates were thoroughly cleaned using the standard procedure reported elsewhere,[34] and dried with nitrogen before introducing them into the vacuum chamber. The chamber was initially evacuated to a base pressure of $\sim 1 \times 10^{-6}$ Torr. Tungsten (W) metal target (Plasmaterials Inc.) of 3" diameter and 99.95% purity was employed for reactive sputtering. The W-target was placed on a 3 in. sputter gun, which is placed at a distance of 8 cm from the substrate. A sputtering power of 40 W was initially applied to the target while introducing high-purity argon (Ar) into the chamber to ignite the plasma. Once the plasma was ignited, the power was increased to 100 W and oxygen (O_2) was released into the chamber for reactive deposition. The flow of the Ar and O_2 and their ratio was controlled using as MKS mass flow meters. Before each deposition, the W-target was presputtered for 10 min using Ar alone with shutter above the gun closed. The samples were deposited by varying the oxygen content in the reactive gas mixture while keeping the deposition temperatures (T_s) fixed at 400 °C. Specifically, the oxygen gas fractionation ratio [$\Gamma = O_2/Ar+O_2$] is varied in order to study the effect of oxygen gas flow rate on the structure and optical properties of WO_3 films. The deposition was made for a constant time of 60 min. The substrates were heated by halogen lamps and the desired temperature was controlled by an Athena X25 controller.

B. Characterization. The grown WO_3 films were characterized by performing structural and optical measurements. Surface imaging analysis was performed using a high-performance and ultra high resolution scanning electron microscope (Hitachi S-4800). Secondary electron imaging was performed on WO_3 films grown on Si wafers using carbon paste at the ends to avoid charging problems. The grain detection, size-analysis and statistical analysis was performed using the software provided with the SEM. X-ray reflectivity (XRR) measurements were performed using a Bruker Discover D8 X-ray diffractometer. Samples grown on Si substrates were employed for XRR measurements. All the measurements were made ex situ as a function of partial pressure. The thickness and density calculations were performed by fitting the XRR data using LEPTOS software. The film thickness was obtained by the period of oscillations in the XRR curve. The film-density was determined by the position of total reflection edge. Surface imaging was also performed using an atomic force microscope (AFM) (Nanoscope IV-Dimension 3100 SPM system). WO_3 films grown on Si wafers were used for AFM analysis. The main purpose of AFM measurements was to obtain quantitative information on the surface roughness and compare with the results of XRR fitting.

XPS measurements were performed with a Physical Electronics Quantera scanning X-ray microprobe. This system uses a focused monochromatic Al $K\alpha$ X-ray (1486.7 eV) source for excitation and a spherical section analyzer. The instrument has a 32 element multichannel detection system. A 100 W X-ray beam focused to 100 μm diameter was rastered over a 1.4 mm × 0.1 mm rectangle on the sample. The X-ray beam is incident normal to the sample and the photoelectron detector is at 45° off-normal. High energy resolution spectra were collected using a pass-energy of 69.0 eV with a step size of 0.125 eV. For the Ag 3d5/2 line, these conditions produced a fwhm of 0.91 eV. The sample experienced variable degrees of charging. Low energy electrons at ~1 eV, 20 μA and low energy Ar^+ ions were used to minimize this charging.

The optical properties of WO_3 films were evaluated using optical transmission and reflectance measurements using Cary 5000 UV−vis-NIR double-beam spectrophotometer. Films grown on optical grade quartz were employed for optical property measurements. The quartz substrates employed extends the transparency range down to ~190 nm and determining the absorption edge extending into ultraviolet (UV) region, which is more than sufficient to determine the band gap shift in deficient or stoichiometric or metal incorporated WO_3 films.

3. RESULTS

A. Surface Chemistry − XPS. X-ray photoelectron spectroscopy (XPS) data indicate that the WO_3 films are stoichiometric within a certain range of oxygen content in the reactive gas mixture while it becomes overstoichiometric for higher oxygen content. An XPS survey spectrum of a representative sample ($\Gamma = 0.9$) is shown in Figure 1. The XPS curve of as-grown sample (Figure 1a; lower panel) indicates that W and O were the main constituent elements of the samples, except for the C present in the sample surface. The C 1s peak observed at a binding energy (BE) of 284.6 eV for as-grown samples originates from surface adsorbed carbon species. It can be seen in the XPS curve (Figure 1b; upper panel) of the same sample that was sputtered for a few minutes with 2 kV Ar^+ ions that it shows no signal from C 1s level. This is a clear indication that the carbon presence is a result of adsorbed species on the film surface due to sample handling and can be removed with a light sputtering of the surface with low-energy Ar^+ ions.

The detailed core-level spectra of W 4f and O 1s peaks for WO_3 films are shown in Figure 2. For WO_3 films grown with $\Gamma = 0.5-0.9$, the XPS W 4f core-level peak exhibits a well-resolved doublet corresponding to W $4f_{5/2}$ and W $4f_{7/2}$ (Figure 2; upper panel) at the binding energy values of 37.9 and 35.8 eV, respectively. The W $4f_{7/2}$ peak at 35.8 eV in this work is in good agreement with the literature value of 35.7 eV characterizing the W^{6+} state in WO_3.[44−46] The corresponding O 1s core level peak at BE~530.5 eV (Figure 2; lower panel) is the typical of O atoms bonded to W.[47,48] Absence of any other contributions, such as surface adsorbed oxygen or carbonyl groups, can be noted. Also, the O 1s core level is symmetric for all the samples reflecting the characteristic feature of O atoms bonded with W atoms only. The chemical composition determined using integrated peak areas and sensitive factors indicate that the O/W ratio was maintained well in the films grown at $\Gamma = 0.5-1.0$. However, it was noted that for samples under 2 kV Ar^+ sputtering i.e., after the removal of a few top surface layers, the oxygen to tungsten atomic ratio in WO_3 films is always higher

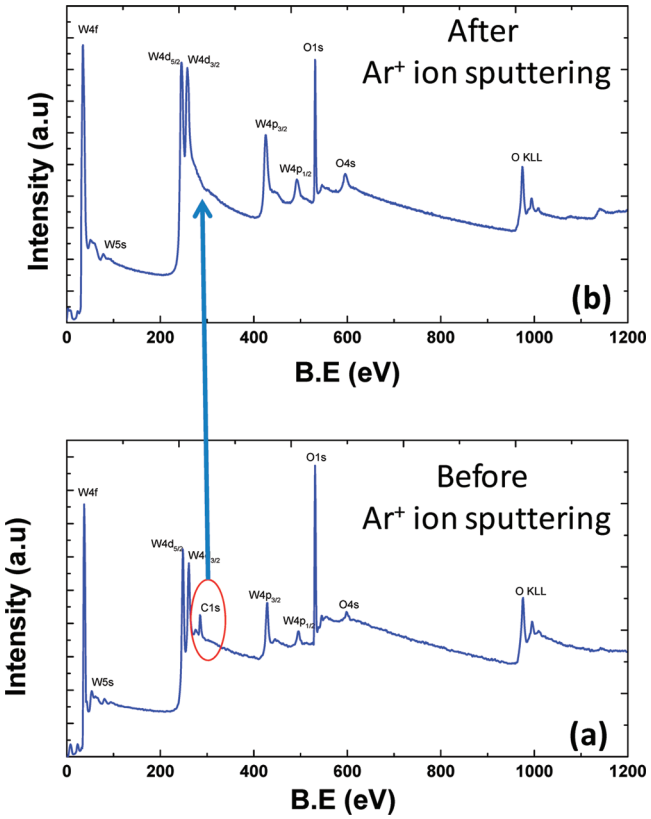

Figure 1. XPS survey spectra of WO_3 films. The survey spectrum obtained (a) before Ar^+ ion sputtering and that obtained (b) after sputtering are shown. The X-ray photoemission and Auger peaks and their respective binding energy positions are as indicated. It is evident that the C 1s peak disappears after Ar^+ ion sputtering indicating the adsorbed carbon on the samples surface.

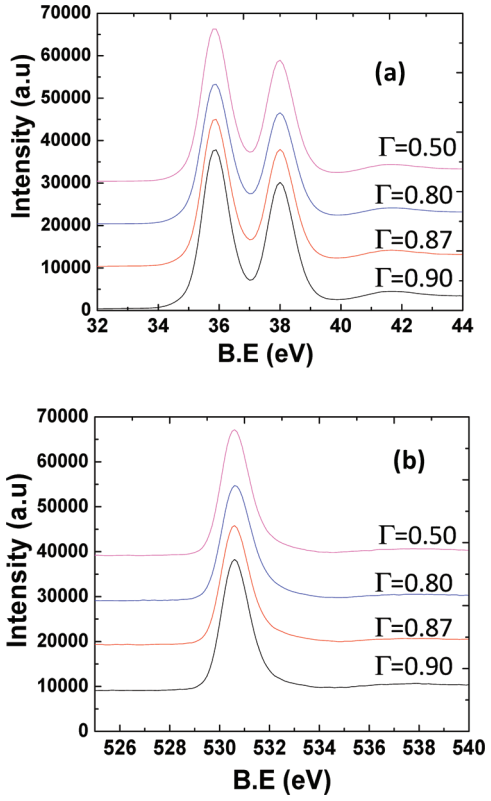

Figure 2. Core level XPS spectra of (a) W 4f and (b) O 1s.

than expected for those samples grown at $\Gamma \geq 0.6$. This observation indicates that there is excess oxygen trapped during the successive layer formation during film growth.

B. Film density and surface/interface structure – XRR, SEM, and AFM. The XRR patterns of WO_3 films are shown in Figure 3. Simulation of the XRR experimental data using appropriate models can provide physio-chemical information of the nanocrystalline WO_3 films. Specifically, the surface and interface roughness, thickness and density of the WO_3 films can be obtained from XRR spectra.[49] The density can be obtained from the total reflection or critical edge.[49] Film thickness can be derived from the period of the oscillations in the XRR spectra. In the present case, it is evident that the experimental and simulation curves are in excellent agreement for WO_3 films (Figure 3). The stack model used to simulate the spectra is shown in the inset of Figure 3a. The model contains, from top, WO_3 film, SiO_2 interface and Si substrate. The surface and interface roughness were also considered in order to accurately fit the experimental XRR spectra of WO_3 films. The following observations can be made from the XRR spectra (Figure 3). A positive shift (higher angle) of the critical edge with increasing oxygen flow rate is the first. The oscillations extend toward higher angle (>2°) is the second. The latter observation indicates that the film roughness is not very high. The positive shift of the critical edge indicates an increase in the film density with increasing oxygen content in the reactive gas mixture. The density varies in the range of 4.98–5.98 g/cm^3.

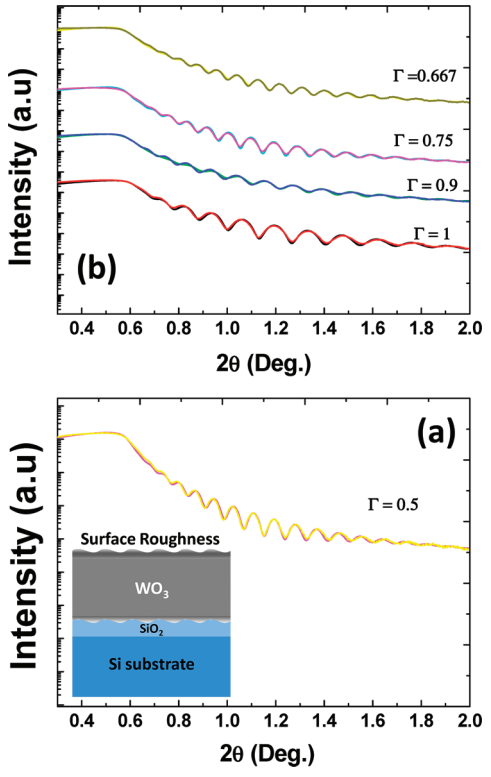

Figure 3. XRR experimental simulation curves of nanocrystalline WO_3 films. (a) The fitting procedure and the stack model employed are shown for films grown at Γ = 0.5. (b) The XRR curves and fitting is shown for a series of WO_3 films grown at variable oxygen concentration values.

dx.doi.org/10.1021/am2016409 | ACS Appl. Mater. Interfaces 2012, 4, 1371–1377

The film thickness and interfacial oxide thickness were also determined from XRR analysis. The variation of film thickness as a function of oxygen concentration is shown in Figure 4. It is

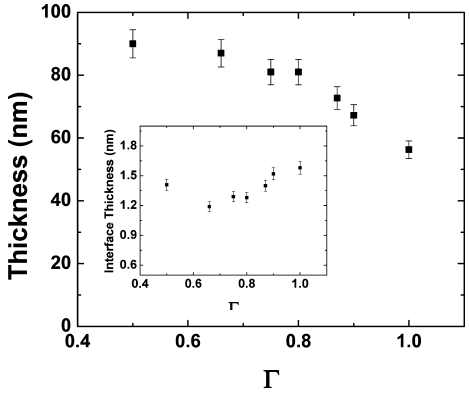

Figure 4. Variation WO_3 film thickness with oxygen concentration in the sputtering gas mixture. A continuous decrease in film thickness with increasing oxygen concentration can be noted. Inset shows the variation of interfacial SiO_2 thickness with Γ values.

evident that the film thickness decreases with increasing oxygen concentration. However, although the growth part is not very significant, a slightly increasing trend for interfacial oxide (SiO_2) with increasing oxygen concentration can be seen in the inset. Increasing oxygen pressure reduces the energy that the particles attain to the substrate and their mobility, making it more difficult for the sputtering species to bombard the substrate and, thus, leading to decreasing film thickness. During sputtering process, the target species are subjected to collisions with ambient gas molecules and other ejected atoms. The reactive sputter-gas, therefore, impedes the mobility and trajectory of sputtered species.

SEM images of nanocrystalline WO_3 films are shown in Figure 5. The fine microstructure and uniform distribution

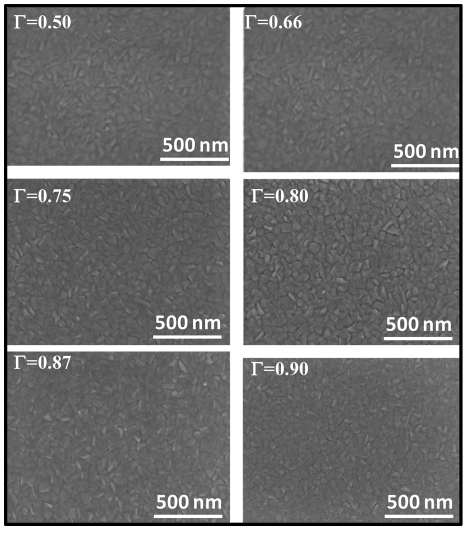

Figure 5. High-resolution SEM images of WO_3 films as a function of oxygen concentration in the sputtering gas mixture.

characteristics of the particles are evident in the micrographs (Figure 5). The X-ray diffraction (XRD) data (not shown) confirmed that these are crystalline grains. The average grain size, determined from XRD, gradually decreases with increasing oxygen flow rate. The grain size increases from 21 to 25 nm with increasing Γ to 0.65, at which point the grain size exhibits a decreasing trend to attain the lowest value of 15 nm at Γ = 1. The corresponding roughness and the randomness of the grains decrease with increasing oxygen content. Variation of the film surface roughness with oxygen concentration is presented in Figure 6. The values were determined from the XRR data

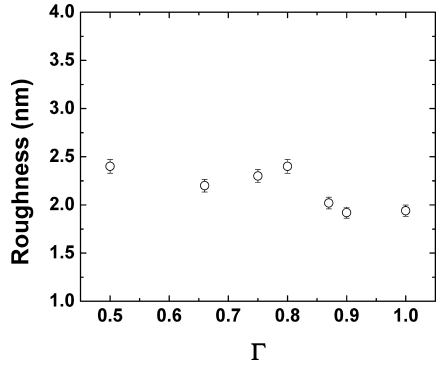

Figure 6. WO_3 film surface roughness determined from XRR.

where the surface roughness is varied order to obtain a best fit the experimental and simulation curves. The surface roughness values and their variation agrees well with the root-mean-square (rms) value surface roughness values obtained from AFM (not shown). It can be seen that the surface roughness decreases slightly with increasing oxygen concentration in the sputtering gas mixture.

C. Band Hap − Spectrophotometry. The optical transmittance spectra of WO_3 films are shown in Figure 7. The spectral

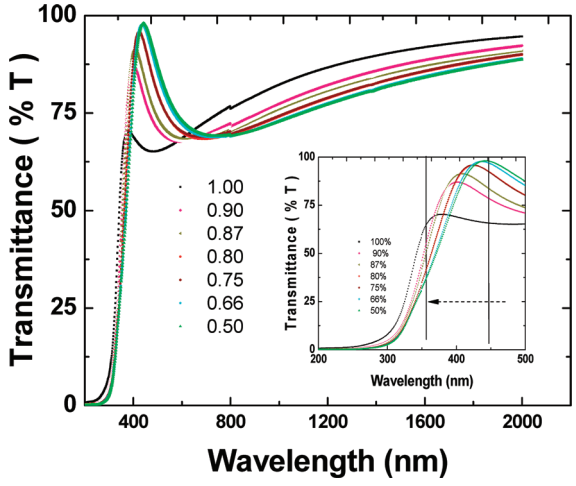

Figure 7. Spectral transmittance characteristics of WO_3 films as a function of oxygen concentration in the sputtering gas mixture. Inset shows the shift noted in the curves, as pointed by arrow, with increasing oxygen concentration.

transmission curves reveal the following characteristic features. (1) WO_3 films in general show a high transparency in the spectral region except where the incident radiation is absorbed across the band gap (E_g). This observation indicates the high-quality and transparent nature of WO_3 films. (2) An increase in optical transmittance with increasing oxygen content in the

dx.doi.org/10.1021/am2016409 | ACS Appl. Mater. Interfaces 2012, 4, 1371−1377

reactive gas mixture. Inset in Figure 7 shows the expanded version of the transmittance spectra in a selected spectral region to show the effect of Γ values. The behavior indicates that the effect of oxygen concentration in the sputtering gas influences the optical properties. (3) The oxygen content also influences the absorption across the band gap. It is evident that the absorption edge shifts to lower spectral region indicating that the increasing oxygen increases the energy of the absorption edge. An arrow with a window is presented as shown in inset of Figure 7 to indicate the absorption edge shift as a function of increasing Γ values.

A further analysis of the optical spectra is performed in order to better understand effect of oxygen content in the reactive gas mixture on the optical properties and to derive a quantitative structure−property relationship. It is well-known that the optical absorption below E_g follows an exponential behavior.[1,5,34,49] The absorption, therefore, is exponentially dependent on the energy ($h\nu$) of incident photon in that region. For WO_3, in the E_g region (high absorption) or above the fundamental absorption edge, the absorption follows a power law of the form[1,5,34,50]

$$(\alpha h\nu) = B(h\nu - E_g)^2 \quad \{1\}$$

where $h\nu$ is the energy of the incident photon, α the absorption coefficient, B the absorption edge width parameter, E_g the band gap. The optical absorption coefficient, α, of the films is evaluated using the relation[34,49,50]

$$\alpha = [1/t]\ln[T/(1 - R)^2] \quad \{2\}$$

where T is the transmittance, R the reflectance, and t the film thickness. The thickness values determined from XRR were employed to obtain the optical absorption coefficient of nanocrystalline WO_3 films. The absorption data and the plots obtained for WO_3 films are shown in Figure 8. It is evident that

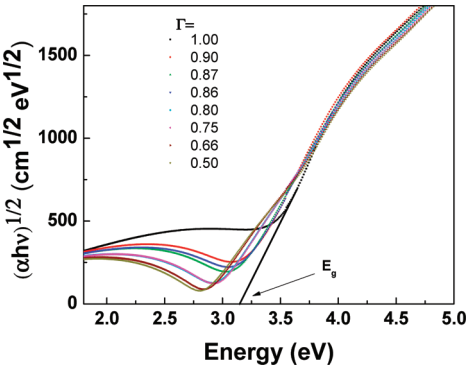

Figure 8. $(\alpha h\nu)^{1/2}$ vs $h\nu$ plots for WO_3 films grown at various oxygen concentration values. Extrapolating the linear region of the plot to $h\nu = 0$ provides the band gap value as indicated with an arrow.

$(\alpha h\nu)^{1/2}$ vs $h\nu$ results in linear plots in the high absorption region, $\alpha > 1 \times 10^4$ cm^{-1}, suggesting indirect allowed transitions across E_g of WO_3 films. Regression analysis and extrapolating the linear region of the plot to $h\nu = 0$ provide the band gap value as indicated with an arrow in Figure 8. The E_g values derived from curves shown in Figure 8 increases from 2.78 to 3.25 eV with increasing Γ values.

4. DISCUSSION

The chemistry−density−band gap (optical property) relationship in nanocrystalline WO_3 films can be derived on the basis of the observed results and taking the simultaneous effect of oxygen content in the sputtering gas mixture and, hence, the associated effects into account. A decrease in film thickness with increasing oxygen concentration in the sputtering gas mixture indicates that the effective number of species ejected from target surface and the effective number of particles reaching and attaining the substrate decreases with increasing Γ values. It can be seen that increasing oxygen concentration reduces the energy that the particles attain to the substrate and their mobility. As such, it more difficult for the sputtering species to bombard the substrate and, thus, leads to a decreasing growth rate that in turn reduces film thickness.[41,42] It must be pointed out that during sputtering process, the target species are subjected to collisions with ambient gas molecules and other ejected atoms. This behavior results in a partial loss of energy and direction on their respective paths, which makes it more difficult to attain the substrate. The reactive sputter-gas, therefore, impedes the mobility and trajectory of sputtered species. Furthermore, at a given or constant sputter-power, increasing oxygen pressure in the plasma shifts the thermalization region toward the target.[41−43,51] As a result, oxidation of the W target takes place leading to a decrease in deposition rate and, hence, thickness of WO_3 films. A faster decrease in the growth rate of WO_3 films at higher oxygen concentration can then be attributed to the combined effect of target oxidation, sputter-ejected species being impeded, decrease in the mean free path, and partial resputtering of the film.

The results obtained from XRR and spectrophotometry indicates that the oxygen content in the reactive gas mixture influences the density and band gap. To explain the observed results and derive the correlation, we show the variation in the density and band gap of WO_3 films with Γ in Figure 9. The most important and very first observation is that these two parameters exhibit similar functional dependence on Γ value. Second, the density and band gap data was found to fit to an exponential growth function. The results can be explained as follows. It should be noted that the measured density of the WO_3 films is less compared to that bulk of the tungsten oxide (7.16 g/cm^3).[1,52] On the other hand the density increases with increasing oxygen concentration is sputtering gas mixture. The lower values of density may be due to voids in the grains. Also, the density of vapor deposited thin films is always lower than that of bulk counterparts. The increase in density with increasing Γ values can be attributed to the incorporation of excess oxygen that is trapped during the successive layer formation leading to the total film thickness. Evidence for this comes from the XPS analyses where the superstoichimetry for films grown at Γ > 0.6 is noted. We believe the excess oxygen trapped is also responsible for the observed behavior of E_g values for nanocrystalline WO_3 films. In WO_3, E_g corresponds to electronic transitions from the top of valence band (formed by the filled O 2p orbitals) to the conduction band (formed by the empty W 5d orbitals).[1,5,34,50,52,53] Reduction in the band gap can be expected in the presence of oxygen vacancies or any other structural defects. As such, the lower density coupled with the observed lower E_g values can be attributed to the present of voids or vacancies. The increase in density and band gap with a progressive increase in oxygen concentration can be attributed to the excess oxygen. It has been argued that the extra oxygen atoms in the defect picture can be viewed as interstitials.[52] In fact, we believe this is indeed the case in our WO_3 films. This is based on the fact that there is a higher O/W ratio in XPS. This extra oxygen is responsible to decrease the grain size and shifts the E_g values to higher energy side. This is the reason why WO_3

dx.doi.org/10.1021/am2016409 | ACS Appl. Mater. Interfaces 2012, 4, 1371−1377

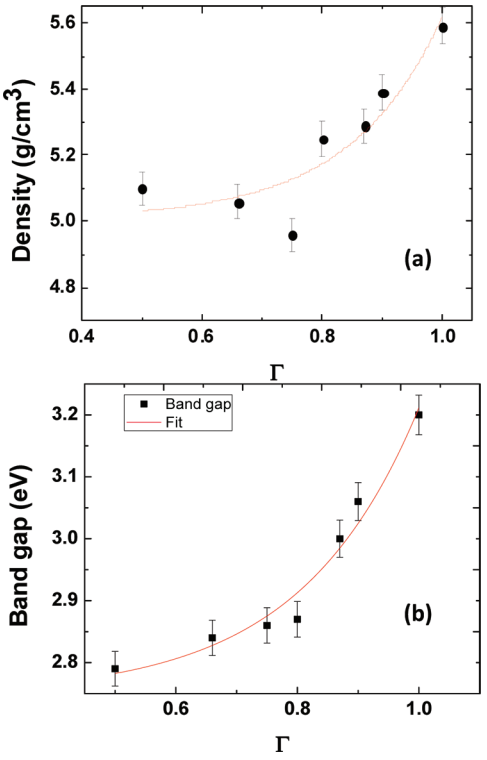

Figure 9. Comparison of (a) the trend of density variation and (b) band gap variation with oxygen concentration in sputtering gas mixture in nanocrystalline WO_3 films. A direct correlation between density and band gap in addition to similar trend can be noted. The density and band gap variation with oxygen concentration in the sputtering gas mixture follows an exponential growth function as indicted by lines.

films grown at higher oxygen concentration becomes more insulating, i.e., higher E_g, compared those grown at lower oxygen concentration. The presence of excess oxygen in sputtered grown oxides has been reported several times.[54−59] For instance, reactive sputtering of alumina films resulted in excess oxygen when sputtering was performed in the reactive oxygen atmosphere using Al target.[54] Using Rutherford backscattering spectrometry analysis, Chin et al have demonstrated the O/Ce ratio >2 in sputtered CeO_2 films.[55] Vink et al. have shown evidence for excess oxygen, which also helps lithium trapping, in sputtered WO_3 films.[56] Higher concentrations of oxygen chemisorbed on the film surface and along depth of the film leading to an increase in electrical conductivity has been reported for ZnO.[57] However, in the case of WO_3 films, the debate was on the presence of hydroxyl bonds[58,59] or the inherent processing effect of sputter-deposition[56] that accommodates the excess oxygen. XPS analysis of our WO_3 films did not reveal the presence of hydroxyl groups and the mechanism or the source of hydroxyl bonds for excess oxygen can, therefore, be ruled out. Our results are in close agreement with those reported by Venk et al.,[56] where it was claimed that the excess oxygen in the films is due to higher oxygen concentration and higher sputtering power, which are needed for incorporating the oxygen.[54−56] Specifically, the excess oxygen originates from negative ion effects, which is common in the oxygenated metal targets. As reported by Venk et al., negative oxygen ions are generated at the surface of the oxygenated targets.[56] These ions are accelerated and subsequently neutralized in the plasma. By virtue of their kinetic energy, the oxygen atoms can be incorporated in the growing film leading to the observed excess oxygen. A significant decrease in growth rate and film thickness (Figure 4) at higher oxygen concentration is direct evidence for the above-mentioned mechanism and excess oxygen incorporation into the growing WO_3 films.

5. CONCLUSIONS

Nanocrystalline WO_3 thin films were fabricated by reactive magnetron sputter-deposition by varying the ratio of argon to oxygen in a wide range. The surface chemical composition, valence state of W ions, surface/interface chemistry, density and optical properties of nanocrystalline WO_3 films were evaluated as function of oxygen concentration in the sputtering gas mixture. The results indicate that the effect of oxygen during deposition is significant on the ultramicrostructure in terms of surface/interface chemistry. This consequently influences the optical properties of WO_3 films. Formation of stoichiometric WO_3 with tungsten existing in W^{6+} state for all WO_3 films is evident. However, WO_3 films grown at high oxygen concentration (>60%) were over stoichiometric with excess oxygen incorporated. XRR data coupled with simulations indicate that the density of WO_3 films is sensitive to the oxygen concentration. The density varies from 4.98 to 5.98 g/cm^3 with increasing Γ values form 0.5 to 1.0. The spectral transmission and band gap of the WO_3 films increases with the increasing oxygen content in the reactive gas mixture. The band gap increases from 2.75 to 3.25 eV with increasing oxygen concentration. The corresponding density of WO_3 films also exhibit the similar variation as a function oxygen content indicating a direct relationship between the oxygen concentration, density and band gap. A direct correlation between the film-density and band gap in nanocrystalline WO_3 films is presented and explained on the basis of excess oxygen incorporation and negative ion effects as encountered in the sputter-deposition process at higher oxygen pressures.

AUTHOR INFORMATION

Corresponding Author

*E-mail: rvchintalapalle@utep.edu.

ACKNOWLEDGMENTS

This material is based on the work supported by the Department of Energy under Award DE-PS26-08NT00198-00. A portion of the research presented in this manuscript was performed using Environmental Molecular Sciences Laboratory (EMSL), a national scientific user facility sponsored by the Department of Energy's Office of Biological and Environmental Research and located at Pacific Northwest National Laboratory.

REFERENCES

(1) Granqvist, C. G. *Handbook of Inorganic Electrochromic Materials*; Elsevier: New York, 1995.
(2) Zhang, Y.; Lee, S. H.; Mascarenhas, A.; Deb, S. K. *Appl. Phys. Lett.* **2008**, *93*, 203508.
(3) Ramana, C. V.; Utsunomiya, S.; Ewing, R. C.; Julien, C. M.; Becker, U. *J. Phys. Chem. B* **2006**, *110*, 10430.
(4) Berggren, L.; Jonsson, J. C.; Niklasson, G. A. *J. Appl. Phys.* **2007**, *102*, 083523.
(5) Lin, Y. S.; Chen, H. T.; Lai, J. Y. *Thin Solid Films* **2009**, *518*, 1377.
(6) Lu, D.; Chen, J.; Chen, H. J.; Gong, J.; Deng, S. Z.; Xu, N. S.; Liu, Y. L. *Appl. Phys. Lett.* **2007**, *90*, 041919.
(7) Lee, D. S.; Han, S. D.; Lee, D. D. *Sens. Actuators, B* **1999**, *60*, 57.
(8) Baeck, S. H.; Jaramillo, T.; Stucky, G. D.; McFarland, E. W. *Nano Lett.* **2002**, *2*, 831.

(9) Lee, D. S.; Nam, K. H.; Lee, D. D. *Thin Solid Films* **2000**, *375*, 142.
(10) Wang, L.; Teleki, S. E.; Pratsinis, S. E.; Gouma, P. I. *Chem. Mater.* **2008**, *20*, 4794.
(11) Kawasaki, H.; Namba, J.; Iwatsuji, K.; Suda, Y.; Wada, K.; Ebihara, K.; Ohshima, T. *Appl. Surf. Sci.* **2002**, *8065*, 1.
(12) Ionescu, R.; Llobet, E.; Brezmes, J.; Vilanova, X.; Correig, X. *Sens. Actuators, B* **2003**, *95*, 182.
(13) Moulzolf, S. C.; Ding, S.; Lad, R. J. *Sens. Actuators, B* **2000**, *67*, 1.
(14) Satnkova, M.; Vilanova, X.; Llobet, E.; Calderer, J.; Bittencourt, C.; Pireaux, J. J.; Correig, X. *Sens. Actuators, B* **2005**, *105*, 271.
(15) Xie, G.; Yu, J.; Chen, X.; Jiang, Y. *Sens. Actuaors, B* **2007**, *123*, 909.
(16) Santucci, S.; Cantalini, C.; Crivellari, M.; Lozzi, L.; Ottaviano, L.; Passacantanso, M. *J. Vac. Sci. Technol. A* **2000**, *18*, 1077.
(17) Gouma, P. I.; Kalyanasundaram, K. *Appl. Phys. Lett.* **2008**, *93*, 244102.
(18) Huelser, T. P.; Lorke, A.; Ifeacho, P.; Wiggers, H.; Schulz, C. *J. Appl. Phys.* **2007**, *102*, 124305.
(19) Marsen, B.; Miller, E. L.; Paluselli, D.; Rocheleau, R. E. *Int. J. Hydrogen Energy* **2007**, *32*, 3110.
(20) Paluselli, D.; Marsen, B.; Miller, E. L.; Rocheleau, R. E. *Electrochem. Solid-State Lett.* **2005**, *8*, G 301.
(21) Sun, Y.; Murphy, C. J.; Reyes-Gil, K. R.; Reyes-Garcia, E. A.; Thornton, J. M.; Morris, N. A.; Raftery, D. *Int. J. Hydrogen Energy* **2009**, *34*, 8476.
(22) Zheng, H.; Tachibana, Y.; Kalantar-Zadeh, K. *Langmuir* **2010**, *26*, 19148.
(23) Zheng, H.; Ou, J. Z.; Strano, M. S.; Kaner, R. B.; Mitchell, A.; Kalantar-Zadeh, K. *Adv. Fun. Mater* **2011**, *21*, 2175.
(24) Sahle, W.; Nygren, M. *J. Solid State Chem.* **1983**, *48*, 154.
(25) Berak, J. M.; Sienko, M. J. *J. Solid State Chem.* **1970**, *2*, 109.
(26) Salje, E.; Viswanathan, K. *Acta Crystallogr., Sect. A* **1975**, *31*, 356−359.
(27) Vogt, T.; Woodward, P. M.; Hunter, P. A. *J. Solid State Chem.* **1999**, *144*, 209.
(28) Cazzanelli, E.; Vinegoni, C.; Mariotto, G.; Kuzmin, G.; Purans, J. *J. Solid State Chem.* **1999**, *143*, 24.
(29) Chatten, R.; Chadwick, A.; Rougier, A.; Lindan, J. *J. Phys. Chem. B* **2005**, *109*, 3146.
(30) Lassner, E.; Schubert, W. D. *Tungsten: Properties, Chemistry, Technology of the Element, Alloys, and Chemical Compounds*; Kluwer Academic: New York, 1999.
(31) Cora, F.; Stachiotti, M. G.; Catlow, C. R. A.; Rodriguez, C. O. *J. Phys. Chem.* **1997**, *101*, 3945.
(32) Rao, C. N. R.; Raveau, B. *Transition Metal Oxides*; VCH: Weinheim, Germany, 1995.
(33) Chawla, A. K.; Singhal, S.; Gupta, H. O.; Chandra, R. *Thin Solid Films* **2009**, *518*, 1430.
(34) Gullapalli, S. K.; Vemuri, R. S.; Ramana, C. V. *Appl. Phys. Lett.* **2010**, *96*, 171903.
(35) Kalidindi, N. R.; Manciu, F. S.; Ramana, C. V. *ACS Appl. Mater. Interfaces* **2011**, *3*, 863.
(36) Vemuri, R. S.; Kamala Bharathi, K.; Gullapalli, S. K.; Ramana, C. V. *ACS Appl. Mater. Interfaces* **2010**, *2*, 2623.
(37) Vasilopoulou, M.; Palilis, L. C.; Georgiadou, D. G.; Argitis, P.; Kennou, S.; Kostis, I.; Papadimitropoulos, G.; Stathopoulos, N. A.; Iliadis, A. A.; Konofaos, N.; Davazoglou, D. *Thin Solid Films* **2011**, *519*, 5748.
(38) Papadimitropoulos, G.; Vourdas, N; Giannakopoulos, K.; Vasilopoulou, M.; Davazoglou, D. *J. Appl. Phys.* **2011**, *109*, 103527.
(39) Beydaghyan, G.; Bader, G.; Ashrit, P. V. *Thin Solid Films* **2008**, *516*, 1646.
(40) Gillet, M.; Aguir, K.; Lemire, C.; Gillet, E.; Schierbaum, K. *Thin Solid Films* **2004**, *467*, 239.
(41) Jerman, M.; Mergel, D. *Thin Solid Films* **2007**, *515*, 6904.
(42) Jerman, M.; Qiao, Z.; Mergel, D. *Appl. Opt.* **2005**, *44*, 3006.
(43) Mergel, D. *Thin Solid Films* **2001**, *397*, 216.
(44) Charton, P.; Gengembre, L.; Armand, P. *J. Solid State Chem.* **2002**, *168*, 175.
(45) Dupin, J. C.; Gonbeau, D.; Vinatier, P.; Levasseur, A. *Phys. Chem. Chem. Phys.* **2000**, *2*, 1319.
(46) Shpak, A. P.; Korduban, A. M.; Medvedskij, M. M.; Kandyba, V. O. *J. Electron Spectrosc. Relat. Phenom.* **2007**, *156−158*, 172.
(47) Katrib, A.; Hemming, F.; Wehrer, P.; Hilaire, L.; Maire, G. *J. Electron Spectrosc. Relat. Phenom.* **1995**, *76*, 195.
(48) Leftheriotis, G.; Papaefthimiou, S.; Yianoulis, P.; Siokou, A.; Kefalas, D. *Appl. Surf. Sci.* **2003**, *218*, 276.
(49) Kamala Bharathi, K.; Noor-A-Alam, M.; Vemuri, R. S.; Ramana, C. V. *RSC Adv.* **2012**, *2*, 941.
(50) Subrahmanyam, A.; Karuppasamy, A. *Sol. Energy Mater. Sol. Cells* **2007**, *91*, 266.
(51) Tahar, R. B. H.; Ban, T.; Ohya, Y.; Takahashi, Y. *J. Appl. Phys.* **1998**, *83*, 2631.
(52) Niklasson, G. A.; Granqvist, C. G. *J. Mater. Chem.* **2007**, *17*, 127.
(53) Koffyberg, F. P.; Dwight, K.; Wold, A. *Solid State Commun.* **1979**, *30*, 433.
(54) Vuoristo, P.; Matyla, T.; Kettunen, P.; Lappalainen, R. *Thin Solid Films* **1991**, *204*, 297.
(55) Chin, C. C.; Lin, R. J.; Yu, Y. C.; Wang, C. W.; Lin.; Tsai, W. C.; Tseng, T. C. *Physica C* **1996**, *260*, 86.
(56) Venk, T. J.; Boonekamp, E. P.; Verbeek, R. G. F. A.; Tamminga, Y. *J. Appl. Phys.* **1999**, *85*, 1540.
(57) Uthanna, S.; Subramanyam, T. K.; Srinivasulu Naidu, B.; Mohan Rao, G. *Opt. Mater.* **2002**, *19*, 461.
(58) Hashimoto, S.; Matsuoka, H. *J. Electrochem. Soc.* **1991**, *138*, 2403.
(59) Hashimoto, S.; Matsuoka, H. *Surf. Interface Anal.* **1992**, *19*, 464.

Applied Surface Science 259 (2012) 172–177

Contents lists available at SciVerse ScienceDirect

Applied Surface Science

journal homepage: www.elsevier.com/locate/apsusc

Physical properties and surface/interface analysis of nanocrystalline WO_3 films grown under variable oxygen gas flow rates

R.S. Vemuri[a,b,c], G. Carbjal-Franco[b], D.A. Ferrer[d], M.H. Engelhard[c], C.V. Ramana[a,b,*]

[a] Departments of Mechanical Engineering and Energy Science and Engineering, University of Texas at El Paso, El Paso, TX 79968, USA
[b] Department of Materials Science and Engineering, University of Texas at El Paso, El Paso, TX 79968, USA
[c] Environmental Molecular Sciences Laboratory (EMSL), Pacific Northwest National Laboratory (PNNL), Richland, WA 99352, USA
[d] Department of Chemical Engineering, University of Texas at Austin, Austin, TX 78758, USA

ARTICLE INFO

Article history:
Received 17 October 2011
Received in revised form 24 June 2012
Accepted 4 July 2012
Available online 14 July 2012

Keywords:
WO_3 thin films
Microstructure
Density
Surface/interface structure
X-ray reflectivity
Electron microscopy

ABSTRACT

Nanocrystalline WO_3 films were grown by reactive magnetron sputter-deposition in a wide range of oxygen gas flow rates while keeping the deposition temperature fixed at 400 °C. The physical characteristics of WO_3 films were evaluated using grazing incidence X-ray diffraction (GIXRD), X-ray reflectivity (XRR), and transmission electron microscopy (TEM) measurements. Physical characterization indicates that the thickness, grain size, and density of WO_3 films are sensitive to the oxygen gas flow rate during deposition. XRD data indicate the formation of tetragonal WO_3 films. The grain size increases from 21 to 25 nm with increasing oxygen gas flow rate to 65%, at which point the grain size exhibits a decreasing trend to attain the lowest value of 15 nm at 100% oxygen. TEM analysis provides a model consisting of isotropic WO_3 film (nanocrystalline)–SiO_2 interface (amorphous)–Si(1 0 0) substrate. XRR simulations, which are based on this model, provide excellent agreement to the experimental data indicating that the normalized thickness of WO_3 films decreases with the increasing oxygen gas flow rate. The density of WO_3 films increases with increasing oxygen gas flow rate.

1. Introduction

Tungsten oxide (WO_3) is an interesting "chromogenic" material because of the coloration effects associated with various processes [1–6]. Current interest in WO_3 low-dimensional structures includes a wide variety of applications in optoelectronics, microelectronics, selective catalysis, and environmental engineering [2–20]. WO_3 films find application in the development of smart windows, flat-panel displays, optical memory and writing–reading–erasing devices, and electronic information displays [1–6]. WO_3 films exhibit gas sensing properties, which will have numerous applications in environmental and industrial pollution monitoring [7–18]. WO_3 films exhibit excellent functional activity to various gases, such as H_2S, NO_x, trimethylamine, and other organics, and are suitable for integrated sensors [13–18]. Recently, WO_3 based materials are also attracting the attention for application in photoelectrochemical cells (PECs) [19–21] and dye-sensitized solar cells (DSSCs) technology [22]. A review of structure, synthesis, and application of nanostructured WO_x materials is documented in a recent review article where the opportunities and scope for further exploitation of nanostructured WO_3 materials are convincing [23].

WO_3 is a complicated material with respect to crystal structure and thermal stability because of several structures, such as monoclinic, triclinic, tetragonal, orthorhombic, cubic, and hexagonal for pure and oxygen deficient WO_3 [24–28]. At room-temperature, WO_3 crystallizes in a triclinic structure and exhibit structural transformation at higher temperatures. Investigations on bulk WO_3 report the following sequence: triclinic (~30 °C) → monoclinic (330 °C) → orthorhombic (740 °C) → tetragonal [24–29]. Formation of pyrochlore WO_3 structure at about 373 K has been reported [30]. The ideal WO_3 crystal structure can be represented as a cubic ReO_3 structure [31,32]. In fact, the polymorphs of WO_3 can be described as distortions from the cubic ReO_3 structure [24–29]. The characteristic feature of the structure is that the cation is surrounded by an octahedral arrangement of oxygen atoms. Therefore, the structure is built up from a three-dimensional network of corner-sharing MO_6 (M = W or Re) octahedra as shown in Fig. 1 for WO_3. The octahedral environment of W is shown in Fig. 1b. The crystal structure of WO_3 can be viewed as alternating planes of O and WO_2 (Fig. 1b). The planes of O and WO_2 can be viewed as placed normal to the respective crystallographic direction. However, WO_3 thin films prepared by a wide variety of chemical and physical techniques employing various processing conditions usually possess different microstructures, properties, and phenomena [1–17,33–41].

* Corresponding author at: Departments of Mechanical Engineering and Energy Science and Engineering, University of Texas at El Paso, El Paso, TX 79968, USA.
E-mail address: rvchintalapalle@utep.edu (C.V. Ramana).

0169-4332/$ – see front matter © 2012 Elsevier B.V. All rights reserved.
http://dx.doi.org/10.1016/j.apsusc.2012.07.014

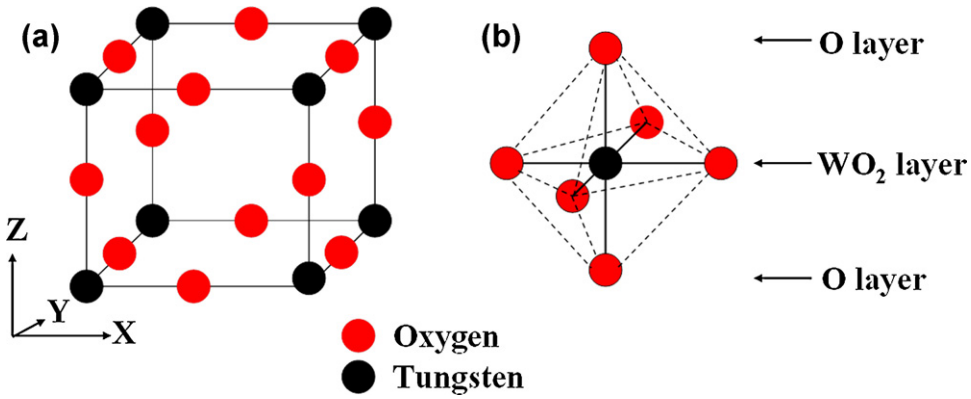

Fig. 1. The structure of WO_3. (a) The ideal cubic structure of WO_3. (b) The WO_6 octahedra. The alternating WO_2 and O layers are also indicated.

The controlled growth and manipulation of specific crystal structures at the nanoscale dimensions has important implications for the design and applications of WO_3 films. However, the ability to tailor the properties so as to optimize performance requires a detailed understanding of the relationship between electronic and geometric structure, particularly at the nanoscale dimensions. Furthermore, stabilizing metastable high-temperature phases in a controlled way requires detailed understanding of the structural transformation induced changes in the electronic properties of nanocrystalline WO_3 films. Therefore, it is important to characterize and obtain detailed information on the physical and surface/interface structural characteristics of WO_3 films as a function of growth conditions. The present work was, therefore, performed on sputter-deposited nanocrystalline WO_3 films under varying the oxygen partial pressure at a fixed deposition temperature. Earlier we reported on the effect of deposition temperature on the microstructure and electrical properties nanocrystalline WO_3 films [34,36]. We found that the effect of growth temperature is significant on the structure, phase, grain-size, and electrical conductivity of nanocrystalline WO_3 films [34–36]. The objective of the present work is to derive a detailed understanding of the physical characteristics, such as crystal structure, film thickness, grain size, and density variation, which will have profound influence on the electronic properties and device performance of WO_3 films. The results obtained on the effect of oxygen gas flow rate during deposition of nanocrystalline WO_3 films is presented and discussed in this paper.

2. Experimental

2.1. Fabrication

WO_3 thin films were deposited onto silicon (Si) (1 0 0) wafers by radio-frequency (RF) (13.56 MHz) magnetron sputtering. All the substrates were thoroughly cleaned, using the standard procedure reported elsewhere [34–36], and dried with nitrogen before introducing them into the vacuum chamber, which was initially evacuated to a base pressure of $\sim 10^{-6}$ Torr. Tungsten (W) metal target (Plasmaterials Inc.) of 2 in. diameter and 99.95% purity was employed for reactive sputtering. The W-target was placed on a 3-in. sputter gun, which is placed at a distance of 8 cm from the substrate. A sputtering power of 40 W was initially applied to the target while introducing high purity argon (Ar) into the chamber to ignite the plasma. Once the plasma was ignited the power was increased to 100 W and oxygen (O_2) was released into the chamber for reactive deposition. The flow of the Ar and O_2 and their ratio was controlled using as MKS mass flow meters. Before each deposition, the W-target was pre-sputtered for 10 min using Ar alone with shutter above the gun closed. The samples were deposited by varying the oxygen concentration while keeping the deposition temperatures (T_S) fixed at 400 °C. Specifically, the oxygen gas fractionation ratio [$\Gamma = O_2/Ar + O_2$] is varied in a wide range in order to study the effect of oxygen gas flow rate of the structural characteristics of WO_3 films. The deposition was made for a constant time of 60 min. The substrates were heated by halogen lamps and the desired temperature was controlled by Athena X25 controller.

2.2. Characterization

X-ray diffraction (XRD) measurements on WO_3 films were performed using a Bruker D8 Advance X-ray diffractometer. All the measurements were made ex situ as a function of growth temperature. XRD patterns were recorded using Cu Kα radiation (λ = 1.54056 Å) at RT. In addition, high resolution scans of selected individual diffraction peaks were obtained. The high resolution data of selected peaks were obtained with the step size of 0.001°/s. The coherently diffracting domain size (D_{hkl}) was calculated from the integral width of the diffraction lines using the well known Scherrer's equation after background subtraction and correction for instrumental broadening. The Scherrer equation [42] is:

$$D_{h\,k\,l} = \frac{0.9\lambda}{\beta \cos\theta} \quad (1)$$

where D_{hkl} is the size, λ is the wavelength of the filament used in the XRD machine, β is the width of a peak at half of its intensity, and θ is the angle of the peak. X-ray reflectivity (XRR) measurements were performed in the same machine. All the measurements were made ex situ as a function of partial pressure. The thickness and density calculation were performed by fitting the XRR data using LEPTOS® software. The film thickness was obtained by the period of oscillations in the XRR curve. The film-density was determined by the position of total reflection edge. The transmission electron microscopy (TEM) experiments were performed in a FEI Tecnai TF20 (200 kV) equipped with a STEM unit, high-angle annular dark-field (HAADF) detector and X-Twin lenses. Cross-section of samples (WO_3 films grown on Si) for TEM were prepared by using a dual beam System (FIB/SEM) FEI Strata 235, employing 30 kV Ga^+ ions, with a final beam current of ~50 pA. Samples were then plasma cleaned for 7 min in a South Bay Technology PC200 system on a Ar/O_2 ambient and subsequently introduced into the TEM measurements.

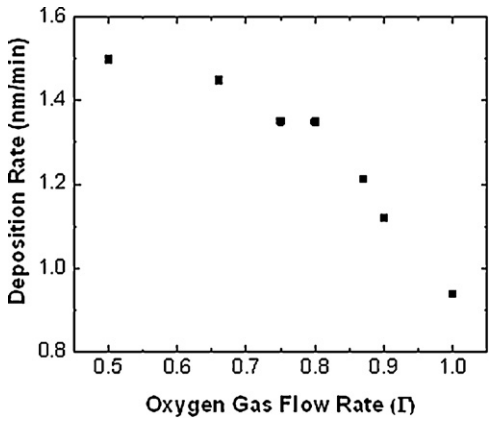

Fig. 2. The variation of the deposition rate of WO_3 films with oxygen gas flow rate. The experimental data are shown with solid squares while the solid line represents a fit to an exponential decay function. A decrease in deposition rate with increasing Γ is evident.

3. Results and discussion

3.1. Growth rate and film thickness

The physical examination of the grown films under varying oxygen flow rates indicates that the WO_3 layers are uniform and transparent. The layers exhibit a good adhesion with no mechanical defects, such as cracks. The surface chemical composition of the WO_3 films was studied employing X-ray photoelectron spectroscopy (XPS). The results and detailed analysis of XPS data have been reported elsewhere [41]. Briefly, XPS data indicate that the WO_3 films are stoichiometric within a certain range of oxygen content in the reactive gas mixture while it becomes overstoichiometric for higher oxygen content ($\Gamma > 0.6$). The chemical state of tungsten ions is determined to be as W^{6+} while the O 1s core level is symmetric for all the samples reflecting the characteristic feature of O atoms bonded with W atoms only [41].

The variation of the growth rate of WO_3 films with oxygen flow rate is shown in Fig. 2. A decrease in deposition rate with increasing oxygen gas flow rate is evident. A closer examination of the data indicates two characteristic features of the dependence of WO_3 growth on the oxygen gas flow rate. For the given set of constant conditions i.e., sputter-power and deposition temperature, the changes in the deposition rate is not significant for the initial increase in oxygen gas flow rate. However, the growth rate decreases significantly at higher oxygen flow rate. This behavior is more dominant in the range of oxygen gas flow rate $\Gamma > 0.75$. The observed behavior can be explained based on the effect of oxygen pressure and the effective number of species ejected from target surface and the effective number of particles reaching and attaining the substrate. Increasing oxygen pressure reduces the energy that the particles attain to the substrate and their mobility, making it more difficult for the sputtering species to bombard the substrate and, thus, leading to decreasing growth rate of the film [43–45]. It must be pointed out that during sputtering process, the target species are subjected to collisions with ambient gas molecules and other ejected atoms. This results in a partial loss of energy and direction on their way making it more difficult to attain the substrate [45,46]. The reactive sputter-gas, therefore, impedes the mobility and trajectory of sputtered species. Furthermore, at a given or constant sputter-power, increasing oxygen pressure in the plasma shifts the thermalization region toward the target [46]. As a result, oxidation of the W-target takes place leading to a decrease in deposition rate of WO_3 films. Re-sputtering of the grown film cannot be ruled at higher oxygen pressures that could potentially decrease the overall film thickness and, hence, the growth rate. A faster decrease in the growth rate of WO_3 films at higher oxygen flow rates (Fig. 2) can, therefore, be attributed to the combined effect of target oxidation, sputter-ejected species being impeded and decrease in the mean free path, and partial re-sputtering of the film.

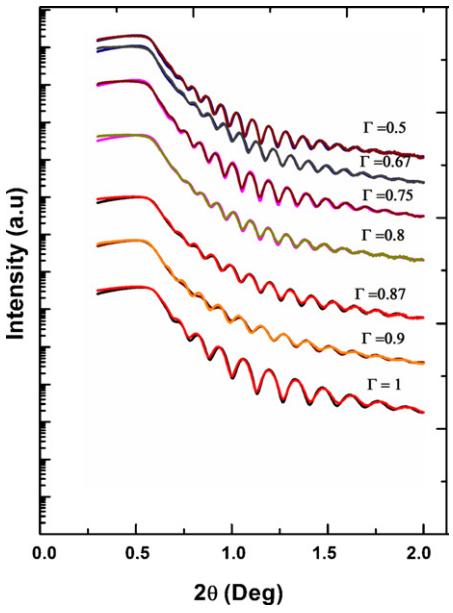

Fig. 3. The XRR patterns of nc-WO_3 films as a function of oxygen gas flow rates. Experimental and simulation curves are shown.

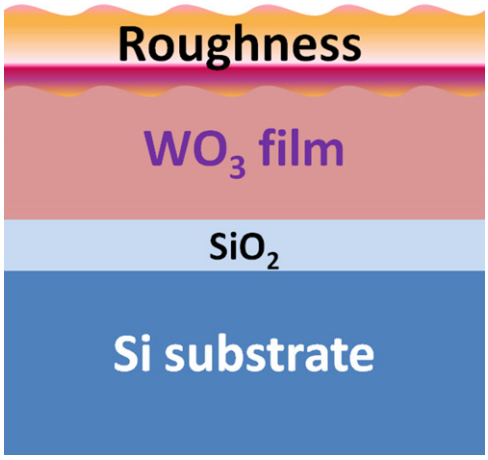

Fig. 4. The stack model used to simulate the XRR spectra. The model contains WO_3 film, SiO_2 interface, and Si substrate as indicated.

3.2. Film density and surface/interface structure

The XRR patterns of nc-WO_3 films are shown in Fig. 3 as a function of oxygen pressure. Simulation of the XRR experimental data using appropriate model can provide physio-chemical information of the nc-WO_3 films. Specifically, the surface and interface roughness, thickness, and density of the WO_3 films can be obtained from XRR spectra [47,48]. The density can be obtained from the total reflection or critical edge [48]. Film thickness can be derived from the period of the oscillations in the XRR spectra [47,48]. It is evident that the experimental and simulation curves are in excellent agreement. The stack model used to simulate the spectra is shown in Fig. 4. The model contains, from top, WO_3 film, SiO_2 interface, and Si substrate. The surface and interface roughness were also

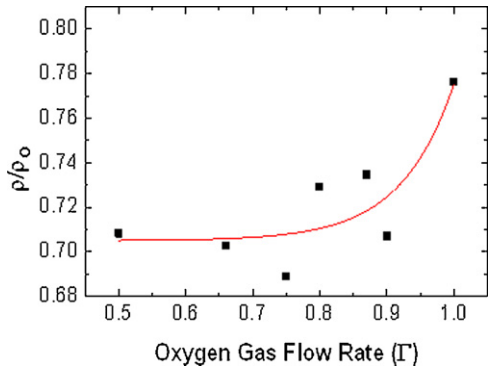

Fig. 5. Normalized density variation of WO_3 films with oxygen gas flow rate.

considered in order to accurately fit the experimental XRR spectra of WO_3 films. The model constructed is based on the TEM observations of the sample's cross-section as discussed later below. The following observations can be made from the XRR spectra (Fig. 3). A positive shift (higher angle) of the critical edge with increasing oxygen flow rate is the first. The oscillations extend toward higher angle (>2°) is the second. The later observation indicates that the film roughness is not very high. The positive shift of the critical edge indicates an increase in the film density with increasing oxygen flow rate. The results obtained are shown in Fig. 5. The variation of normalized density of nc-WO_3 films with oxygen flow rate along with a model is shown. The data are normalized using the theoretical density of bulk WO_3. It can be noted that the WO_3 films grown at $\Gamma = 0.5$ is only about 70% of theoretical density of bulk WO_3.

The high-resolution TEM micrographs of a representative WO_3 film on Si(1 0 0) is shown in Fig. 6. The existence of an interfacial layer between the grown WO_3-film and Si-substrate is evident in the HRTEM image. TEM measurements confirm the thickness of the WO_3 films. The film, interface, and substrate regions are as indicated in Fig. 6. The very-high magnification images obtained from HRTEM in the areas along with the WO_3 film region are shown in a separate image (Fig. 6b). The regions used for obtaining the high-resolution magnification images are shown. It can be seen that the images obtained exhibit the lattice-fringes, which corresponds to the crystallized WO_3 films. The direct observation of the cross-sectional structure of WO_3 films on Si using TEM data allows constructing the stack model used in XRR data analysis and simulation. The lattice fringes are due to diffraction from (0 0 1) and (2 0 0) planes. The inter-planar distances of 3.88 Å and 3.695 Å for

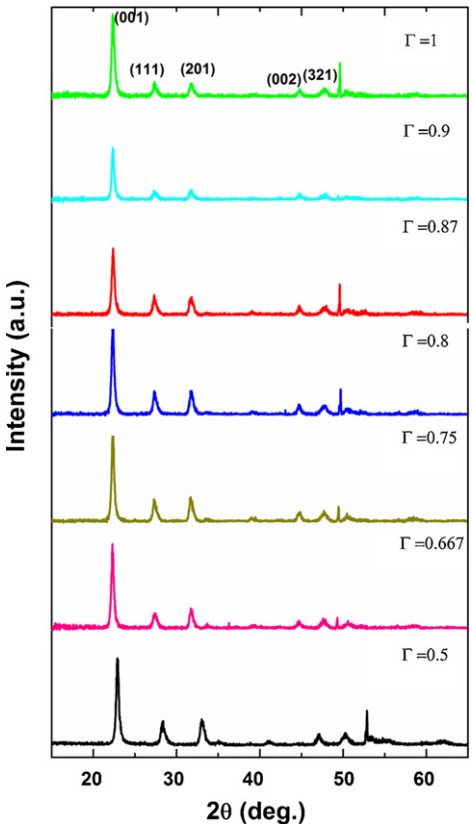

Fig. 7. XRD patterns of WO_3 films as function of oxygen gas flow rates.

(0 0 1) and (2 0 0) planes, respectively, are in good agreement with the tetragonal phase of WO_3. The structure of WO_3 films as determined from XRD confirms the tetragonal phase formation in WO_3 films grown under various oxygen flow rates.

3.3. Crystal structure

The XRD patterns of WO_3 films as function of variable oxygen gas flow rates are shown in Fig. 7. The structural characterization using XRD and phase analysis of WO_3 films grown at various temperatures have been reported elsewhere [34,36]. Briefly, WO_3 films grown at RT were amorphous transforming to monoclinic WO_3 with increasing substrate temperature to 200 °C. WO_3 films grown

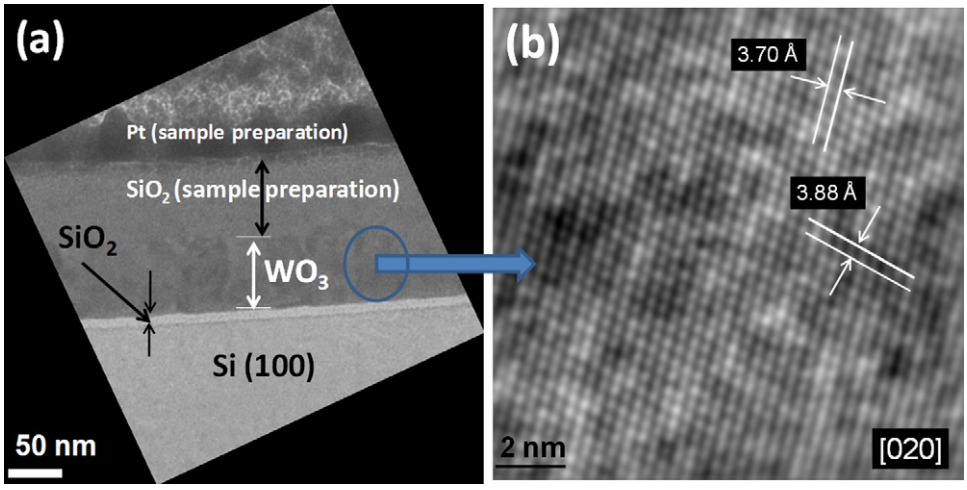

Fig. 6. TEM micrograph of WO_3 films grown at $\Gamma = 0.9$. The film, interface, and substrate regions are as indicated.

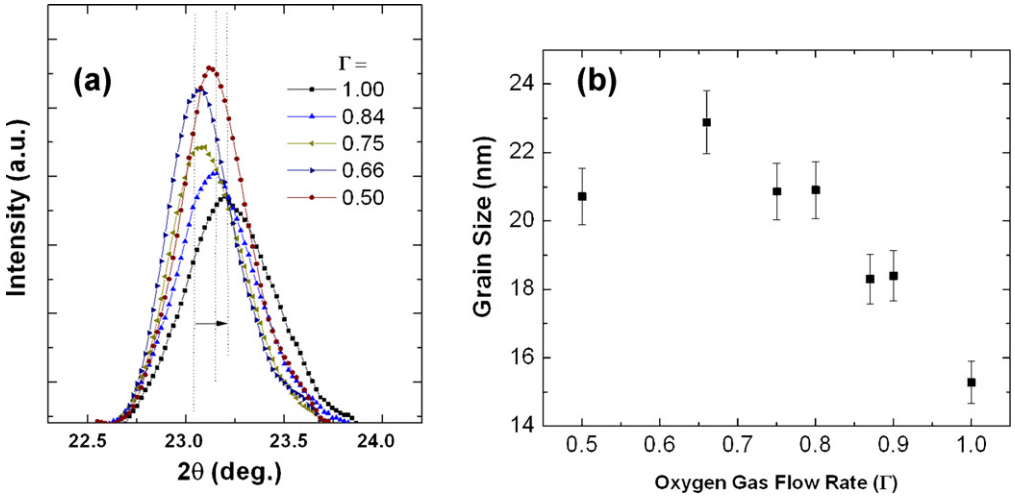

Fig. 8. Grain size dependence of WO_3 films on oxygen gas flow rate.

at further higher temperatures, specifically at $T_s \geq 400\,^{\circ}C$, structural transformation occurs again leading to the formation of strained tetragonal phase. High-temperature tetragonal phase formation of WO_3 at 400 °C was attributed to the effect of phase stabilization at the nanoscale dimensions [34,36]. The preferred *c*-axis orientation was due to the growth process minimizing the internal strain-energy in the film. The high-resolution scans of (0 0 1) peak as a function oxygen gas flow rate are shown in Fig. 8a. It can be seen that increasing oxygen flow rate slightly broadens the (0 0 1) peak in addition to the slight shift in the peak position. This observation indicates that the films grown at higher oxygen gas flow rates may have the decreased particle size coupled with the presence of strain, Perhaps, oxygen may be trapped when there is excess oxygen gas flow during deposition. The grain size, determined from XRD, variation with oxygen flow rate is shown in Fig. 8b. It is evident that the grain size gradually decreases with increasing oxygen flow rate. The grain size increases from 21 to 25 nm with increasing Γ to 0.65, at which point the grain size exhibits a decreasing trend to attain the lowest value of 15 nm at $\Gamma = 1$. This observation indicates that the increase in oxygen gas flow decreases the mobility of the adatoms on the surface leading to a decrease in grain size. The correlation between optical structural characteristics and optical properties of these WO_3 films were discussed in detail elsewhere [41]. It was noted that the spectral transmission and band gap of the WO_3 films increases with the increasing oxygen content in the reactive gas mixture. The band gap increases from 2.75 eV to 3.25 eV with increasing oxygen concentration. While we attribute the increased band gap to the excess oxygen, the detailed studies in the physical characteristics indicate that the band gap increase is due to excess oxygen coupled with smaller crystallite size and stress in the films.

4. Conclusions

Nanocrystalline WO_3 films were grown by reactive magnetron sputter-deposition by varying the oxygen gas flow rate. The effect of oxygen gas flow rate on the crystal structure, thickness, surface and interface structure and morphology, density, and grain size of WO_3 films is evaluated. Nanocrystalline WO_3 films crystallize in tetragonal phase with *c*-axis oriented growth. However, the shift in the (0 0 1) peak suggests increasing strain in the WO_3 films due to excess oxygen incorporation at higher oxygen gas flow rates. The grain size increases from 21 to 25 nm with increasing Γ to 0.65, at which point the grain size exhibits a decreasing trend to attain the lowest value of 15 nm at $\Gamma = 1$, which indicates that the increase in oxygen gas flow decreases the mobility of the adatoms on the film surface. XRR data indicate that the thickness of WO_3 films decreases with the increasing Γ values. The density of WO_3 films increases from 70 to 78% with increasing oxygen gas flow rate.

Acknowledgements

This material is based upon the work supported by the Department of Energy under Award Number DE-PS26-08NT00198-00. A portion of the research was performed using Environmental Molecular Sciences Laboratory (EMSL), a national scientific user facility sponsored by the Department of Energy's Office of Biological and Environmental Research and located at Pacific Northwest National Laboratory.

References

[1] C.G. Granqvist, Handbook of Inorganic Electrochromic Materials, Elsevier, New York, 1995.
[2] Y. Zhang, S.H. Lee, A. Mascarenhas, S.K. Deb, Applied Physics Letters 93 (2008) 203508.
[3] C.V. Ramana, S. Utsunomiya, R.C. Ewing, C.M. Julien, U. Becker, Journal of Physical Chemistry B 110 (2006) 10430.
[4] L. Berggren, J.C. Jonsson, G.A. Niklasson, Journal of Applied Physics 102 (2007) 083523.
[5] Y.S. Lin, H.T. Chen, J.Y. Lai, Thin Solid Films 518 (2009) 1377.
[6] D. Lu, J. Chen, H.J. Chen, J. Gong, S.Z. Deng, N.S. Xu, Y.L. Liu, Applied Physics Letters 90 (2007) 041919.
[7] D.S. Lee, S.D. Han, D.D. Lee, Sensors and Actuators B 60 (1999) 57–63.
[8] S.H. Baeck, T. Jaramillo, G.D. Stucky, E.W. McFarland, Nano Letters 2 (2002) 831–834.
[9] D.S. Lee, K.H. Nam, D.D. Lee, Thin Solid Films 375 (2000) 142–147.
[10] L. Wang, S.E. Teleki, S.E. Pratsinis, P.I. Gouma, Chemistry of Materials 20 (2008) 4794–4796.
[11] H. Kawasaki, J. Namba, K. Iwatsuji, Y. Suda, K. Wada, K. Ebihara, T. Ohshima, Applied Surface Science 8065 (2002) 1–5.
[12] R. Ionescu, E. Llobet, J. Brezmes, X. Vilanova, X. Correig, Sensors and Actuators B 95 (2003) 177–182.
[13] S.C. Moulzolf, S. Ding, R.J. Lad, Sensors and Actuators B 67 (2000) 1.
[14] M. Satnkova, X. Vilanova, E. Llobet, J. Calderer, C. Bittencourt, J.J. Pireaux, X. Correig, Sensors and Actuators B 105 (2005) 271.
[15] G. Xie, J. Yu, X. Chen, Y. Jiang, Sensors and Actuators B 123 (2007) 909.
[16] S. Santucci, C. Cantalini, M. Crivellari, L. Lozzi, L. Ottaviano, M. Passacantanso, Journal of Vacuum Science & Technology A 18 (2000) 1077.
[17] P.I. Gouma, K. Kalyanasundaram, Applied Physics Letters 93 (2008) 244102.
[18] T.P. Huelser, A. Lorke, P. Ifeacho, H. Wiggers, C. Schulz, Journal of Applied Physics 102 (2007) 124305.
[19] B. Marsen, E.L. Miller, D. Paluselli, R.E. Rocheleau, International Journal of Hydrogen Energy 32 (2007) 3110.
[20] D. Paluselli, B. Marsen, E.L. Miller, R.E. Rocheleau, Electrochemical and Solid-State Letters 8 (2005) G301.
[21] Y. Sun, C.J. Murphy, K.R. Reyes-Gil, E.A. Reyes-Garcia, J.M. Thornton, N.A. Morris, D. Raftery, International Journal of Hydrogen Energy 34 (2009) 8476.
[22] H. Zheng, Y. Tachibana, K. Kalantar-Zadeh, Langmuir 26 (2010) 19148.

[23] H. Zheng, J.Z. Ou, M.S. Strano, R.B. Kaner, A. Mitchell, K. Kalantar-Zadeh, Advanced Functional Materials 21 (2011) 2175.
[24] W. Sahle, M. Nygren, Journal of Solid State Chemistry 48 (1983) 154–160.
[25] J.M. Berak, M.J. Sienko, Journal of Solid State Chemistry 2 (1970) 109–133.
[26] E. Salje, K. Viswanathan, Acta Crystallographica A 31 (1975) 356–359.
[27] T. Vogt, P.M. Woodward, P.A. Hunter, Journal of Solid State Chemistry 144 (1999) 209.
[28] E. Cazzanelli, C. Vinegoni, G. Mariotto, G. Kuzmin, J. Purans, Journal of Solid State Chemistry 143 (1999) 24.
[29] R. Chatten, A. Chadwick, A. Rougier, J. Lindan, Journal of Physical Chemistry B 109 (2005) 3146.
[30] E. Lassner, W.-D. Schubert, Tungsten: Properties, Chemistry, Technology of the Element, Alloys, and Chemical Compounds, Kluwer Academic, New York, 1999.
[31] F. Cora, M.G. Stachiotti, C.R.A. Catlow, C.O. Rodriguez, Journal of Physical Chemistry 101 (1997) 3945.
[32] C.N.R. Rao, B. Raveau, Transition Metal Oxides, VCH Publ., 1995.
[33] A.K. Chawla, S. Singhal, H.O. Gupta, R. Chandra, Thin Solid Films 518 (2009) 1430.
[34] S.K. Gullapalli, R.S. Vemuri, C.V. Ramana, Applied Physics Letters 96 (2010) 171903.
[35] N.R. Kalidindi, K. Kamala Bharathi, C.V. Ramana, Applied Physics Letters 97 (2010) 142107.
[36] R.S. Vemuri, K. Kamala Bharathi, S.K. Gullapalli, C.V. Ramana, ACS Applied Materials & Interfaces 2 (2010) 2623.
[37] M. Vasilopoulou, L.C. Palilis, D.G. Georgiadou, P. Argitis, S. Kennou, I. Kostis, G. Papadimitropoulos, N.A. Stathopoulos, A.A. Iliadis, N. Konofaos, D. Davazoglou, Thin Solid Films 519 (2011) 5748.
[38] G. Papadimitropoulos, N. Vourdas, K. Giannakopoulos, M. Vasilopoulou, D. Davazoglou, Journal of Applied Physics 109 (2011) 103527.
[39] G. Beydaghyan, G. Bader, P.V. Ashrit, Thin Solid Films 516 (2008) 1646.
[40] M. Gillet, K. Aguir, C. Lemire, E. Gillet, K. Schierbaum, Thin Solid Films 467 (2004) 239.
[41] R.S. Vemuri, M.H. Engelhard, C.V. Ramana, ACS Applied Materials & Interfaces 4 (2012) 1371.
[42] B.D. Cullity, S.R. Stock, Elements of X-ray Diffraction, Prentice Hall, 2001.
[43] O. Kappertz, R. Drese, J.M. Ngaruiya, M. Wuttig, Thin Solid Films 484 (2005) 64.
[44] M. Buchanan, J.B. Webb, D.F. Williams, Thin Solid Films 81 (1981) 371.
[45] R.B.H. Tahar, T. Ban, Y. Ohya, Y. Takahashi, Journal of Applied Physics 83 (1998) 2631.
[46] E. Leja, A. Kolodiez, T. Pisarkiewiez, T. Stapinski, Thin Solid Films 81 (1976) 283.
[47] S. Bernstorff, P. Dubček, B. Pivac, I. Kovačević, A. Sassella, A. Borghesi, Applied Surface Science 253 (2006) 33.
[48] K. Kamala Bharathi, R.S. Vemuri, M. Noor-A-Alam, C.V. Ramana, Thin Solid Films 520 (2012) 1794.

Spectroscopic analysis of tungsten oxide thin films

Felicia S. Manciu,[a] Jose L. Enriquez, William G. Durrer, and Young Yun
Department of Physics, University of Texas at El Paso, El Paso, Texas 79968

Chintalapalle V. Ramana and Satya K. Gullapalli
Department of Mechanical Engineering, University of Texas at El Paso, Texas 79968

(Received 2 March 2010; accepted 14 July 2010)

We present a detailed study of the morphology and composition of tungsten oxide (WO_3) thin films, grown by radio frequency magnetron reactive sputtering at substrate temperatures varied from room temperature (RT) to 500 °C, using infrared (IR) absorption, Raman spectroscopy, and x-ray photoelectron spectroscopy (XPS). This work includes valuable new far-IR results about structural changes in microcrystalline WO_3. Both IR absorption and Raman techniques reveal an amorphous sample grown at RT and initial crystallization into monoclinic structures for samples grown at temperatures between 100 and 300 °C. The Raman spectra of the samples grown at high temperatures indicate, apart from the monoclinic structure, a strain effect, with a distribution revealed by confocal Raman mapping. XPS indicates that the film surface maintains the stoichiometry WO_x, with a value of x slightly greater than 3 at RT due to oxygen contamination, which decreases with increasing temperature.

I. INTRODUCTION

Tungsten oxide (WO_3) has been extensively investigated, especially in the form of thin films, where controlling material characteristics such as crystallinity, grain size, nano- and micro-porosity, stoichiometry, and surface reactivity can be used to enhance its photochromic,[1–3] electrochromic,[3–6] thermochromic,[7,8] and gasochromic[9,10] properties. Important reasons for the impressive amount of research dedicated to this metal oxide are its unique properties, which consist of relatively high melting point, diverse, but thermodynamically stable structures with variations in temperature and pressure growth conditions, and low-cost manufacturing procedures. In addition, the high compatibility of WO_3 with microelectronic processing and ease of integration into portable devices with the characteristics of low power consumption and online operation, have resulted in its extensive use in nanotechnology applications. It is a primary candidate for use in photocatalysts, anti-dazzle mirrors, smart windows, and gas sensing devices.[10–14]

In order to achieve stable, selective, and reliable devices, accurate preparation of the functional material is crucial; many factors must be taken into account to warrant homogeneous WO_3 grain characteristics such as shape and size, distribution, porosity, and surface conditions. This is a consequence of the fact that, despite the simplicity of the principle and use of metal oxides for industrial purposes, the actual mechanism is quite complex and not yet fully understood in a way that allows total control in a confinement regime. Thus, fundamental investigations of WO_3 at the nano- and micro-scale, where structural defects and perturbation of the electronic structure often arise, need particular attention. Abundant theoretical and experimental forecasts of properties of this compound, in its standard and doped form, are available in the literature, revealing that thin-film structures of WO_3 exhibit various phases depending on the thermodynamic parameters (temperature and reactive pressure) used for their growth.[2,7,15] For example, triclinic, monoclinic, orthorhombic, tetragonal, and hexagonal crystalline phases of WO_3 have been reported for temperatures between absolute zero and its melting point at about 1400 °C.[2,7,15]

Since individual nanostructures are not only small in size, but often present in low yield and as mixtures of different phases, sensitive spectroscopy tools are required to study them. In this context, we present here detailed experimental infrared absorption, confocal Raman, and x-ray photoelectron spectroscopic (XPS) results, which demonstrate the effect of growth temperature on the morphological evolution of WO_3 thin films. Apart from standard structural and microscopic characterizations by x-ray diffraction (XRD), scanning electron microscopy (SEM), and atomic force microscopy (AFM),[15–18] spectroscopic analytical techniques have also proven to be valuable,[19–21] especially for obtaining information about the local structure (e.g., by using Raman mapping) and the chemical bonding of the stoichiometric polycrystalline films.

[a]Address all correspondence to this author.
e-mail: fsmanciu@utep.edu
DOI: 10.1557/JMR.2010.0294

While structural changes in microcrystalline WO_3 have been investigated predominantly by means of Raman scattering spectroscopy at low frequencies and under ambient or high-pressure conditions,[19,20] much less structural change information is available from far infrared (FIR) absorption analysis. As will be proven in this work, the FIR region is important as it complements the Raman measurements in frequency domains where the peaks are associated with lattice modes of the relative translational or rotational motions of WO_6 octahedral units forming the unit cell (for frequencies less than 200 cm^{-1}) and with O-W-O bending modes (for frequencies between 200 and 400 cm^{-1}). Considering that, with respect to the ideal ReO_3 cubic structure, the symmetry of WO_3 is lowered by two distortions that contribute to material phase transitions, namely, the tilting of the WO_6 octahedra and the displacement of the tungsten from the center of its octahedron, determination of possible structural phase modifications is feasible only in the FIR region. Distinguishing between different crystalline phases of WO_3 in the higher frequency region (400–900 cm^{-1}), which is characteristic of W-O stretching modes, is very difficult since their predicted IR and Raman predicted vibrations have very similar frequencies that, usually, are not experimentally resolved.

Also, the confocal Raman mapping measurements that were performed here allow us to associate the spectroscopic data with specific nano- and micro-scale features and to confirm the coexistence of different crystalline phases. This information is particularly critical for complex, heterogeneous samples, since modification of the chemical or physical synthesis route within the same general sample preparation method can influence the properties of the grown material.

II. EXPERIMENTAL PROCEDURE

In the present work, radio frequency (RF) magnetron reactive sputtering was used to deposit the WO_3 thin films on Si(100) wafer and sapphire substrates, which were mounted at 8 cm from a 3″ diameter W metal target (Plasmaterials, Inc., Livermore, CA) of 99.95% purity. The Si(100) substrates were thoroughly cleaned with RCA and dried with nitrogen before introducing them into the vacuum chamber. A similar cleaning treatment, but with isopropyl alcohol, was performed on the sapphire substrates. After evacuating the cryopumped deposition chamber to a base pressure of 10^{-6} Torr, high purity Ar was introduced into the chamber while holding the sputtering power at 40 W to achieve plasma ignition. Then the power was increased to 100 W and the W target was pre-sputtered for 10 min in Ar with a closed shutter between the source and substrate. A reactive deposition was reached by opening the shutter and releasing O_2 into the chamber. The sputtering atmosphere consisted of Ar-O_2 mixed gases and their flow rates were controlled with MKS mass flow meters to provide an optimum Ar:O_2 flow ratio of 1:6. Deposition temperatures at the substrates were set by heating the substrates with halogen lamps and controlled with an Athena X25 temperature controller. Each deposition was timed at 1 h, but different samples were produced at different substrate temperatures, which varied from room temperature (RT) to 500 °C. These parameters of the deposition process led to a total thickness of each WO_3 film of about 80 nm.[22]

The Raman measurements were acquired at ambient conditions, whereas a Bruker IFS 66v FTIR spectrometer, a vacuum-based system, was used for IR absorption experiments. Each IR spectrum resulted from an accumulation of 256 scans at a resolution of 4 cm^{-1}. Raman spectroscopy was performed with an alpha 300 WITec confocal Raman system, using the 532 nm excitation of a Nd:YAG laser. An acquisition time of 5 s for each spectrum and a 100× objective lens with NA = 0.95 was used in all experiments.

The binding energies of the atomic constituents and their chemical oxidation states were evaluated through XPS measurements, which were performed on sample surfaces using Mg K_a x-rays in a Perkin-Elmer Phi 560 ESCA/SAM system.

III. RESULTS AND DISCUSSION

The IR absorption measurements of the WO_3 thin films grown at Si substrate temperatures between RT (top spectrum) and 500 °C (bottom spectrum), are presented in Figs. 1(a)–1(c). The spectra in the region of 480 to 1200 cm^{-1} [Figs. 1(b) and 1(c)] show absorption lines at 731 and 815 cm^{-1}, which are ascribed to W-O

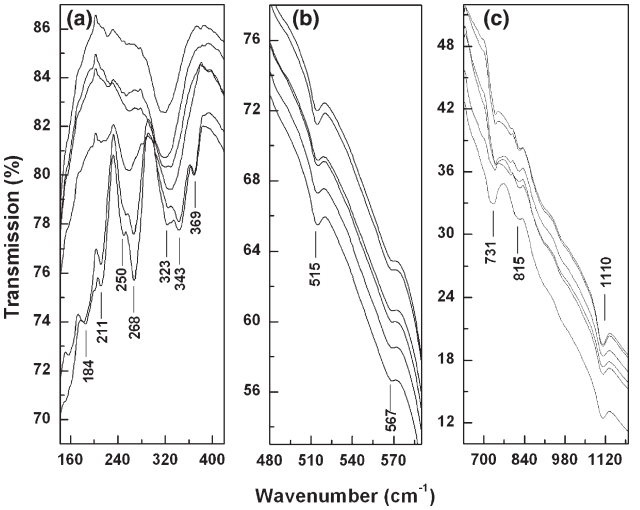

FIG. 1. (a)–(c) Infrared absorption spectra of WO_3 samples grown at different temperatures. For easier visualization, the spectra are vertically translated with the RT spectrum at the top and the 500 °C spectrum at the bottom.

stretching vibrations.[21,23] Their very slight increase in intensities suggests an increase in material crystallization with increasing temperature. The unwanted but conspicuous presence of Si-O bonds is also observed at 515 and 567 cm^{-1} (symmetric Si-O-Si vibration) and 1110 cm^{-1} (asymmetric Si-O-Si vibration). It is well known that an Si wafer will always be covered by a very thin SiO_2 layer due to the high Si oxidation rate.

The more interesting behavior of these samples is seen in the FIR absorption region [Fig. 1(a)]. While the spectra recorded for a growth temperature of less than 200 °C exhibit only a broad intense band at 317 cm^{-1} and very weak features around 224 and 256 cm^{-1}, a multitude of vibrational lines at 184, 211, 250, 268, 323, 343, and 369 cm^{-1} is observed for the samples grown at 400 and 500 °C. Also, in the spectrum of the WO_3 sample grown at 300 °C, there is an evident increase in the intensities of the absorption features at 224 and 256 cm^{-1}, which correspond to monoclinic WO_3.[21] In addition, a very slight shift (of ~7 cm^{-1}) to higher frequency is observed for the 317 cm^{-1} line. If these changes could again be attributed to a continuing crystallization of the material, with a likely monoclinic structure at 300 °C, the splitting of the 256 cm^{-1} absorption feature into vibrations at 250 and 268 cm^{-1}, and of the 324 cm^{-1} band into lines at 323 and 343 cm^{-1}, together with the appearances of new weak absorptions at 184, 211, and 369 cm^{-1}, suggest an additional material structural change at higher temperatures. This is only a tentative, but plausible assumption, since no detailed investigations in this region have been previously reported in the literature, which makes the assignment of these new lines difficult. The single reported WO_3 lattice dynamics analysis in the IR region is by Salje,[22] which is only for temperatures between –180 and 290 °C; and thus, much lower than the current ones.

Further analysis of these samples by Raman spectroscopy is presented in Fig. 2. The Raman spectrum of the pure silicon substrate is also shown in this figure, for easier comparison and for assignment of the features at 303, 435, 622, and 675 cm^{-1} to the presence of Si-O bonds. The spectrum of the RT WO_3 sample is very similar to the Si spectrum, showing only a slight increase in the intensities of the two broad bands around 675 and 810 cm^{-1}, therefore revealing an amorphous nature for this sample. The sharpening and increasing of intensities of these peaks, which become more evident at higher temperatures, demonstrate a trend toward ordering, that is, toward the presence of crystalline domains of increasing size. From the positions of the growing peaks we can infer the presence of a monoclinic WO_3 structure in our films for temperatures $\leq$300 °C.

With increasing temperature, weak shoulders around 271 and 711 cm^{-1} can be observed in the spectra. These features transform into definite Raman peaks at 400 and 500 °C. Since O-W-O bridging oxygen vibrations at

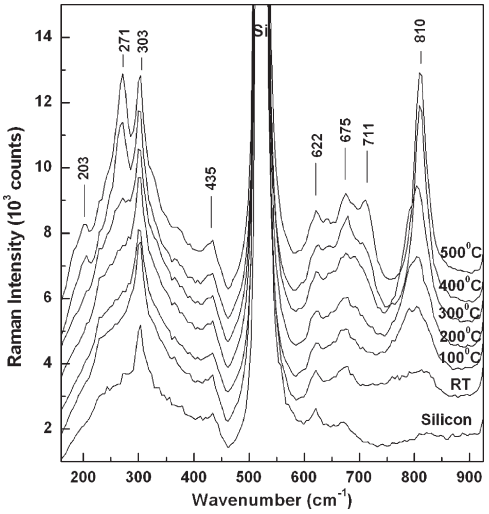

FIG. 2. Raman spectra of WO_3 samples for varying Si substrate growth temperature.

271 ± 2 cm^{-1} and 711 ± 5 cm^{-1} were previously reported in the literature for different WO_3 structures,[19–21,24] a definite assignment of WO_3 morphology cannot be based on them. A similar situation arises for the 810 cm^{-1} Raman peak. However, at these temperatures, the presence of a new weak peak around 203 cm^{-1} is observed. Although Pecquenard et al.[24] attributed this peak to the orthorhombic phase of WO_3, features around the same frequency have been found in the spectra of WO_3 under high pressure conditions.[19,20] Therefore, the exact nature of this Raman vibration in our spectra is controversial: it may be associated with a phase transition from monoclinic to orthorhombic WO_3, or with the existence of internal stress in the films, or with both. The possibility of a phase transition is in good agreement with previously reported literature results, which affirm that for bulk WO_3 a complete transformation to an orthorhombic morphology is expected for temperatures ranging between 330 and 740 °C, where a further transformation to tetragonal is expected to occur. On the other hand, since surface diffusion and film roughness increase at elevated growth temperatures, it is likely that the lattice mismatch between the Si substrate and the crystallized WO_3 layer become larger, and, as a result, an induced stress appears in the thin film.

Due to the laser filter cutoff, we could not perform Raman measurements at frequencies lower than 150 cm^{-1}, a region where a definite distinction between WO_3 structures would be achievable. However, to eliminate the strong Si substrate influence in our spectra and to elucidate the origin of the 303 cm^{-1} Raman vibration, which, apart from corresponding to Si, could also be attributed to an orthorhombic WO_3 characteristic mode,[24] we analyze the samples grown on a sapphire substrate. These Raman results are presented in Fig. 3. Not only do

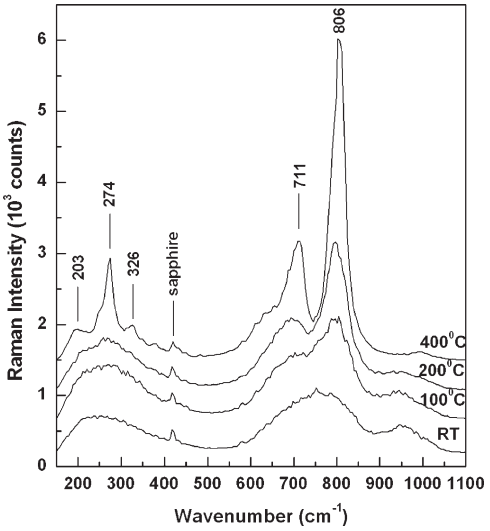

FIG. 3. Raman spectra of WO_3 samples for varying sapphire substrate growth temperature.

they corroborate with our previous observation of a continuing crystallization with increasing temperature, but they confirm the existence in our samples of a monoclinic structure even for a 400 °C substrate temperature. This affirmation is based on the existence of typical monoclinic vibrational modes at 274, 326, 711, and 806 cm^{-1} in the spectrum of the sample grown at 400 °C. In addition, the presence in this Raman spectrum of the same weak vibration around 203 cm^{-1} together with the absence of the characteristic orthorhombic 303 cm^{-1} Raman peak, demonstrate a strained WO_3 structure for samples grown at high temperatures.

In order to qualitatively identify in the samples the occurrence of this strained WO_3 structure versus the monoclinic WO_3 structure, we performed confocal Raman mapping on the surfaces of the samples grown at 400 and 500 °C. The images obtained from these measurements, at different magnifications (as indicated by the 1 μm and 400 nm scale bars), are presented in Figs. 4(a)–4(d). The light gray color corresponds to a strained WO_3 structure and the black color to a monoclinic structure. While the existence of the monoclinic phase is still observed in these images, the strained phase predominates, more notably for a growth temperature of 500 °C.

Since some properties of WO_3 are controlled by surface defects rather than by the intrinsic nature of this material, we performed XPS analysis on the samples, and the results are presented in Figs. 5 and 6. The XPS survey scans show that the main constituent elements of the films were tungsten and oxygen atoms, except for an additional C peak at 284.6 eV, which was used for calibration purposes and originates from surface adsorbed carbon moieties. There was no other discernable impurity except for carbon.

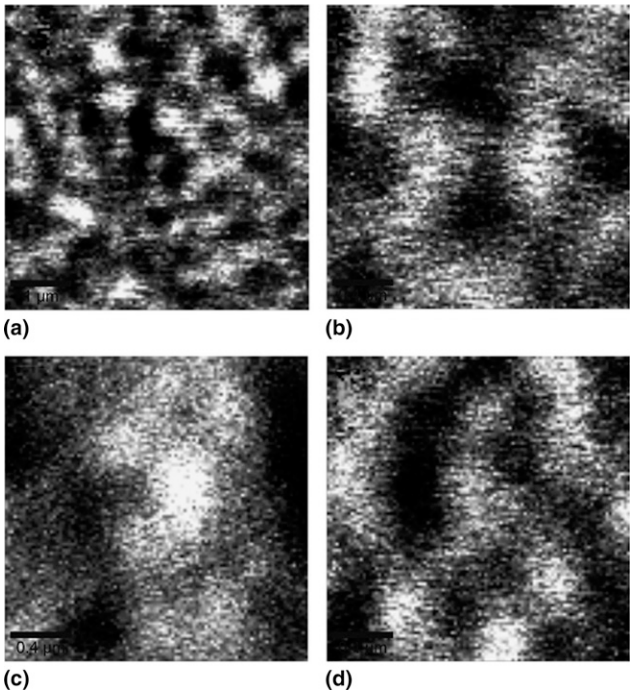

FIG. 4. (a)–(d) Confocal Raman mapping on the surfaces of WO_3 samples grown at: (a, b) 400 °C, and (c, d) 500 °C. The images were recorded at different resolutions and on different spots.

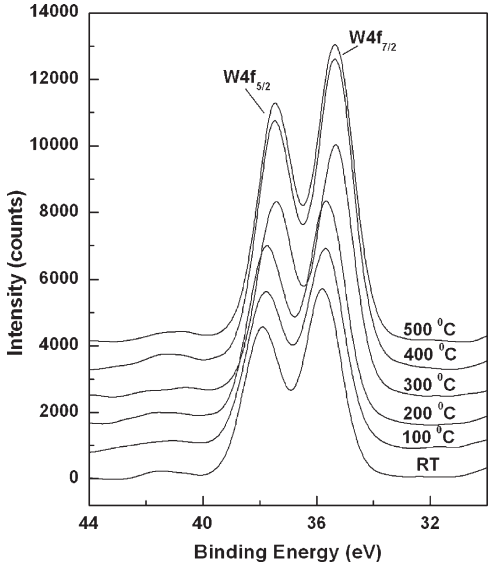

FIG. 5. XPS spectra of W 4*f* peaks for samples deposited on Si substrates at different temperatures, as indicated. The spectra are vertically translated for clarity.

Narrow-scan XPS measurements were performed for the W 4*f* and O 1*s* regions to identify the elements' chemical states. It is known from literature that a large energy shift, of about 3 eV, occurs for the binding energy of W $4f_{7/2}$ as W^{6+} is reduced to W^{4+} and only a 0.2 eV shift is expected for O 1*s*. It is also established that WO_3

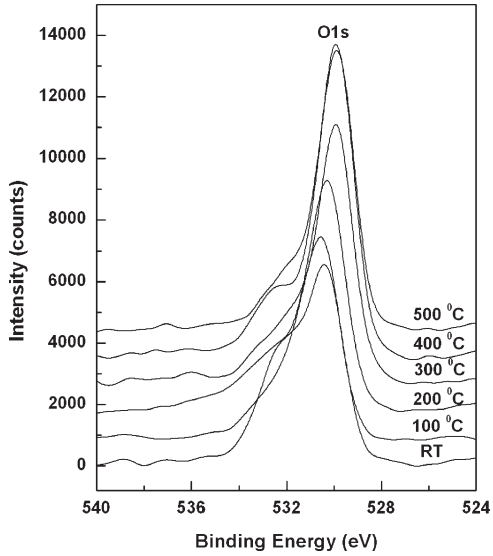

FIG. 6. XPS spectra of O 1*s* peaks for samples deposited on Si substrates at different temperatures, as indicated. The spectra are vertically translated for clarity.

has the tendency to form substoichiometric shear phases, which do not significantly affect the coordination polyhedron of oxygen about each W, since they originate from an alteration of the anion to cation ratio.[25,26]

The XPS measurements of the W 4*f* level, which are presented in Fig. 5, reveal well-resolved doublet peaks corresponding to W $4f_{5/2}$ and W $4f_{7/2}$. While at RT the binding energies of these peaks are 37.9 eV and 35.8 eV, respectively, indicating that the film surface is close to the chemical stoichiometry of WO_3,[25] with increasing temperature, a slight shift of about 0.5 eV toward lower energies is observed in their positions. We attribute this shift to a small partial change in the tungsten oxidation state from W^{6+} to W^{5+} as previously observed and reported in the literature.[26]

The XPS data for O 1*s*, which are presented in Fig. 6, show the existence of oxygen in a characteristic metal oxide form with a binding energy of 530.4 eV. In addition to this intense peak, there is a weak feature at 532.4 eV, which is attributed to surface oxygen contamination. The peak areas of O 1*s* and W 4*f* core levels (sensitivity factors: 0.63 for O 1*s* and 2.0 for W 4*f*)[27] were subsequently calculated, yielding at RT an overstoichiometric ratio of oxygen to tungsten atomic concentrations of 3.2 ± 0.1. A slight decrease of this ratio is observed with increasing temperature, which again could be an indication of a continuing crystallization process.

IV. CONCLUSIONS

The inherent complexity and the likely inhomogeneity of WO_3 thin film samples grown by RF sputtering at different temperatures (between RT and 500 °C) were studied in detail using IR absorption, Raman spectroscopy, and XPS. The results from both IR absorption and Raman techniques demonstrate an amorphous nature for the WO_3 sample grown at RT and an initial crystallization into a monoclinic WO_3 structure for samples grown at temperatures between 100 and 300 °C. In the Raman spectra for 400 and 500 °C, the existence of a strained WO_3 structure is observed together with the monoclinic structure. XPS data indicate that the film surface is close to the chemical stoichiometry of WO_3, with a slight modification arising from oxygen contamination.

The absence of the expected Raman spectrum associated with the orthorhombic phase for the samples grown on sapphire has led us to the conclusion that our higher temperature WO_3 depositions are affected by strain rather than having an orthorhombic structure. An explanation for the strained structure at these temperatures could be the presence of interstitial oxygen incorporated into the film/substrate interface in the growth process. The relative amount of oxygen at the interface is a result of the interaction between the first deposited layer of the film and the SiO_2 surface, an interaction that can create a large gradient in oxygen chemical potential. As a consequence, oxygen can be pulled out from the SiO_2 into the growing film. Since the reduction in the chemical potential gradient will depend on the oxygen pressure during deposition, the distribution of oxygen at the interface due to the SiO_2 reacting with the first layer of the film will depend on the overall oxygen content.

This work demonstrates the value of applying sensitive spectroscopy tools to investigate the morphology of WO_3. In particular, it shows the effectiveness of far-infrared absorption and Raman mapping spectroscopies for observing small structural modifications and for proving useful information that is complementary to that obtained though other means of optical and electron spectroscopy. It is clear that such combined techniques can play a crucial role in the ongoing quest to improve and optimize material properties.

ACKNOWLEDGMENTS

This work was supported by U.S. Department of Energy Grant No. DE-P26-08NT00198 and the National Science Foundation, MRI Grant No. 0723115.

REFERENCES

1. A.I. Gavrilyuk, B.P. Zakharchenya, and F.A. Chudnovskii: Photochromism in WO_3 thin films. *Electrochim. Acta* **44,** 3027 (1999).
2. S.K. Deb: Optical and photoelectric properties and color centers in thin films of WO_3. *Philos. Mag.* **17,** 801 (1973).
3. C.S. Blackman and I.P. Parkin: Atmospheric pressure chemical vapor deposition of crystalline monoclinic WO_3 and WO_{3-x} thin films from reaction of WCl_6 with O-containing solvents and their photochromic and electrochromic properties. *Chem. Mater.* **17,** 1583 (2005).

4. S.H. Lee, R. Deshpande, P.A. Parilla, K.M. Jones, B. To, A.H. Mahan, and A.C. Dillon: Crystalline WO_3 nanoparticles for highly improved electrochromic applications. *Adv. Mater.* **18,** 763 (2006).
5. S.H. Baeck, K.S. Choi, T.F. Jaramillo, G.D. Stucky, and E.W. McFarland: Enhancement of photocatalytic and electrochromic properties of electrochemically fabricated mesoporous WO_3 thin films. *Adv. Mater.* **15,** 1269 (2003).
6. W. Cheng, E. Baudrin, B. Dunn, and J.I. Zink: Synthesis and electrochromic properties of mesoporous tungsten oxide. *J. Mater. Chem.* **11,** 92 (2001).
7. L. Zhou, Q. Ren, X. Zhou, J. Tang, Z. Chen, and C. Yu: Comprehensive understanding on the formation of highly ordered mesoporous tungsten oxides by x-ray diffraction and Raman spectroscopy. *Microporous Mesoporous Mater.* **109,** 248 (2008).
8. S.M.A. Durrani, E.E. Khawaja, M.A. Salim, M.F. Al-Kuhaili, and A.M. Al-Shukri: Effect of preparation conditions on the optical and thermochromic properties of thin films of tungsten oxide. *Sol. Energy Mater. Sol. Cells* **71,** 313 (2002).
9. S.H. Lee, H.M. Cheong, P. Liu, D. Smith, C.E. Tracy, A. Mascarenhas, J.R. Pitts, and S.K. Deb: Raman spectroscopic studies of gasochromic a-WO_3 thin films. *Electrochim. Acta* **46,** 1995 (2001).
10. S.M. Kanan, O.M. El-Kadri, I.A. Abu-Yousef, and M.C. Kanan: Semiconducting metal oxide based sensors for selective gas pollutant detection. *Sensors* **9,** 8158 (2009).
11. D.E. Williams: Semiconducting oxides as gas-sensitive resistors. *Sens. Actuators, B* **57,** 1 (1999).
12. A. Kolmakov and M. Maskovits: Chemical sensing and catalysis by one-dimensional metal-oxide nanostructures. *Annu. Rev. Mater. Res.* **34,** 151 (2004).
13. W.H. Tao and C.H. Tsai: H_2S sensing properties of noble metal doped WO_3 thin film sensor fabricated by micromachining. *Sens. Actuators, B* **81,** 237 (2002).
14. M. Stankova, X. Vilanova, J. Calderer, E. Llobet, J. Brezmes, I. Gracia, C. Cane, and X. Correig: Sensitivity and selectivity improvement of RF sputtered WO_3 microhotplate gas sensors. *Sens. Actuators, B* **113,** 241 (2006).
15. C.V. Ramana, S. Utsunomiya, R.C. Ewing, C.M. Julien, and U. Becker: Structural stability and phase transitions in WO_3 thin films. *J. Phys. Chem. B* **110,** 10430 (2006).
16. E. Salje: The orthorhombic phase of WO_3. *Acta Crystallogr., Sect. B: Struct. Sci.* **33,** 574 (1977).
17. S. Tanisaki: Crystal structure of monoclinic tungsten trioxide at room temperature. *J. Phys. Soc. Jpn.* **15,** 573 (1960).
18. P.M. Woodward, A.W. Sleight, and T. Vogt: Ferroelectric tungsten trioxide. *J. Solid State Chem.* **131,** 9 (1997).
19. M. Boulova, N. Rosman, P. Bouvier, and G. Lucazeau: High-pressure Raman study of microcrystalline WO_3 tungsten oxide. *J. Phys. Condens. Matter* **14,** 5849 (2002).
20. A.G. Souza Filho, P.T.C. Freire, O. Pilla, A.P. Ayala, J. Mendes Filho, F.E.A. Melo, V.N. Freire, and V. Lemos: Pressure effects in Raman spectrum of WO_3 microcrystals. *Phys. Rev. B: Condens. Matter* **62,** 3699 (2000).
21. E. Salje: Lattice dynamics of WO_3. *Acta Crystallogr., Sect. A: Found. Crystallogr.* **31,** 360 (1975).
22. S.K. Gullapalli, F.S. Manciu, J.L. Enriquez, and C.V. Ramana: Tungsten oxide (WO_3) thin films for application in advanced energy systems. *J. Vac. Sci. Technol., A* **28,** 824 (2010).
23. K. Ohwada: Lattice vibrations of δ-uranium and tungsten trioxides. *Spectrochim. Acta, Part A* **26A,** 1035 (1969).
24. B. Pecquenard, H. Lecacheux, J. Livage, and C. Julien: Orthorhombic WO_3 formed via a T-stabilized WO_3 H_2O phase. *J. Solid State Chem.* **135,** 159 (1998).
25. H-T. Sun, C. Cantalini, L. Lozzi, M. Passacantando, S. Santucci, and M. Pelino: Microstructural effect on NO_2 sensitivity of WO_3 thin film gas sensors. Part 1. Thin film devices, sensors and actuators. *Thin Solid Films* **287,** 258 (1996).
26. Y.S. Kim: Thermal treatment effects on the material and gas-sensing properties of room-temperature tungsten oxide nanorod sensors. *Sens. Actuators, B* **137,** 297 (2009).
27. C.D. Wagner, W.M. Riggs, L.E. Davis, and J.E. Moueler: *Handbook of X-ray Photoelectron Spectroscopy*, edited by G.E. Muilenberg (Perkin-Elmer, Eden Prairie, MN, 1979).

Effect of Structure and Size on the Electrical Properties of Nanocrystalline WO_3 Films

R.S. Vemuri, K. Kamala Bharathi, S.K. Gullapalli, and C.V. Ramana*

Department of Mechanical Engineering, University of Texas at El Paso, El Paso, Texas 79968

ABSTRACT Nanocrystalline WO_3 films were grown by reactive magnetron sputter-deposition by varying the substrate temperature in the range of 303(RT)−673 K. The structure and electrical transport properties of WO_3 films were evaluated using X-ray diffraction and dc electrical conductivity measurements. The effect of ultramicrostructure and grain-size was significant on the electrical properties of WO_3 films. DC conductivity variation of the WO_3 films measured in the temperature range of 120−300 K reveals their semiconducting nature. The temperature dependent electrical conductivity curves exhibit two distinct regions indicative of two different types of electrical transport mechanisms. Analysis of the conductivity indicates that the small polaron and variable-range-hopping mechanisms are operative in 180−300 K and 120−180 K temperature regions, respectively. The density of localized states at the Fermi level, $N(E_F)$, has been calculated and it was found to be $\sim 1 \times 10^{19}$ eV^{-1} cm^{-3} for all the films.

KEYWORDS: WO_3 thin films • H_2S sensors • size effects • electrical properties • small polaron hopping • variable range hopping

I. INTRODUCTION

Semiconducting oxides received significant recent attention as sensor materials because of their remarkable electrical properties sensitive to oxidative or reductive type of gases (1–4). Currently, there has been a great deal of interest in WO_3 low-dimensional structures for a wide variety of applications in chemical and mechanical sensors, selective catalysis, electrochemical industry and environmental engineering (5–9). It has been demonstrated that the sensing properties of WO_3 films will have numerous applications in environmental and industrial pollution monitoring (5–9). WO_3 films exhibit excellent functional activity to various gases, such as H_2S, NO_x, trimethylamine, and other organics, and are suitable for integrated sensors (5–9). Most importantly, WO_3 nanocrystalline films have been established as one of the best gas sensors for the reducing gases such as NO_2, H_2, and CO and the results evidenced the role of the microstructure, specifically the grain size (5–9). Because of the large surface to volume ratio and smaller dimensions, WO_3 nanostructures appear to be promising candidates for chemical sensors working at various temperatures, which include low and high temperatures (10). In addition, WO_3 is an intensively studied representative of a group of "chromogenic" materials because of the coloration effects associated with various processes (11–14). WO_3 has been in use for the development of smart windows for energy-efficient architecture of buildings and automobiles, flat-panel displays, optical memory and writing-reading-erasing devices, and electronic information displays. Most of these applications depend on the remarkable electrical and optical properties of WO_3 (15). Therefore, the controlled growth, fundamental understanding, and manipulation of electronic properties of WO_3 at the nanoscale dimensions has important implications for the sensor design and utilizing WO_3 films.

The electrical properties, and hence the sensor performance of WO_3 films, is dependent on the microstructure, which in turn depends on the technique used to fabricate the films and the growth conditions. The microstructure factors such as grain size (L), grain boundary, film thickness, specific phase, dopants (if any), and active surface offered for reaction with the test gases will, therefore, play a significant role in determining the ultimate sensing performance of WO_3 nanostructures. However, WO_3 is a complicated material with respect to crystal structure and thermal stability because of several structures, such as monoclinic, triclinic, tetragonal, orthorhombic, cubic, and hexagonal, for pure and oxygen deficient WO_3 (16–18). At room temperature, WO_3 crystallizes in a triclinic structure and exhibit structural transformation at higher temperatures (16–19). Investigations on bulk WO_3 report the following sequence: triclinic (~17 °C) → monoclinic (330 °C) → orthorhombic (740 °C) → tetragonal. In addition to that, formation of pyrochlore WO_3 structure at about 373 K has been reported (20). Furthermore, WO_3 films prepared by various techniques (20–23) and under various processing conditions usually possess different microstructures and properties. Therefore, the control of microstructure and the fundamental understanding of the effect of microstructure on the electrical properties of WO_3 need a significant attention for both theoretical (24, 25) and experimental investigations. Clearly, controlled growth and manipulation of specific crystal structures at the nanoscale dimensions has important implications for the design and applications of WO_3-based sensors. The ability to tailor the properties so as to optimize sensor performance requires a detailed fundamental understanding of the relationship between the microstructure and

* Corresponding author. E-mail: rvchintalapalle@utep.edu.
Received for review May 21, 2010 and accepted August 1, 2010

DOI: 10.1021/am1004514

electrical properties of WO_3, particularly at the nanoscale dimensions.

In the present work, the microstructure and temperature-dependence of electrical conductivity of nanocrystalline WO_3 films made by radio frequency magnetron sputtering are investigated. WO_3 films were produced at various substrate temperatures ranging from room-temperature (RT/303 K) to 673 K. The purpose is not only to obtain films with a variable microstructure and nanometrics but also to cover the range of temperatures that are usually required either for postannealing or film processing of WO_3 for sensors as reported in the literature. To explain electrical transport properties, we have considered several conduction mechanisms as relevant to oxide semiconductors. These models include the simple thermally activated conduction, grain-boundary conduction, small-polaron hopping conduction, and variable-range hopping (VRH) conduction. An analysis of the conduction mechanisms at various temperature ranges and a correlation between microstructure and electrical properties in nanocrystalline (nc-WO_3) W−O films is presented and discussed in detail in this paper.

2. EXPERIMENTAL SECTION

WO_3 thin films were deposited onto silicon (Si) wafers by radio frequency (RF) (13.56 MHz) magnetron sputtering. The Si(100) substrates were cleaned by RCA (Radio Corporation of America) cleaning. All the substrates were thoroughly cleaned and dried with nitrogen before introducing them into the vacuum chamber, which was initially evacuated to a base pressure of $\sim 1 \times 10^{-6}$ Torr. Tungsten (W) metal target (Plasmaterials Inc.) of 3″ diameter and 99.95% purity was employed for reactive sputtering. The W-target was placed on a 3-in. sputter gun, which is placed at a distance of 8 cm from the substrate. A sputtering power of 40 W was initially applied to the target while introducing high purity argon (Ar) into the chamber to ignite the plasma. Once the plasma was ignited the power was increased to 100 W and oxygen (O_2) was released into the chamber for reactive deposition. The flow of the Ar and O_2 and their ratio was controlled using as MKS mass flow meters. Before each deposition, the W-target was presputtered for 10 min using Ar alone with shutter above the gun closed. The samples were deposited at different temperatures (T_s) varying from RT-673 K. The substrates were heated by halogen lamps and the desired temperature was controlled by Athena X25 controller.

The grown WO_3 films were characterized by performing structural and electrical measurements. X-ray diffraction (XRD) measurements on WO_3 films were by performed using a Bruker D8 Advance X-ray diffractometer. All the measurements were made ex-situ as a function of growth temperature. XRD patterns were recorded using Cu Kα radiation ($\lambda = 1.54056$ Å) at RT. The coherently diffracting domain size (d_{hkl}) was calculated from the integral width of the diffraction lines using the well-known Scherrer's equation (26) after background subtraction and correction for instrumental broadening. Surface imaging analysis was performed using a high-performance and ultra high resolution scanning electron microscope (Hitachi S-4800). The secondary electron imaging was performed on WO_3 films grown on Si wafers using carbon paste at the ends to avoid charging problems. The grain detection, size-analysis and statistical analysis was performed using the software provided with the SEM. The average grain size measured was found to vary from 9 to 50 nm as reported elsewhere (27). DC electrical resistivity measurements were carried out under the vacuum of 10^{-2} Torr by two-probe method in the temperature range 120−300 K employing a closed cycle refrigerator (CCR). Resistance was measured by employing a Keithley electrometer (Keithley 6517A Electrometer/High resistance meter). The temperature was measured using a silicon diode sensor and employing a Lakeshore temperature controller (model 330). The film was kept on the cold head of the CCR. The point contacts were made by soldering the indium metal at the corners of the films.

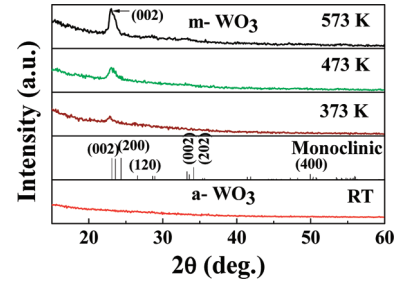

FIGURE 1. XRD patterns of WO_3 films grown at $T_s \leq 573$ K. It is evident from the curves that the films grown at RT are amorphous whereas films grown at $T_s \geq 373$ K are nanocrystalline. Films crystallize in m-WO_3 phase. XRD pattern of m-WO_3 (PDF: 830950) is also included for reference. WO_3 films grown at 573 exhibit a mixture of monoclinic and tetragonal phases.

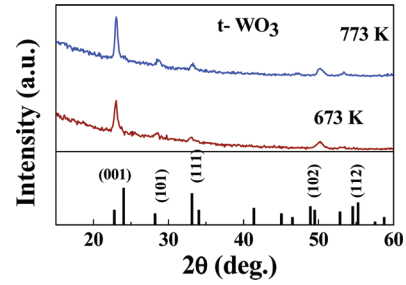

FIGURE 2. XRD patterns of WO_3 films grown at $T_s \geq 673$ K. The curves indicate that WO_3 films crystallize in tetragonal structure. XRD pattern of t-WO_3 (PDF:also included for comparison.

3. RESULTS AND DISCUSSION

The XRD patterns of WO_3 films are shown in Figures 1 and 2 as a function of T_s. The XRD curve (Figure 1) of WO_3 films grown at RT did not show any peaks indicating their amorphous (a-WO_3) nature. The XRD peak corresponding to monoclinic WO_3 (m-WO_3) phase appears when the $T_s =$ 373 K. However, the peak (at 23.1°) is rather broad, indicating the presence of very small nanoparticles. It is evident (Figure 1) that the intensity of the peak, at 23.1°, which corresponds to diffraction from (002) planes increase with increasing T_s (28). This is an indicative of an increase in the average crystallite-size and preferred orientation of the film along (002) with increasing T_s. The later is dominant for WO_3 films grown at $T_s \geq 473$ K. Also, a structural transformation occurs at $T_s = 673$K. XRD peaks due to tetragonal (t-WO_3) phase are clearly seen for WO_3 films grown at $T_s \geq 673$ K (Figure 2). In fact, it can be seen in the XRD curve obtained for WO_3 films grown at 573 K that an overlap of (001) peak corresponding to t-WO_3 and (002) peak corresponding to m-WO_3 indicating the onset of phase transformation but not complete. Perhaps, the temperature is just sufficient to induce a phase change in nanoscale m-WO_3 films but not fully favorable to complete the process. High-temperature

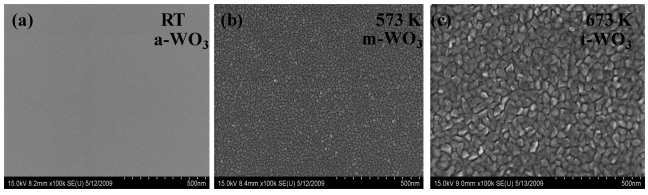

FIGURE 3. SEM images of WO_3 films grown at various temperatures. The phases determined from XRD are as indicated.

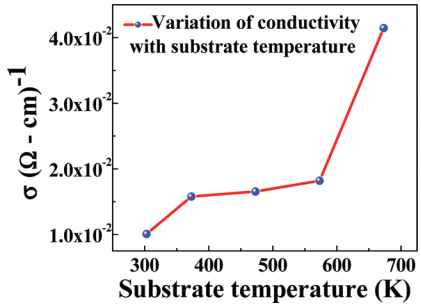

FIGURE 4. Room-temperature conductivity value for WO_3 films grown at different substrate temperatures.

t-WO_3 formation at 673 K seems to be the effect of phase stabilization at the nanoscale dimensions. The preferred *c*-axis orientation could be due to the growth process minimizing the internal strain-energy in the film. Anisotropy exists in crystalline materials and the strain energy densities will typically be different for different crystallographic direction. The growth will favor those orientations with low strain energy density. Therefore, increasing T_s favors the preferred orientation along (002) while minimizing the strain-energy in the WO_3 film. The SEM images of WO_3 films as a function of substrate temperature are shown in Figure 3. The effect of temperature on the surface morphology of WO_3 films is remarkable. No features can be seen for WO_3 films grown at RT even at very high magnifications (Figure 3a). This observation is in agreement with the XRD results indicating the complete amorphous nature of the samples. The small, dense particles spherical in shape can be noticed in SEM image (Figure 3b) for WO_3 films grown at 473 K. The SEM data along with appearance of diffraction peaks in XRD clearly indicate that 473 K is the critical temperature to promote the growth of nanocrystalline WO_3 films. The XRD and SEM results suggest that a further increase in temperature beyond 473 K results in changes in the crystal structure and morphology. WO_3 films continue to show preferred growth along with an increase in average particle size with increasing temperature. It can be seen in SEM image (Figure 3c) that increasing temperature to 573 K results in size >20 nm.

The room-temperature electrical conductivity variation of WO_3 films with T_s is shown in Figure 4. It can be seen that the electrical conductivity increases with increasing T_s. The conductivity is reported to decrease with grain size reduction due to the increasing grain boundary volume and associated impedance to the flow of charge carriers (29, 30). If the crystallite size is smaller than the electron mean free path, grain boundary scattering dominates and hence the electrical conductivity decreases. The electrical resistivity is also

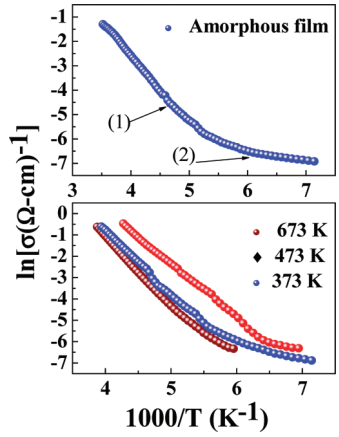

FIGURE 5. Temperature-dependent dc conductivity of WO_3 films.

very sensitive to lattice imperfections in solids, such as vacancies and dislocations that are reported to be present in nanocrystalline materials. In addition to that, lattice strain and the distortions can affect the motion of charge causing decrease in conductivity (29–31). The room-temperature conductivity data and its variation with T_s observed for WO_3 can be explained taking these factors into consideration. WO_3 films grown at RT are completely amorphous as evidenced in XRD studies. The randomness or disordered structure of the films, therefore, accounts for the observed low conductivity of a-WO_3 films. Appearance of diffraction peaks in the XRD curves, an increase in the average crystallite size along with a preferred orientation of the film along (002) is clearly seen with increasing T_s. Therefore, increase in conductivity with increasing T_s can be attributed to the increasing crystalline nature and preferred orientation of the film along (002). In addition, a decrease in strain energy of the growing WO_3 film, as discussed using the XRD results, with increasing T_s also causes the increase in conductivity. The observed jump in the electrical conductivity for WO_3 films grown at 673 K seems to be a result of combined effect of the grain-size increase and phase transformation from m-WO_3 to t-WO_3. The observed variation in electrical conductivity is in correlation with optical properties, where we found enhancement in the band gap for a-WO_3 films and continuous decrease in the band gap with increasing temperature or grain size (32).

The temperature-dependent electrical conductivity plots of WO_3 films are shown in Figure 5. Conductivity decreases exponentially with decreasing temperature from 300 to 120 K which indicates the semiconducting nature of all the WO_3 films. However, a marked difference in the temperature-dependence of conductivity can be seen for a-WO_3 films (Figure 5a) when compared to nc-WO_3 films (Figure 5b). Similarly, in Figure 4b, it can be seen that the curves of WO_3 films grown at 373 and 473 K are clearly separated from WO_3 films grown at 673 K. We attribute this behavior to the grain-size and phase transformation. The size variation for the films grown between 373 and 473 K is small but significantly lower when compared films grown at 673 K (24, 32). Also, phase transformation occurs from m-WO_3 to t-WO_3 at 673 K. The most remarkable feature of these

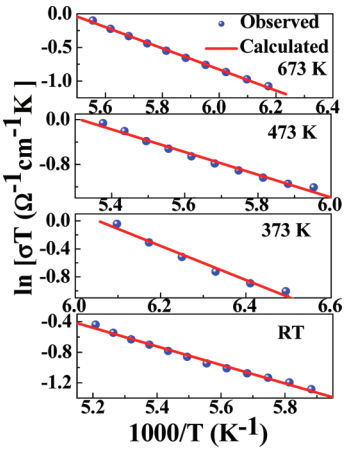

FIGURE 6. Relation between ln σT and 1000/T for WO_3 thin films.

temperature-dependent electrical conductivity curves of WO_3 films is two distinct regions indicative of two different conduction mechanisms operative in those temperature regions.

The temperature-dependence of conductivity of a-WO_3 film (Figure 5a) shows almost a linear behavior at high temperatures ($T > 250$ K) and a curvature at low temperatures. It can also be noticed that the activation energy continuously decreases with a decrease in measuring temperature of the conductivity. The curvature without a definite slope and continuous decrease in activation energy is a characteristic behavior of polaron hopping mechanism in amorphous semiconductors. On the other hand, the conductivity plots show a distinct change in slope at a more or less same temperature in nc-WO_3 films (Figure 4b). We consider various models to analyze the observed electrical properties and conduction mechanisms as discussed below.

Conductivity in semiconductors is due to both hopping of electrons and charge transport via excited states and it can be expressed as (33, 34)

$$\sigma = A_1\exp\left(\frac{-E_1}{k_BT}\right) + A_2\exp\left(\frac{-E_2}{k_BT}\right) + A_3\exp\left(\frac{-E_3}{k_BT}\right)+ \quad (1)$$

where E_1 is the activation energy for intrinsic conduction and E_2, E_3, ..., are the activation energies needed for hopping conduction. A_1, A_2, A_3 are constants and k_B is the Boltzmann constant. Ln σ vs 1000/T plots (Figure 6) yield two different slopes for WO_3 films. The activation energy values at different temperature ranges (300−180 K and 180−120 K) calculated from the ln σ vs 1000/T plots are given in Table 1. The activation energy is found to be higher in the 300−180 K temperature region when compared that in the 180−120 K temperature region. Decreasing activation energy with decreasing temperature in transition metal oxides has been explained by small-polaron theory (34). The VRH model of small polarons also predicts continuously decreasing activation energy with decreasing temperature. Small polaron formation occurs for strong enough electron−phonon interaction, as predicted by Landau (35). The polaron transport occurs by hopping process at sufficiently higher temperatures. The multiphonon hopping process freezes out at lower temperatures, and conduction through extended states in a polaron band dominates. This should lead to a decay of the conductivity and activation energy as the temperature is reduced well below half of the Debye temperature (36).

To obtain a clear distinction between the two conduction mechanisms (two different slopes in Figure 5), we used the polaron and variable-range hopping (VRH) models to fit the conductivity data of WO_3 films. In the temperature regime, 180−300 K, the conductivity data of WO_3 films can be interpreted in terms of the phonon-assisted hopping model given by Mott (37)

$$\sigma = \frac{e^2\nu_{ph}c(1-c)}{k_BTR}\exp(-2\alpha R)\exp\left(-\frac{E}{kT}\right) \quad (2)$$

where ν_{ph} is the optical phonon frequency, c is the fraction of reduced transition metal ions (the ratio of ion concentration of transition metal ions in the low valence state to the total concentration of transition metal ions), R is the average spacing between the transition ions, α is the localization length, and E is the activation energy for the hopping conduction. The plots of ln σT vs 1000/T for WO_3 films are shown in Figure 6. The values of ν_{ph} and R, the activation energy, E (calculated from the slope of the plot) are given in Table 1. Assuming a strong electron−phonon interaction, Austin and Mott proposed that

$$E = E_H + \frac{E_D}{2} \quad (3)$$

for ($T > \theta_D/2$)

$$E = E_D \quad (4)$$

for ($T > \theta_D/4$) where E_H is the polaron hopping energy, E_D is the disorder energy arising from the energy difference of neighbors between two hopping sites and θ_D is the Debye temperature (380 K for WO_3). Polaron radius can be calculated using the formula (35–37)

$$r_p = \left(\frac{\pi}{6}\right)^{1/3}\left(\frac{R}{2}\right) \quad (3a)$$

Where R is the average distance between the transition metal ions (W ion), which is 0.3 nm in the present case (38). The value of r_p was found to be 0.12 nm.

To better understand the nature of hopping conduction, i.e., to determine whether it is adiabatic or nonadiabatic regime, it is necessary to perform a detailed analysis. The following are the conditions that define the adiabatic and nonadiabatic conduction

Table 1. Activation Energy Values, *A* and *B* Parameter Values, and the Density of Localized States at the Fermi Level Values of WO_3 Thin Films

substrate temperature of WO_3 film (°C)	activation energy (eV) 180−300 K	activation energy (eV) 120−180 K	A (Ω^{-1} cm^{-1} K$^{1/2}$)	B (K$^{1/4}$)	$N(E_F)$ (× 10^{19} eV^{-1} cm^{-3})
RT	0.22	0.029	73242	23.27	2.72
100	0.23	0.031	73602	23.89	2.71
200	0.25	0.033	72266	23.83	2.67
400	0.26	0.033	72572	23.48	2.65

$$J > \left(\frac{2kTE_H}{\pi}\right)^{1/4}\left(\frac{h\nu_0}{\pi}\right)^{1/2} \quad \text{(adiabatic)} \qquad (4a)$$

$$J < \left(\frac{2kTE_H}{\pi}\right)^{1/4}\left(\frac{h\nu_0}{\pi}\right)^{1/2} \quad \text{(nonadiabatic)} \qquad (5)$$

where J is the polaron bandwidth, E_H is the hopping energy (0.22 eV), and $h\nu_0 = k_B\theta_D$ (θ_D is the Debye temperature and it is 380 K for WO_3). In the evaluation of the term on the right-hand side of eq 5 at 300 K, a value of 0.0222 eV is obtained. On the other hand, J can be estimated independently using Dhawan's formula (36)

$$J \approx e^3\left(\frac{N(E_F)}{(\varepsilon_p)^3}\right)^{1/2} \qquad (6)$$

Where ε_p is the effective dielectric constant and it can be calculated using the Mott's small polaron hopping model with the relation by

$$E_H = \left(\frac{e^2}{4\varepsilon_p}\right)\left(\frac{1}{r_p} - \frac{1}{R}\right) \qquad (7)$$

In the present case, the value of ε_p was found to be 7.4. By using the previously obtained $N(E_F)$ and ε_p values, J is calculated as 0.0028 eV. Because $J < 0.0222$ eV, we conclude that the electrical transport in WO_3 is due to small-polaron conduction in the nonadiabatic regime.

According to the small-polaron theory and the VHR model of small polarons, the activation energy should continuously decrease with decreasing temperature. The procedure suggested by Greaves as a modification of Mott's model of VRH could be applied in the second temperature regime (120−180 K), and the following expression is proposed for the electrical conductivity

$$\sigma T^{1/2} = A\exp(-BT^{-1/4}) \qquad (8)$$

Where A and B are constants and B is expressed as

$$B = 2.1\left[\frac{\alpha^3}{k_B N(E_F)}\right]^{1/4} \qquad (9)$$

$N(E_F)$ is the density of localized states at E_F and α^{-1} is the decay constant of the wave function of localized states at E_F.

Variable-range hopping model may be valid in the temperature range 120−180 K and a good fit of the experimental data to the eq 9 is shown in Figure 7 ($\ln(\sigma T^{1/2})$ vs $T^{-1/4}$ plot). The values of parameters A and B were calculated from this curve and are shown in Table 1. The density of localized states at the Fermi level, $N(E_F)$, has been calculated taking a constant value of α^{-1} (× 10^{-7} cm) (38). The determined value is $N(E_F) \approx 1 \times 10^{19}$ eV^{-1} cm^{-3}, which is good agreement with the reported value for WO_3 films (39, 40). Electrical properties of WO_3 thin films prepared by thermal evaporation have been reported by M G Hutchins et al. (40). Arrhenius law, a polaron model, and a variable-range hopping model have been used to explain the conduction mechanism forWO_3 films at different temperature regime. Using the variable-range hopping model, the density of localized states at the Fermi level, $N(E_F)$, was reported to be to be 1.08×10^{19} eV^{-1} cm^{-3}. The average values of activation energies were found to be 1.70 eV ($T > 525$ K), 0.58 eV (525 K $\leq T \leq$ 353 K,) and 0.06 eV ($T \leq 353$ K).

A good fit of the Mott's VRH model has been verified by calculating the hopping parameters and the Mott's requirements (24) ($R_{hop}\alpha \geq 1$ and $E_{hop} > k_BT$). Here, R_{hop} and E_{hop} are temperature-dependent hopping distance and average polaron hopping energy, respectively.

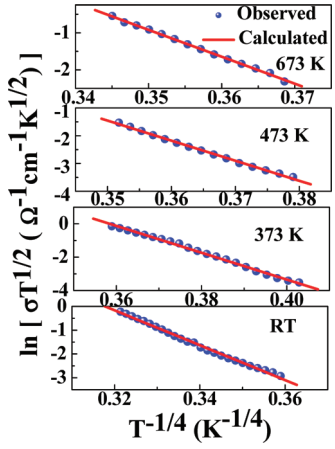

FIGURE 7. Relation between ($\ln(\sigma T^{1/2})$ and $T^{-1/4}$ for WO_3 thin films.

$$R_{hop} = \left[\frac{9}{8\pi N(E_F)\alpha k_B T}\right]^{1/4} \quad (10)$$

$$E_{hop} = \frac{3}{4\pi R_{hop}^3 N(E_F)} \quad (11)$$

The calculated average values of R_{hop} and E_{hop} at 140 K for WO_3 films are found to be 3.9 nm and 204 meV. The values of $R_{hop}\alpha$ and E_{hop} are found to be 3.9 and 204 meV, respectively. The requirements ($R_{hop}\alpha \geq 1$ and $E_{hop} > k_B T$) are clearly satisfied.

The effect of microstructure and size on the electrical properties of WO_3 films as determined in this work is quite useful while considering the fundamental aspects and design of a sensor. The key dimension defining the enhancement of a sensor performance as function of reducing particle size or film thickness is the Debye length (λ_D) (41, 42). Most important to mention is that the grain size must be very small on the order of λ_D, where the space-charge regions overlap and all the grains are fully depleted, to take the advantage of nanoscale effects. It has been reported that the better sensor performance was obtained for nanocrystalline SnO_2 films with very small sizes ($\leq\lambda_D$) or smallest thicknesses (41–44). In this context, although WO_3 films grown in the range of 373−573 K are promising, the electrical parameters determined for WO_3 films with grain sizes varying in the range of 9−50 nm could provide a database to design a sensor with enhanced performance.

4. SUMMARY AND CONCLUSION

Temperature-dependent dc electrical conductivity of the amorphous and nanocrystalline WO_3 films exhibits the exponential behavior which indicates the semiconducting nature of all the films. Lower conductivity of WO_3 films RT is attributed to their amorphous nature. The conductivity value was found to increase with increasing substrate temperature because of the increasing crystalline nature and preferred orientation of the nanocrystalline WO_3 films along (00 L). The mechanisms of electrical conduction at different temperature regions in all the films are explained in terms of a polaron model and a variable-range hopping model. The conductivity data of WO_3 films were successfully analyzed by the nonadiabatic small polaron hopping conduction theory at higher temperature (180−300 K). It has been found that the conduction mechanism at the temperature range of 120−180 K is due to variable range hopping mechanism. The density of localized states at the Fermi level, $N(E_F)$, has been calculated and it was found to be $\sim 1 \times 10^{19}$ eV^{-1} cm^{-3} for all the films.

Acknowledgment. This material is based on work supported by the Department of Energy under Award DE-PS26-08NT00198-00.

REFERENCES AND NOTES

(1) Meixner, H.; Lampe, U. *Sens. Actuators B* **1996**, *33*, 198–202.
(2) Williams, D. E. *Sens. Actuators B* **1999**, *57*, 1–16.
(3) Wang, X.; Miura, N.; Yamazoe, N. *Sens. Actuators B* **2000**, *66*, 74–79.
(4) Lee, D. S.; Han, S. D.; Lee, D. D. *Sens. Actuators B* **1999**, *60*, 57–63.
(5) Baeck, S. H.; Jaramillo, T.; Stucky, G. D.; McFarland, E. W. *Nano Lett.* **2002**, *2*, 831–834.
(6) Lee, D. S.; Nam, K. H.; Lee, D. D. *Thin Solid Films* **2000**, *375*, 142–147.
(7) Wang, L.; Teleki, S. E.; Pratsinis, S. E.; Gouma, P. I. *Chem. Mater.* **2008**, *20*, 4794–4796.
(8) Kawasaki, H.; Namba, J.; Iwatsuji, K.; Suda, Y.; Wada, K.; Ebihara, K.; Ohshima, T. *Appl. Surf. Sci.* **2002**, *8065*, 1–5.
(9) Ionescu, R.; Llobet, E.; Brezmes, J.; Vilanova, X.; Correig, X. *Sens. Actuators B* **2003**, *95*, 177–182.
(10) Gillet, M.; Delamare, R.; Gillet, E. *Eur. Phys. J. D* **2007**, *43*, 295–298.
(11) Gao, B.; Ma, Y.; Cao, Y.; Yang, W.; Yao, J. *J. Phys. Chem. B* **2006**, *110*, 14391–14397.
(12) Santato, C.; Ulmann, M.; Augustynski, J. *J. Phys. Chem. B* **2001**, *105*, 936.
(13) Deb, S. K. *Sol. Energy Mater. Sol. Cells* **2008**, *92*, 245–250.
(14) Huda, M. N.; Yan, Y.; Moon, C.-H.; Wei, S.-H.; Al-Jassim, M. M. *Phys. Rev. B* **2008**, *77*, 195102–195105.
(15) Shaltout, I. I.; Tang, Y. I.; Braunstein, R.; Shaisha, E. E. *J. Phys. Chem. Solid* **1996**, *57*, 1223–1224.
(16) Sahle, W.; Nygren, M. *J. Solid State Chem.* **1983**, *48*, 154–160.
(17) Berak, J. M.; Sienko, M. J. *J. Solid State Chem.* **1970**, *2*, 109–133.
(18) Salje, E.; Viswanathan, K. *Acta Crystallogr., Sect. A* **1975**, *31*, 356–359.
(19) Lassner, E.; Wolf-Dieter, S. *Tungsten: Properties, Chemistry, Technology of the Element, Alloys, and Chemical Compounds*; Kluwer Academic: New York, 1999.
(20) Ayyappan, S.; Rangavittal, N. *Bull. Mater. Sci.* **1997**, *20*, 103–109.
(21) Georg, A.; Graf, W.; Wittwer, J. *Sol. Energy Mater. Sol. Cells* **1998**, *51*, 353–370.
(22) Wang, X. G.; Jiang, Y. S.; Yang, N. H.; Yuan, L.; Pang, S. J. *Appl. Surf. Sci.* **1999**, *143*, 135–141.
(23) Akl, A. A.; Kamal, H.; Abdel-Hady, K. *Physica B* **2003**, *325*, 65–75.
(24) De Wijs, G. A.; de Boer, P. K.; de Groot, R. A.; Kresse, G. *Phys. Rev. B* **1999**, *59*, 2684–2693.
(25) Methfessel, M.; Paxton, A. T. *Phys. Rev. B* **1989**, *40*, 3616–3621.
(26) The Scherrer equation is $d_{hkl} = 0.9\lambda/\beta\cos\theta$, where d is the size, λ is the wavelength of the filament used in the XRD machine, β is the width of a peak at half of its intensity, and θ is the angle of the peak.
(27) Gullapalli, S. K.; Vemuri, R. S.; Ramana, C. V. *Appl. Phys. Lett.* **2010**, *96*, 171903–171905.
(28) Stankov, N. E.; Atanasov, P. A.; Stanimirova, T. J.; Dikovska, A. Og.; Eason, R. W. *Appl. Surf. Sci.* **2005**, *247*, 401–405.
(29) Bakonyi, I.; Toth-Kadar, E.; Tarnoczi, T.; Varga, L.; Cziraki, A.; Gerocs, I.; Fogarassy, B. *Nanostruct. Mater.* **1993**, *3*, 155–158.
(30) Wu, L.; Tien-Shou, W.; Chung-Chuang, W. *J. Phys. D: Appl. Phys.* **1980**, *13*, 259–266.
(31) Ramana, C. V.; Smith, R. J.; Julien, C. M. *J. Vac. Sci. Technol., A* **2004**, *22*, 2453–2458.
(32) Ramana, C. V.; Julien, C. M. *Chem. Phys. Lett.* **2006**, *428*, 114–118.
(33) Ambily, S.; Menon, C. S. *Thin Solid Film* **1999**, *347*, 284–289.
(34) Mott, N. F.; Davis, E. A. *Electronic Processes in Non-Crystalline Materials*, 2nd ed.; Clarendon: Oxford, U.K., 1979.
(35) Landau, D. *Phys. Z. Sowjetunion* **1933**, *3*, 644–654.
(36) Ajai Gupta, K.; Kumar, V.; Khare, N. *Solid State Sci.* **2007**, *9*, 817–823.
(37) Mott, N. F. *J. Non-Cryst. Solid* **1968**, *1*, 1–10.
(38) Yildiz, A.; Lisesivdin, S. B.; Kasap, M.; Mardare, D. *Physica B* **2009**, *404*, 1423–1426.
(39) Hutchins, M. G.; Abu-Alkhair, O.; El-Nahass, M. M.; Abdel Hady, K. *J. Phys.: Condens. Matter* **2006**, *18*, 9987–9997.
(40) Ogawa, H.; Nishikawa, M.; Abe, A. *J. Appl. Phys.* **1982**, *53*, 44484455.
(41) Du, X.; George, S. M. *Sens. Actuators B* **2008**, *135*, 152–160.
(42) Jin, Z. H.; Zhou, H. J.; Jin, Z. L.; Savinell, R. F.; Liu, C. C. *Sens. Actuators B* **1998**, *52*, 188–194.
(43) Shieh, J.; Feng, H. M.; Hon, M. H.; Juang, H. Y. *Sens. Actuators B* **2002**, *86*, 75–80.
(44) Xu, C.; Tamaki, J.; Miura, N.; Yamazoe, N. *Sens. Actuators B* **1991**, *3*, 147–155.

AM1004514

Structural transformation induced changes in the optical properties of nanocrystalline tungsten oxide thin films

S. K. Gullapalli, R. S. Vemuri, and C. V. Ramana

Citation: Applied Physics Letters **96**, 171903 (2010); doi: 10.1063/1.3421540
View online: http://dx.doi.org/10.1063/1.3421540
View Table of Contents: http://scitation.aip.org/content/aip/journal/apl/96/17?ver=pdfcov
Published by the AIP Publishing

Structural transformation induced changes in the optical properties of nanocrystalline tungsten oxide thin films

S. K. Gullapalli, R. S. Vemuri, and C. V. Ramana[a)]
Department of Mechanical Engineering, University of Texas at El Paso, El Paso, Texas 79968, USA

(Received 21 January 2010; accepted 12 April 2010; published online 30 April 2010)

Nanocrystalline tungsten oxide (WO_3) films were grown by reactive magnetron sputter-deposition. The structure and optical properties of WO_3 films were evaluated using grazing incidence x-ray diffraction and optical spectroscopic measurements. The effect of ultramicrostructure was significant on the optical characteristics of WO_3 films. The band gap decreases from 3.25 to 2.92 eV with increasing grain-size from ~9 to 50 nm while the films exhibit a transition from monoclinic to tetragonal phase. A direct microstructure-property relationship found suggests that tuning properties of WO_3 films for desired applications can be achieved by tuning the conditions and controlling the phase. © *2010 American Institute of Physics*. [doi:10.1063/1.3421540]

Tungsten oxide (WO_3) is an intensively studied representative of a group of "chromogenic" materials because of the coloration effects associated with various processes.[1–6] There has been a great deal of recent interest in low-dimensional structures of WO_3 for a wide variety of applications in optoelectronics, microelectronics, selective catalysis, and environmental engineering.[2–12] WO_3 has been in use for the development of smart windows for energy-efficient architecture of buildings and automobiles, flat-panel displays, optical memory and writing−reading−erasing devices, and electronic information displays.[1–6] It has been demonstrated that WO_3 films exhibit chemical sensing properties,[6–12] which will have numerous applications in environmental and industrial pollution monitoring. WO_3 films exhibit excellent functional activity in various gases, such as H_2S, NO_x, trimethylamine, and other organics, and are suitable for integrated sensors.[6–12]

WO_3 is a complicated material with respect to crystal structure and thermal stability because of several structures, such as monoclinic, triclinic, tetragonal, orthorhombic, cubic, and hexagonal for pure and oxygen deficient WO_3.[1–3,13–15] At room-temperature, WO_3 crystallizes in a triclinic structure and exhibit structural transformation at higher temperatures. Investigations on bulk WO_3 report the following sequence: triclinic ($\sim 30\ ^\circ C$) → monoclinic ($330\ ^\circ C$) → orthorhombic ($740\ ^\circ C$) → tetragonal.[13,14] However, WO_3 thin films prepared by various techniques and under various processing conditions usually possess different microstructures and properties.

The controlled growth and manipulation of specific crystal structures at the nanoscale dimensions has important implications for the design and applications of WO_3 films. However, the ability to tailor the properties so as to optimize performance requires a detailed understanding of the relationship between electronic and geometric structure, particularly at the nanoscale dimensions. Furthermore, stabilizing metastable high-temperature phases in a controlled way requires detailed understanding of the structural transformation induced changes in the electronic properties of nanocrystalline WO_3 films. Therefore, it is important to characterize and obtain a correlation between microstructure and electronic properties in nanocrystalline WO_3 films as a function of growth conditions. The present work was, therefore, performed on sputter-deposited nanocrystalline WO_3 films under varying growth conditions to understand the size-effects on the optical properties. Interestingly, a size-phase-property correlation was found in nanocrystalline WO_3 films. The results and their implications for technology are presented and discussed in this letter.

WO_3 films were deposited onto optical grade quartz and silicon (Si) wafers by radio-frequency (rf) magnetron sputtering. The substrates were cleaned by RCA cleaning. All the substrates were thoroughly cleaned and dried with nitrogen before introducing them into the vacuum chamber, which was initially evacuated to a base pressure of $\sim 10^{-6}$ Torr. Tungsten (W) metal target of 3″ diameter and 99.95% purity was employed for reactive sputtering. The W target was placed on a 3 in. sputter gun, which is placed at a distance of 8 cm from the substrate. A sputtering power of 40 W was initially applied to the target while introducing high purity argon (Ar) into the chamber to ignite the plasma. Once the plasma was ignited the power was increased to 100 W and oxygen (O_2) was released into the chamber for reactive deposition. The flow of the Ar and O_2 and their ratio was controlled using as mks mass flow meters. Before each deposition, the W target was presputtered for 10 min using Ar alone with shutter above the gun closed. The deposition was carried out to obtain ~70 nm thick films. The samples were grown at various substrate temperatures (T_s) varying from RT to 500 °C. The substrates were heated by halogen lamps and the desired temperature was controlled by Athena X25 controller. Structural measurements were performed using a Bruker D8 Advance x-ray diffractometer employing Cu K_α radiation ($\lambda = 1.54056$ Å). The optical properties of WO_3 films were evaluated using spectrophotometric optical transmission and reflectance measurements using Cary 5000 UV-vis-NIR double-beam spectrophotometer.

The x-ray diffraction (XRD) patterns of WO_3 films are shown in Fig. 1 as a function of T_s. The XRD curve of WO_3 films grown at RT did not show any peaks indicating their amorphous (a-WO_3) nature. The XRD peak corresponding to monoclinic WO_3 (m-WO_3) phase appears when the

a)Author to whom correspondence should be addressed. Electronic mail: rvchintalapalle@utep.edu.

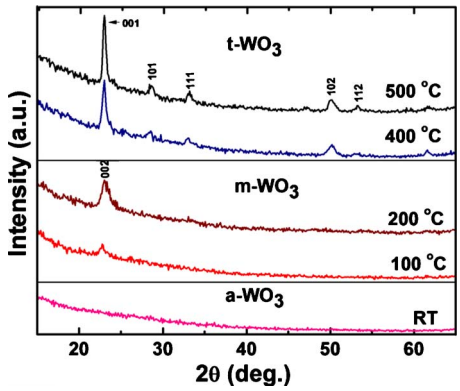

FIG. 1. (Color online) (a) XRD patterns of WO_3 films grown at various temperatures. Structural evolution and phase transitions as a function of T_s are as noted. WO_3 films grown at T_s=RT are amorphous (a-WO_3). WO_3 films exhibit a phase transition to monoclinic (m-WO_3) at T_s=100 °C and to tetragonal at higher temperatures.

T_s=100 °C. However, the peak (at 23.1°) is rather broad indicating the presence of very small particles. It is evident (Fig. 1) that the intensity of the peak, at 23.1°, which corresponds to diffraction from (00l) planes increase with increasing T_s. This is an indication of an increase in the average crystallite-size and preferred orientation of the film along (00l) with increasing T_s. The later is dominant for WO_3 films grown at $T_s \geq 200$ °C. Also, a structural transformation occurs at T_s=300 °C. XRD peaks due to tetragonal (t-WO_3) phase are clearly seen for WO_3 films grown at $T_s \geq 400$ °C. The peak positions in XRD were determined using TOPAS (Bruker) software and the "crystallite-size" was measured using the Scherrer's equation.[18] The average size increases from 9 to 50 nm with increasing T_s from 100 to 500 °C. High-temperature t-WO_3 seems to be the effect of phase stabilization at the nanoscale dimensions. The preferred *c*-axis orientation could be due to the growth process minimizing the internal strain-energy in the film. Anisotropy exists in crystalline materials and the strain energy densities will typically be different for different crystallographic direction.[16–18] The growth will favor those orientations with low strain energy density. Therefore, increasing T_s favors the preferred orientation along (00l) while minimizing the strain-energy in the WO_3 film.

The optical transmittance (T) spectra of WO_3 films are shown in Fig. 2. The dip noticed in the spectra is due to interference. The spectra reveal two important characteristic

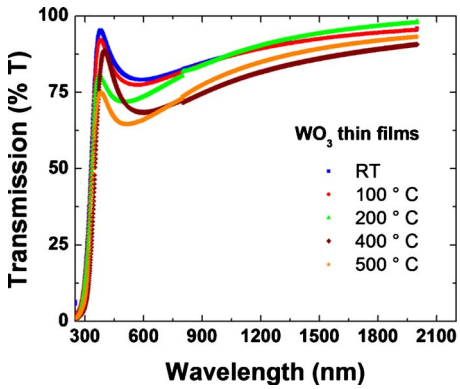

FIG. 2. (Color online) Optical transmittance spectra of WO_3 films. The curves indicate that WO_3 films are highly transparent.

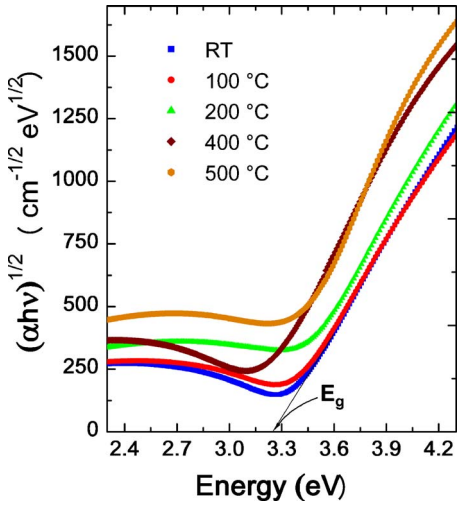

FIG. 3. (Color online) $(\alpha h\nu)^{1/2}$ vs $h\nu$ plots for WO_3 films. Linear fits of the absorption data indicate the indirect band gap of WO_3 films. The extrapolation of the linear region to $h\nu$=0 to determine E_g values is as indicated with lines. The arrow indicates the shift in E_g as a result of size reduction leading to QC effects.

features. (1) All the WO_3 films show a very high transparency in the spectral region except where the incident radiation is absorbed across the band gap (E_g). This observation indicates the high-quality and transparent nature of WO_3 films with almost zero absorption losses. (2) A decrease in T with increasing T_s. However, the decrease is not significant for $T_s < 300$ °C, whereas a clear distinction is seen for $T_s \geq 300$ °C.

It is well known that the optical absorption below E_g follows an exponential behavior.[19] The absorption, therefore, is exponentially dependent on the energy ($h\nu$) of incident photon in that region. For WO_3, in the E_g region (high absorption) or above the fundamental absorption edge, the absorption follows a power law of the form[1,5,20,21]

$$(\alpha h\nu) = B(h\nu - E_g)^2, \quad (1)$$

where $h\nu$ is the energy of the incident photon, α the absorption coefficient, B the absorption edge width parameter, E_g the band gap. The optical absorption coefficient, α, of the films is evaluated using the relation[19–22]

$$\alpha = [1/t]\ln[T/(1-R)^2], \quad (2)$$

where T is the transmittance, R is the reflectance and t is the film thickness. The absorption data and the plots obtained for WO_3 films are shown in Fig. 3. It is evident that $(\alpha h\nu)^{1/2}$ vs $h\nu$ results in linear plots in the high absorption region, $\alpha > 10^4$ cm^{-1}, suggesting indirect allowed transitions across E_g of WO_3 films. The E_g values determined by extrapolating the linear region of the plot to $h\nu$=0, decreases from 3.25 to 2.92 eV with increasing T_s. The possibility of direct allowed transitions is ruled out since similar procedure results in $E_g \sim 4$ eV, which is not reasonable for WO_3. The functional relationship obtained between T_s and E_g is shown in Fig. 4. It is clear that the T_s-E_g data exhibits a linear inverse relationship (Fig. 4).

The size-phase-property relationship in nanocrystalline WO_3 films can be derived based on the observed results and taking the simultaneous effect of size and structural transformations into account. The results indicate that the microstructure has significant effect on the optical properties of

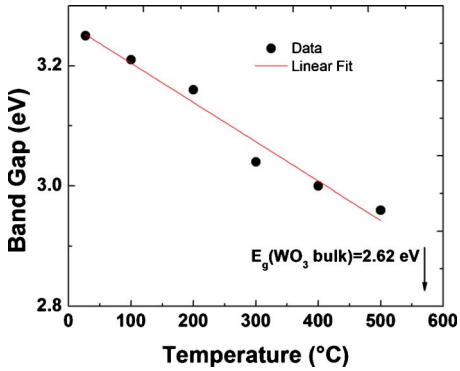

FIG. 4. (Color online) (a) T_s-E_g relationship in WO_3 films. A direct inverse relationship is evident; a line is provided not only to guide the eye but also to indicate the linear fit.

nanocrystalline WO_3 films. In WO_3, E_g corresponds to electronic transitions from the top of valence band (formed by the filled O $2p$ orbitals) to the conduction band (formed by the empty W $5d$ orbitals).[20,23] $E_g(WO_3$ bulk)=2.62 eV.[24] E_g widening in WO_3 films with relatively smaller size is mainly due to quantum-confinement (QC) effects. The shift in E_g due to the size-effect can theoretically be described based on the two QC regimes, strong and weak.[25,26] The former is a case where the electrons and holes are independently confined when the size of a nanocrystal (R_n) is much smaller than the size of Bohr radius (R_B).[25–27] In the later case of weak QC, the energy is dominated by the Coulomb term and quantum effects arise from quantization of exciton motion. The E_g shift is relatively smaller in the latter case.[27,28] WO_3 nanocrystals exhibit a weak QC effect.[28] This accounts for the observed E_g widening and shift by 0.58 eV. The highest E_g (3.25 eV) at T_s=RT is due to formation of a-WO_3 phase. The effect of a-WO_3 to m-WO_3 transition is not significant; $E_g > 3$ eV for nanocrystalline m-WO_3 films can be attributed to the size reduction. Most importantly, it is very interesting to note that the T_s-E_g data exhibits a direct, inverse linear relationship where the combined effect of size increase and structural transformation is evident. Such a size-E_g inverse relationship, which was attributed to QC effects, was also reported in CdS,[26] CdTe–TiO_2,[27] ZrO_2,[29] ZnO,[30] and most recently in WO_3.[28] A drop in E_g by $\sim$0.25 eV for WO_3 films grown at T_s=300 °C could be due to size$>$30 nm and phase transition to t-WO_3. Surface roughening can be accounted for a decrease in transmittance (Fig. 2) at higher T_s. The random distribution of the grains makes the surface rough and results in the increased light-scattering losses. Furthermore, an increase in the scattering coefficient would decrease the optical transmittance in the UV and visible region.[29] This feature was clearly observed in the optical spectra (Fig. 2) with increasing T_s which supports the idea of scattering losses due to surface roughening.

Summarizing the results, amorphous and nanocrystalline WO_3 films were fabricated using sputter-deposition and their structural and optical properties were investigated. The size-effects were significant on the optical characteristics of WO_3 films; the microstructure dependence is remarkably evident in the optical spectra and E_g analysis. WO_3 films grown at RT were amorphous and transform to m-WO_3 at T_s =100 °C. The wide band gap for WO_3 films (3.25–3.17 eV; T_s=RT−200 °C) is due to a size reduction and formation of nanoclusters leading to QC. E_g decreases to 2.92 eV with increasing size to 50 nm while the WO_3 films exhibit a structural transformation to t-WO_3. A direct linear inverse T_s-E_g relationship found for WO_3 films suggest that tuning optical properties can be achieved by controlling the size and phase.

This material is based upon work supported by the Department of Energy under Award No. DE-PS26-08NT00198-00.

[1]C. G. Granqvist, *Handbook of Inorganic Electrochromic Materials* (Elsevier, New York, 1995).
[2]Y. Zhang, S. H. Lee, A. Mascarenhas, and S. K. Deb, Appl. Phys. Lett. **93**, 203508 (2008).
[3]C. V. Ramana, S. Utsunomiya, R. C. Ewing, C. M. Julien, and U. Becker, J. Phys. Chem. B **110**, 10430 (2006).
[4]L. Berggren, J. C. Jonsson, and G. A. Niklasson, J. Appl. Phys. **102**, 083538 (2007).
[5]Y. S. Lin, H. T. Chen, and J. Y. Lai, Thin Solid Films **518**, 1377 (2009).
[6]Dy Lu, J. Chen, H. J. Chen, J. Gong, S. Z. Deng, N. S. Xu, and Y. L. Liu, Appl. Phys. Lett. **90**, 041919 (2007).
[7]F. Ménil, V. Coillard, and C. Lucat, Sen. Actuators B **67**, 1 (2000).
[8]M. Stankova, X. Vilanova, E. Llobet, J. Calderer, C. Bittencourt, J. J. Pireaux, and X. Correig, Sen. Actuators B **105**, 271 (2005).
[9]G. Xie, J. Yu, X. Chen, and Y. Jiang, Sen. Actuators B. **123**, 909 (2007).
[10]S. Santucci, C. Cantalini, M. Crivellari, L. Lozzi, L. Ottaviano, and M. Passacantanso, J. Vac. Sci. Technol. A **18**, 1077 (2000).
[11]P. I. Gouma and K. Kalyanasundaram, Appl. Phys. Lett. **93**, 244102 (2008).
[12]T. P. Huelser, A. Lorke, P. Ifeacho, H. Wiggers, and C. Schulz, J. Appl. Phys. **102**, 124305 (2007).
[13]T. Vogt, P. M. Woodward, and P. A. Hunter, J. Solid State Chem. **144**, 209 (1999).
[14]E. Cazzanelli, C. Vinegoni, G. Mariotto, G. Kuzmin, and J. Purans, J. Solid State Chem. **143**, 24 (1999).
[15]R. Chatten, A. Chadwick, A. Rougier, and J. Lindan, J. Phys. Chem. B **109**, 3146 (2005).
[16]C. V. Ramana, R. J. Smith, and C. M. Julien, J. Vac. Sci. Technol. A **22**, 2453 (2004).
[17]C. V. Ramana, K. Zaghib, and C. M. Julien, Appl. Phys. Lett. **90**, 021916 (2007).
[18]The Scherrer equation is $d=0.9\lambda/\beta\cos\theta$, where d is the size, λ is the wavelength of the filament used in the XRD machine, β is the width of a peak at half of its intensity, and θ is the angle of the peak.
[19]F. Z. Tepehan, F. E. Ghodsi, N. Ozer, and G. G. Tepehan, Sol. Energy Mater. Sol. Cells **59**, 265 (1999).
[20]E. Washizu, A. Yamamoto, Y. Abe, M. Kawamura, and K. Sasaki, Solid State Ionics **165**, 175 (2003).
[21]A. Subrahmanyam and A. Karuppasamy, Sol. Energy Mater. Sol. Cells **91**, 266 (2007).
[22]P. Tyagi and A. G. Vedeshwar, Phys. Rev. B **66**, 075422 (2002).
[23]M. Deepa, A. K. Srivastava, M. Kar, and S. A. Agnihotry, J. Phys. D **39**, 1885 (2006).
[24]F. P. Koffyberg, K. Dwight, and A. Wold, Solid State Commun. **30**, 433 (1979).
[25]J. E. Brus, J. Chem. Phys. **80**, 4403 (1984).
[26]A. D. Yoffe, Adv. Phys. **42**, 173 (1993).
[27]A. C. Rastogi, S. N. Sharma, and S. Kohli, Semicond. Sci. Technol. **15**, 1011 (2000).
[28]R. Alan May, L. Kondrachova, B. P. Hahn, and K. J. Setvenson, J. Phys. Chem. C **111**, 18251 (2007).
[29]C. V. Ramana, R. S. Vemuri, I. Fernandez, and A. L. Campbell, Appl. Phys. Lett. **95**, 231905 (2009).
[30]S. T. Tan, B. J. Chen, X. W. Sun, W. J. Fan, H. S. Kwok, X. H. Zhang, and S. J. Chua, J. Appl. Phys. **98**, 013505 (2005).

Tungsten oxide (WO_3) thin films for application in advanced energy systems

S. K. Gullapalli and R. S. Vemuri
Department of Mechanical Engineering, University of Texas at El Paso, El Paso, Texas 79968

F. S. Manciu and J. L. Enriquez
Department of Physics, University of Texas at El Paso, El Paso, Texas 79968

C. V. Ramana[a)]
Department of Mechanical Engineering, University of Texas at El Paso, El Paso, Texas 79968

(Received 16 October 2009; accepted 22 February 2010; published 29 June 2010)

Inherent processes in coal gasification plants produce hazardous hydrogen sulfide (H_2S), which must be continuously and efficiently detected and removed before the fuel is used for power generation. An attempt has been made in this work to fabricate tungsten oxide (WO_3) thin films by radio-frequency reactive magnetron-sputter deposition. The impetus being the use of WO_3 films for H_2S sensors in coal gasification plants. The effect of growth temperature, which is varied in the range of 30–500 °C, on the growth and microstructure of WO_3 thin films is investigated. Characterizations made using scanning electron microscopy (SEM) and x-ray diffraction (XRD) indicate that the effect of temperature is significant on the microstructure of WO_3 films. XRD and SEM results indicate that the WO_3 films grown at room temperature are amorphous, whereas films grown at higher temperatures are nanocrystalline. The average grain-size increases with increasing temperature. WO_3 films exhibit smooth morphology at growth temperatures $\leq$300 °C while relatively rough at >300 °C. The analyses indicate that the nanocrystalline WO_3 films grown at 100–300 °C could be the potential candidates for H_2S sensor development for application in coal gasification systems. © *2010 American Vacuum Society.* [DOI: 10.1116/1.3368495]

I. INTRODUCTION

Advanced energy systems capable of delivering the energy efficiently are increasingly receiving attention in recent years. Coal gasifiers, which utilize coal for gasification to produce cleaner fuels and energy, are capable of delivering a continuous, large scale energy supply.[1–4] However, these systems are based on fossil fuels and the pollutants released during gasification must be monitored and controlled. Sulfur is a natural contaminant in fossil fuel supplies. When coal is gasified, the sulfur manifests itself in the form of hydrogen sulfide (H_2S), which is corrosive and highly toxic.[5,6]

The undesirable H_2S emissions from coal gasification plants must be effectively monitored, controlled, and removed for efficient power generation.[5,6] Therefore, reliable, fast, highly sensitive, and selective sensors which can withstand high temperature and chemically corrosive environment are desired for detecting and monitoring even very low concentrations of H_2S emissions. Tungsten oxide (WO_3) is a promising material for gas sensors due to its electrical conductivity and excellent sensitivity and selectivity.[7–11] WO_3 films exhibit excellent functional activity to various gases such as H_2S, NO_x, trimethylamine, and other organic compound gases.[7–12]

The present work has been performed on the microstructure and chemical bonding analysis of WO_3 films grown by sputter deposition. Specifically, the effect of growth temperature on the microstructure and chemical properties has been investigated in detail. The impetus for the work is to optimize the conditions to produce high-quality WO_3 thin films for application in H_2S sensors for use in coal gasification systems. An understanding of the crystal structure, surface morphology evolution, and electronic properties is very important since they have a significant impact on the sensitivity, selectivity, and stability of the sensor. In this work, we found that the growth temperature, varied from room temperature (RT) to 500 °C, has a significant effect on the structure and morphology of WO_3 films. The results obtained are presented, discussed, and microstructure-temperature dependence is established in sputter-deposited WO_3 films.

II. EXPERIMENT

A. Preparation

WO_3 thin films were deposited onto silicon (Si) wafers by radio-frequency magnetron sputtering. The Si(100) substrates were cleaned by RCA cleaning. All the substrates were thoroughly cleaned and dried with nitrogen before introducing them into the vacuum chamber, which was initially evacuated to a base pressure of $\sim 10^{-6}$ Torr. Tungsten (W) metal target (Plasmaterials Inc.) of 3 in. diameter and 99.95% purity was employed for reactive sputtering. The W-target was placed on a 3 in. sputter gun, which is placed at a distance of 8 cm from the substrate. A sputtering power of 40 W was initially applied to the target while introducing high purity argon (Ar) into the chamber to ignite the plasma.

a)Author to whom correspondence should be addressed; electronic mail: rvchintalapalle@utep.edu

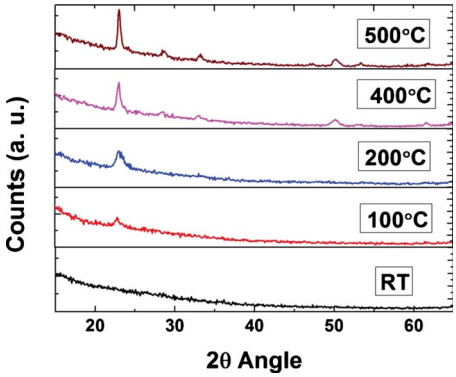

FIG. 1. (Color online) XRD patterns of WO_3 films. The evolution of peak corresponding to (002) reflection at 23.1° can be seen as function of growth temperature for WO_3 films.

Once the plasma was ignited the power was increased to 100 W and oxygen (O_2) was released into the chamber for reactive deposition. The flow of the Ar and O_2 and their ratio was controlled using as MKS mass flow meters. Before each deposition, the W-target was presputtered for 10 min using Ar alone with shutter above the gun closed. The deposition was carried out for 1 h. The samples were deposited at different temperatures varying from RT to 500 °C. The substrates were heated by halogen lamps and the desired temperature was controlled by Athena X25 controller.

B. Characterization

WO_3 films were characterized by studying their crystal structure, surface morphology, and chemical bonding. X-ray diffraction (XRD) measurements on WO_3 films were by performed using a Bruker D8 Advance x-ray diffractometer. All the measurements were made *ex situ* as a function of growth temperature. XRD patterns were recorded using Cu Kα radiation ($\lambda = 1.540\,56$ Å) at RT. Surface imaging analysis was performed using a high performance and ultrahigh resolution scanning electron microscope (Hitachi S-4800). The secondary electron imaging was performed on WO_3 films grown on Si wafers using carbon paste at the ends to avoid charging problems. The grain detection, size analysis, and statistical analysis was performed using the software provided with the SEM

III. RESULTS AND DISCUSSION

A. Structure

The XRD patterns of WO_3 films are shown in Fig. 1 as a function of growth temperature. The XRD curve of WO_3 films grown at RT did not show any peaks. The XRD peak corresponding to WO_3 phase appears when the temperature is 100 °C. However, the peak (at 23.1°) is rather broad indicating the presence of very small particles which is also confirmed by SEM measurements. It is evident (Fig. 1) that the intensity of the peak, at 23.1°, which corresponds to diffraction from (002) planes increase with increasing temperature indicating the following characteristic features. An increase in the average crystallite size with increasing temperature is the first. A preferred orientation of the film along (002) is the second. The latter is dominant for WO_3 films grown at temperatures $\geq$200 °C which can be attributed to increasing degree of preferred orientation with increasing temperature. Ramana *et al.*[13,14] have proposed that the preferred orientation and the degree of orientation in nanocrystalline and microcrystalline oxide films on the specific substrates occur to minimize the internal strain- energy in the film. As shown by Ramana *et al.* for pulsed-laser deposited V,[13] Mo,[14] Ni–Co,[15] and W oxides[11] and most recently by Chawla *et al.*[16] for nanocrystalline WO_3 films, anisotropy exists in crystalline materials and the strain energy densities will typically be different for different crystallographic direction and the growth will favor those orientations with low strain energy density. The preferred (002) orientation of WO_3 films, therefore, can be explained based on the growth process minimizing the internal strain-energy in the film. An increase in temperature favors the preferred orientation along (002) while minimizing the strain-energy in the WO_3 film on Si(100) surface. These results are in good agreement with the recent reported results on WO_3 thin films although the mechanism was not discussed.[17]

B. Surface morphology

The high resolution SEM images of WO_3 films as a function of substrate temperature are shown in Figs. 2 and 3. The effect of temperature on the surface morphology of WO_3 films is remarkable. As it is evident from these images, the SEM data of WO_3 films can be divided into two categories where the morphology differences are significant. The first category contains the set of WO_3 films grown at temperatures $\leq$200 °C (Fig. 2). The second is the set of WO_3 films grown at temperatures >200 °C (Fig. 3). No features can be seen for WO_3 films grown at RT even at very high magnifications [Fig. 2(a)]. This observation is in agreement with the XRD results indicating the complete amorphous nature of the samples. If temperature is low such that the period of the atomic jump process of adatoms on the substrate surface is very large, the condensed species may stay stuck to the regions where they are landing thus leading to an amorphous WO_3 film. The adatom mobility on the surface increases with increasing temperature. The small, dense particles spherical in shape can be noticed in SEM images [Figs. 2(b) and 2(c)] for WO_3 films grown at 100–200 °C. The fine microstructure and uniform distribution characteristics of the particles are evident in the micrographs [Figs. 2(b) and 2(c)]. The average particle size is 10–14 nm. The SEM data along with appearance of diffraction peaks in XRD clearly indicate that 200 °C is the critical temperature to promote the growth of nanocrystalline WO_3 films with particles in spherical shape. For the given set of experimental conditions, a temperature of 200 °C is, therefore, favorable to provide sufficient energy for WO_3 crystallization.

The XRD and SEM results suggest that a further increase in temperature beyond 200 °C results in changes in the crystal structure and morphology. WO_3 films continue to show

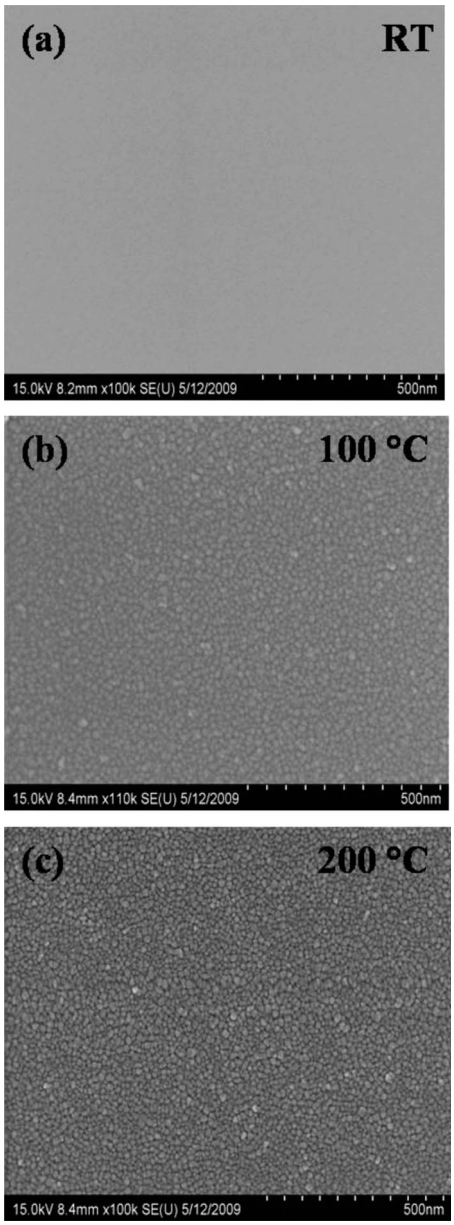

FIG. 2. SEM images of WO_3 films grown at temperatures ≤200 °C. The characteristic spherical particle morphology along with a uniform distribution is evident for WO_3 films grown at 100 and 200 °C.

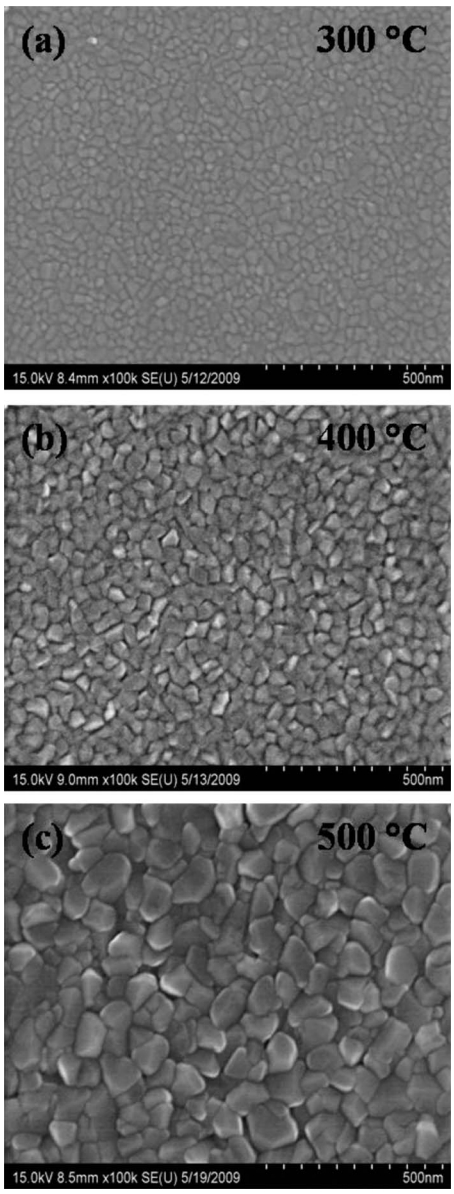

FIG. 3. SEM images of WO_3 films grown at temperatures >200 °C. The changes in morphology with temperature are evident.

preferred growth along with an increase in average particle size with increasing temperature. It can be seen in SEM images (Fig. 3) that increasing temperature above 200 °C results in size >20 nm. The highest particle size (62 nm) is measured for WO_3 films grown at 500 °C. However, it can be also seen in the images that the distribution of particles become random with increasing temperature. The spherical morphology noticed for WO_3 films grown at ≤200 °C is also changed with increase in temperature above 200 °C. A functional relationship obtained between the average particle size (L) and the temperature is shown in Fig. 4. At a constant partial pressure ($Ar:O_2 \approx 1:6$), the temperature-size data fit to an exponential growth function (Fig. 4). The data support thermally activated growth process of nanocrystalline WO_3 thin films. Therefore, similar to the diffusion coefficient equation,[18] L can be expressed as

$$L = L_o \exp(-\Delta E/k_B T), \tag{1}$$

where L is the average particle size, L_0 is a pre-exponential factor or proportionality constant which depends on the specific film, substrate materials involved, E the activation energy, k_B the Boltzmann constant, and T the absolute temperature. The data analysis and Arrhenius plot are presented in Fig. 5, where the data points and a linear fit to the data are shown. It is important to recognize the functional linear relationship which is an indicative of thermally driven growth of nanocrystalline WO_3 films. The activation energy derived from the slope of the linear fit (Fig. 5) is ~0.15 eV. A direct comparison of this value with any other reports is not pos-

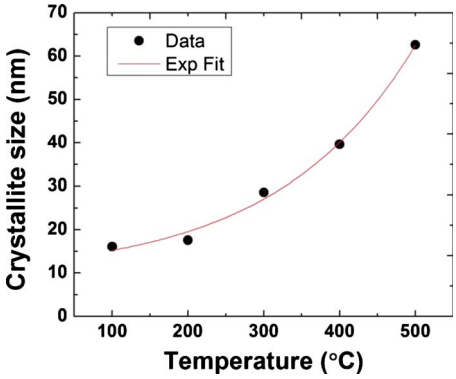

FIG. 4. (Color online) Grain-size variation with temperature for sputter-deposited WO_3 thin films. The experimental data are shown with solid circles while the line is an exponential fit. The data fit to an exponential growth function indicating thermally activated growth process of nanocrystalline WO_3 thin films.

sible at this time since the data or such analysis is not available for nanocrystalline WO_3 films grown by sputtering or any other physical/chemical vapor deposition methods. However, this value is rather small, but expected for nanocrystalline films, when compared to the data of some of the microcrystalline transition metal oxide thin films.[13,19]

The cross-sectional SEM images of WO_3–Si interfaces for WO_3 films grown at various temperatures are shown in Fig. 6. The WO_3 film and Si-substrate regions are as indicated. The cross-sectional SEM images indicate that the WO_3 films grow in a columnar structure on Si surfaces. A sharp interface, within the limits of the resolution of instrument, is seen between the Si substrate and the oxide layer for all WO_3 films. The cross-sectional imaging analysis indicates that there is no reaction leading to compound formation at the Si–WO_3 interface even at the highest temperature (500 °C).

C. Chemical quality

The energy dispersive spectroscopy (EDS) spectra of representative WO_3 films as a function of growth temperature are shown in Fig. 7. The spectra indicate the characteristic x-ray peaks (as labeled in Fig. 7) corresponding to W and O

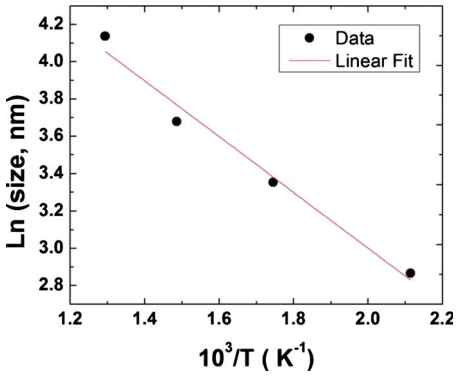

FIG. 5. (Color online) Arrhenius plot of size-temperature dependence. The linear fit is represented with a solid line.

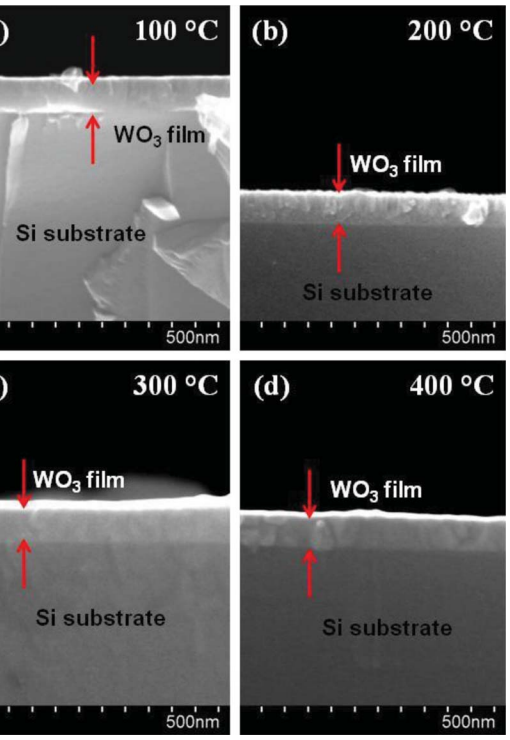

FIG. 6. (Color online) Si–WO_3 cross-sectional SEM images of WO_3 films grown at various temperatures. The Si substrate and WO_3 film regions are as indicated.

atoms present in the sample. The absence of any other peaks except those due to W and O indicate that the sample consists exclusively of W-oxide phase. It is well known that the x rays generated are characteristic of the atoms.[20,21] Therefore, the detection of x rays emitted from the sample as a result of sample-electron beam interaction provides the identification of the atoms present in the crystal. The emitted x-ray peaks detected are only from W and O while the peak due to Si substrate is serving as a reference. No other elements were detected, which is a sign of high purity WO_3 without any elemental impurities incorporated from chemical processing or postpreparation handling. However, it can be seen in the spectra that the peak intensity of O is slightly

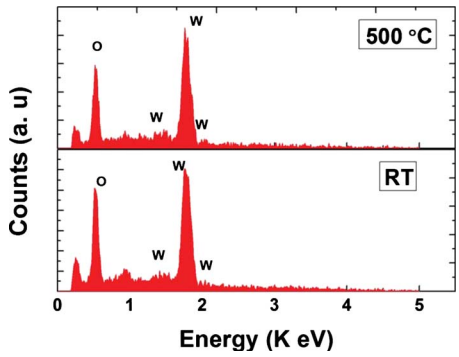

FIG. 7. (Color online) EDS spectra of WO_3 films grown at various temperatures. The x-ray peaks due to W and O atoms present in the grown films are as labeled.

decreased when the temperature is increased to 500 °C. This could be due to formation a small fraction of oxygen vacancies at higher deposition temperatures.

IV. SUMMARY AND CONCLUSIONS

WO_3 thin films have been fabricated onto Si(100) surfaces by sputter-deposition by varying the growth temperature from RT to 500 °C. The effect of growth temperature on the on the growth, structure, surface/interface morphology, and chemical quality of WO_3 thin films is investigated. Characterizations made using scanning electron microscopy (SEM) and x-ray diffraction (XRD) indicate that the effect of temperature is significant on the growth behavior and microstructure of WO_3 thin films. The results reveal that the WO_3 thin films grown at RT are amorphous while the films grown at higher temperatures are nanocrystalline. The average grain size increased from 12 to 62 nm with increasing temperature from 100 to 500 °C. WO_3 films grown at temperatures $\geq$200 °C exhibit the (002) preferred orientation. WO_3 films exhibit smooth morphology at growth temperatures $\leq$300 °C while relatively rough at $>$300 °C. The analyses indicate that the nanocrystalline WO_3 films grown at 100–300 °C could be the potential candidates for H_2S sensor development for application in coal gasification systems.

ACKNOWLEDGMENT

This material is based upon work supported by the Department of Energy under Award No. DE-PS26-08NT00198-00.

[1]G. J. Stiegel and M. Ramezan, Int. J. Coal Geol. **65**, 173 (2006).
[2]A. J. Minchener, Fuel **84**, 2222 (2005).
[3]J. P. Longwell, E. S. Rubin, and J. Wilson, Prog. Energy Combust. Sci. **21**, 269 (1995).
[4]N. Crnomarkovic, B. Repic, R. Mladenovic, O. Neskovic, and M. Veljkovic, Fuel **86**, 194 (2007).
[5]F. Vandecruys, E. Brauns, W. Engelen, F. De Shutter, and J. Vangrunderbeek, Solid State Ionics **112**, 95 (1998).
[6]J. Vangrunderbeek, F. Vandecruys, and R. V. Kumar, Sens. Actuators B **56**, 129 (1999).
[7]F. Ménil, V. Coillard, and C. Lucat, Sens. Actuators B **67**, 1 (2000).
[8]M. Stankova, X. Vilanova, E. Llobet, J. Calderer, C. Bittencourt, J. J. Pireaux, and X. Correig, Sens. Actuators B **105**, 271 (2005).
[9]G. Xie, J. Yu, X. Chen, and Y. Jiang, Sens. Actuators B **123**, 909 (2007).
[10]S. Santucci, C. Cantalini, M. Crivellari, L. Lozzi, L. Ottaviano, and M. Passacantanso, J. Vac. Sci. Technol. A **18**, 1077 (2000).
[11]C. V. Ramana, S. Utsunomiya, R. C. Ewing, C. M. Julien, and U. Becker, J. Phys. Chem. B **110**, 10430 (2006).
[12]S. Djerad, L. Tifouti, M. Crocoll, and W. Weisweiler, J. Mol. Catal. A: Chem. **208**, 257 (2004).
[13]C. V. Ramana, R. J. Smith, and C. M. Julien, J. Vac. Sci. Technol. A **22**, 2453 (2004).
[14]C. V. Ramana and C. M. Julien, Chem. Phys. Lett. **428**, 114 (2006).
[15]C. V. Ramana, K. Zaghib, and C. M. Julien, Appl. Phys. Lett. **90**, 021916 (2007).
[16]A. K. Chawla, S. Singhal, H. O. Gupta, and R. Chandra, Thin Solid Films **517**, 1042 (2008).
[17]M. Regragui, V. Jousseaume, M. Addou, A. Outzourhit, J. C. Bernéde, and B. El Idrissi, Thin Solid Films **397**, 238 (2001).
[18]C. Kittel, *Introduction to Solid State Physics* (Wiley, New York, 1968).
[19]G. J. Fang, K. L. Yao, and Z. L. Liu, Thin Solid Films **394**, 63 (2001).
[20]C. V. Ramana, A. Ait-Salah, S. Utsunomiya, U. Becker, A. Mauger, F. Gendron, and C. M. Julien, Chem. Mater. **18**, 3788 (2006).
[21]J. Goldstein, D. Newbury, D. Joy, C. Lyman, P. Echlin, E. Lifshin, L. Sawyer, and J. Michael, *Scanning Electron Microscopy and X-ray Microanalysis* (Kluwer Academic/Plenum, New York, 2003).

ACS APPLIED MATERIALS & INTERFACES

Research Article

www.acsami.org

Optical Constants of Amorphous, Transparent Titanium-Doped Tungsten Oxide Thin Films

C. V. Ramana,* Gaurav Baghmar, Ernesto J. Rubio, and Manuel J. Hernandez

Department of Mechanical Engineering, University of Texas at El Paso, El Paso, Texas 79968, United States

ABSTRACT: We report on the optical constants and their dispersion profiles determined from spectroscopic ellipsometry (SE) analysis of the 20%-titanium (Ti) doped of tungsten oxide (WO_3) thin films grown by sputter-deposition. The Ti-doped WO_3 films grown in a wide range of temperatures (25−500 °C) are amorphous and optically transparent. SE data indicates that there is no significant interdiffusion at the film−substrate interface for a W−Ti oxide film growth of ∼90 nm. The index refraction (n) at λ = 550 nm vary in the range of 2.17−2.31 with a gradual increase in growth temperature. A correlation between the growth conditions and optical constants is discussed.

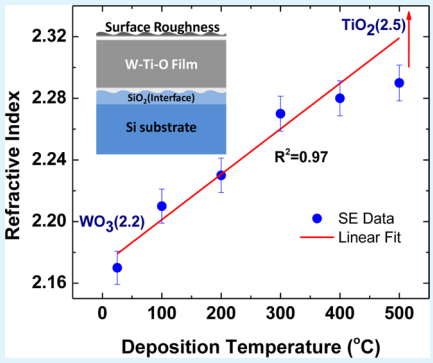

KEYWORDS: *tungsten oxide, Ti-doping, sputter-deposition, microstructure, optical constants*

I. INTRODUCTION

Tungsten oxide (WO_3) is an intensively studied "chromogenic" material because of the coloration effects associated with various processes.[1−6] There has been a great deal of recent interest in low-dimensional structures, such as nanorods, nanowires, nanoparticles and ultrathin films, of WO_3 for a wide variety of applications in optoelectronics, microelectronics, photovoltaic devices, selective catalysis, and environmental engineering.[2−40] WO_3 has been in use for the development of smart windows for energy-efficient architecture of buildings and automobiles, flat-panel displays, optical memory and writing−reading−erasing devices, and electronic information displays.[1−6] Most recently, WO_3 based materials are considered and demonstrated to be attractive for application in photoelectrochemical cells (PECs) for hydrogen production by water-splitting.[19−21] In addition, new application of WO_3 in emerging dye-sensitized solar cells (DSSC) technology has been demonstrated recently.[22] While the efficiency is not comparable to those employing the most studied TiO_2-based DSSCs, options to tailor the microstructure and chemistry in order to improve the efficiency exists.[22,23]

The optical, photochemical, and electrical properties of metal oxide thin films grown from either chemical or physical vapor deposition methods are sensitive to the physical and chemical characteristics, which in turn depend on the processing conditions and precursor materials.[2−40] For instance, the density of TiO_2, SiO_2 HfO_2 and ZrO_2 thin films was shown to be sensitive to the processing conditions and influence the index of refraction of resulting films greatly.[41−43] Furthermore, oxides differ in stoichiometry, depending on the preparation conditions, leading to substantial changes in the electronic properties.[2−43] From this point of view, a detailed understanding and control over the physical parameters and optical properties of pure or doped W-oxide based thin films is required in order to optimize performance for a given application. In this article, we investigate and report on the observed amorphization and optical constants of titanium (Ti) doped WO_3 films grown by reactive sputter-deposition under varying growth temperature.

The relevance and current interest in Ti-doped oxide materials is derived from the following considerations. Recently, it has been demonstrated in several cases that either Ti metal doping or capping will alter the electronic structure of the oxide in order to benefit the properties and device performance.[44−51] Enhancement in the electrical conductivity, luminescence, sensing ability, and photocatalytic performance are the benefits expected and/or reported in the literature under controlled Ti incorporation or TiO_2-coupling with other oxides.[44−53] It has been reported that the near band edge luminescence enhances 5 times when in Ti/ZnO nanorod heterostructures, where Ti is sputtered onto ZnO at 400 °C.[44] Surface diffusion of Ti with a effective reduction in surface defects is accounted for by the enhanced luminescence of Ti/ZnO nanorod heterostructures.[44] For the specific case of W−Ti−O materials, while TiO_2 is a well-studied photocatalyst, coupling TiO_2 with WO_3 can extend the optical absorption to the visible region to enhance the photocatalytic efficiency.[45−50] Recently, studies focused on the TiO_2−WO_3 system proved the enhanced photocatalytic performance of such materials.[45−51] It has been pointed out that the key will be the specific composition and associated effect on the electronic structure and band gap.[45−51] It has been demonstrated that W−Ti mixed oxides exhibit enhanced

Received: October 31, 2012
Accepted: April 9, 2013
Published: May 17, 2013

selectivity and sensitivity to certain chemicals for their utilization in integrated sensors.[52,53] Most recently, we have demonstrated that the electrical conductivity of 5% Ti-doped WO_3 can be enhanced compared to that of pure WO_3 films.[54,55] Therefore, investigating the fundamental aspects of microstructure evolution and structure−property relationships in W−Ti−O films may provide opportunities to tailor the microstructure and optical properties of the materials for the desired application. Specifically, if high optical transparency and improved electrical conductivity is demonstrated, there is a possibility to realize the new set of materials based on W−Ti mixed oxides, which can serve as transparent conducting electrodes for application in emerging of solar cell and optoelectronics technology. The results obtained of the optical constants of Ti-doped amorphous, transparent WO_3 films are reported in this paper.

II. EXPERIMENTAL SECTION

A. Film Growth. Titanium (20%) doped WO_3 thin films were deposited onto silicon (Si) wafers and optical grade quartz substrates by radio frequency (rf) (13.56 MHz) magnetron sputtering. The Si(100) wafers and quartz substrates were cleaned by RCA and chemical cleaning, respectively, as reported elsewhere.[54−57] After cleaning, all the substrates were dried with nitrogen before introducing them into the vacuum chamber, which was initially evacuated to a base pressure of ∼10^{-6} Torr. A W−Ti ($W_{0.8}Ti_{0.2}$) alloy target (Plasmaterials Inc.) of 2 in. diameter and 99.95% purity was employed for reactive sputtering. The $W_{0.8}Ti_{0.2}$-target was placed on a 2-in. sputter gun, which was correspondingly placed at a distance of 8 cm from the substrate. A sputtering power of 40 W was initially applied to the target while introducing high-purity argon (Ar) into the chamber causing plasma ignition. Once ignited, the power was increased to 100 W, and oxygen (O_2) was released into the chamber for reactive deposition. The flow of the Ar and O_2 and their ratio was controlled using MKS mass flow meters. Before each deposition, the $W_{0.8}Ti_{0.2}$-target was presputtered for 10 min using Ar alone with the shutter above the gun closed. The samples were deposited at different temperatures (T_s) varying from RT to 500 °C. The substrates were heated by halogen lamps, and the desired temperature was controlled by an Athena X25 controller. The deposition was made for 1 h duration to obtain a film thickness of ∼90 nm. The film thickness was verified with various analytical methods to ensure that films are with a reasonably constant thickness for comparison of the data and analysis presented and to understand the effect of growth temperature on the structure and properties.

B. Characterization. The grown Ti-doped WO_3 films were characterized by performing structural and optical measurements. X-ray diffraction (XRD) measurements on the samples grown on Si(100) were performed by using a Bruker D8 Advance X-ray diffractometer. In order to avoid interference by the substrate and obtain diffraction pattern of the coatings, grazing incidence X-ray diffraction (GIXRD) was performed on the films. All the measurements were made ex-situ as a function of T_s. GIXRD patterns were recorded using Cu Kα radiation (λ = 1.540 56 Å) at RT. A high voltage of 40 kV was used to generate the X-rays. The GIXRD patterns were recorded employing the X-ray beam fixed at a grazing incidence of 1°. The scanning was performed in a 2θ range of 15−70° using the "detector scan" mode, where the detector was independently moved in the plane of incidence to collect the diffraction pattern. The step size and the scan speed were 0.05° (2θ) and 5°/min, respectively. For these set of conditions, the X-ray beam passes a sufficiently long distance through the coating to provide the observed diffraction patterns. Surface imaging analysis was performed using a high-performance and ultra high resolution scanning electron microscope (Hitachi S-4800). The secondary electron imaging was performed on W−Ti−O films grown on Si wafers using carbon paste at the ends to avoid charging problems.

The optical properties and surface/interface characteristics were probed by spectroscopic ellipsometry (SE). The measurements were made using a W. A. Woollam VVASE spectroscopic ellipsometer operating in the wavelength range of 250−1350 nm with a step size of 2 nm and at angles of incidence of 65°, 70°, and 75°, near the Brewster's angle of silicon. Number of revolutions per measure was set at 20. The ellipsometry data analysis was performed using commercially available WVASE32 software.[58]

In addition to ellipsometry measurements, spectrophotometric measurements were also employed to probe the transparent nature and band gap analysis of the W−Ti−O films. Spectrophotometric measurements were made using a Cary 5000 UV−vis-NIR double-beam spectrophotometer. W−Ti−O films grown on optical grade quartz were employed for these measurements. The quartz substrates employed extends the transparency range down to ∼190 nm and determines the absorption edge extending into the ultraviolet (UV) region, which is more than sufficient to determine the band gap shift in deficient or stoichiometric or metal incorporated WO_3 films, specifically the Ti-doped tungsten oxide films in this case.

III. OPTICAL MODEL AND THEORY

Optical constants of the Ti-doped WO_3 films were primarily probed by SE, which measures the relative changes in the amplitude and phase of the linearly polarized monochromatic incident light upon oblique reflection from the sample surface. The experimental parameters obtained by SE are the angles Ψ (azimuth) and Δ (phase change), which are related to the microstructure and optical properties, defined by[59−62]

$$\rho = R_p/R_s = \tan \Psi \exp(i\Delta) \tag{1}$$

where R_p and R_s are the complex reflection coefficients of the light polarized parallel and perpendicular to the plane of incidence, respectively. The spectral dependencies of ellipsometric parameters Ψ (azimuth) and Δ (phase change) can be fitted with appropriate models to extract film thickness and the optical constants, i.e., the refractive index (n) and extinction coefficient (k), based on the best fit between experimental and simulated spectra.[59,60] In the present case, the Levenberg-Marquardt regression algorithm was used for minimizing the mean-squared error (MSE):[59]

$$\mathrm{MSE} = \frac{1}{2N - M} \sum_{i=1}^{n} \left[\left\{ \frac{(\Psi_{exp} - \Psi_{calc})}{\sigma_{\Psi i}^{exp}} \right\}^2 + \left\{ \frac{(\Delta_{exp} - \Delta_{calc})}{\sigma_{\Delta i}^{exp}} \right\}^2 \right] \tag{2}$$

where Ψ_{exp}, Ψ_{calc} and Δ_{exp}, Δ_{calc} are the measured (experimental) and calculated ellipsometry functions, N is the number of measured Ψ, Δ pairs, M is the number of fitted parameters in the optical model, and σ are standard deviations of the experimental data points.

Extracting meaningful physical information from ellipsometry requires the construction of an optical model of the sample which generally accounts a number of distinct layers with individual optical dispersions. Interfaces between these layers are optical boundaries at which light is refracted and reflected according to the Fresnel relations. The stack model used to simulate the spectra purpose of determining the optical constants of Ti-doped WO_3 films is schematically shown in Figure 1. The model contains, from top, Ti-doped WO_3 film, SiO_2 interface, and Si substrate. The surface and interface roughness were also considered in order to accurately fit the

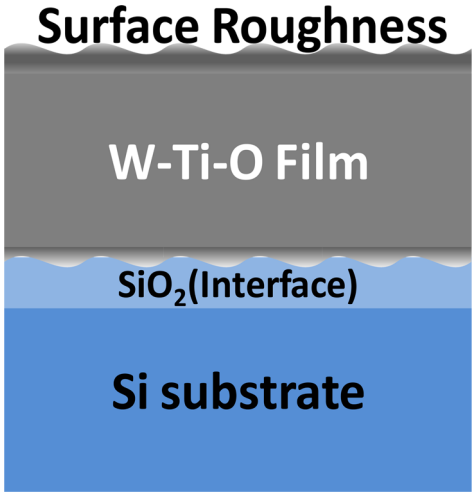

Figure 1. Stack model of the sample constructed for ellipsometry data analysis.

experimental data. The Tauc–Lorentz (TL) model was used and empirical parametrization is based on the Tauc expression for the imaginary part (ε_2) of the dielectric function.[45] For a single transition, the complex dielectric function ε_2 is defined as[59]

$$\varepsilon_2(E) = \left[\frac{A_L E_0 C(E - E_g)^2}{(E^2 - E_o{}^2)^2 + C^2E^2} \cdot \frac{1}{E}\right] \quad (3)$$

where E_0 is the resonance energy, E_g represents band gap energy, E photon energy, and A_L and C are the amplitude and broadening coefficient of the ε_2 peak, respectively, The aforementioned model allowed for the determination of the optical constants, n and k, as well as thickness verification. Note that the real and imaginary parts of the dielectric function are related to n and k as $\varepsilon_1 = n^2 - k^2$; $\varepsilon_2 = 2nk$.

IV. RESULTS AND DISCUSSION

The scanning electron microscopy (SEM) images of W–Ti–O films grown at various T_s are shown in Figure 2. The SEM images did not reveal the presence of any crystalline particles. The SEM cross-sectional images of the representative W–Ti–O films are shown in Figure 3. Images shown are obtained for W–Ti–O films grown at 400 and 500 °C in upper and upper panels, respectively. The Si-substrate and W–Ti–O film regions are as indicated in the micrographs. Two important observations that can be made from these micrographs are the following. No evidence of significant reaction with the Si-substrate at the interface for W–Ti–O samples grown at T_s = RT – 500 °C is the first. This observation indicates that the W–Ti–O films are stable with the Si substrate within the given set of conditions employed in this work. The later is the film thickness, which can be compared and can be used to validate the data obtained from SE modeling as discussed later in this section.

The crystal structure of the grown films was examined by grazing incidence X-ray diffraction (GIXRD) analyses. The GIXRD patterns of W–Ti–O films grown at various T_s are shown in Figure 4. With the absence of diffraction peaks in GIXRD patterns and no evidence of even nanoparticles in the high-resolution SEM images (Figure 2), it can concluded that the films are completely amorphous. The effect may be due to

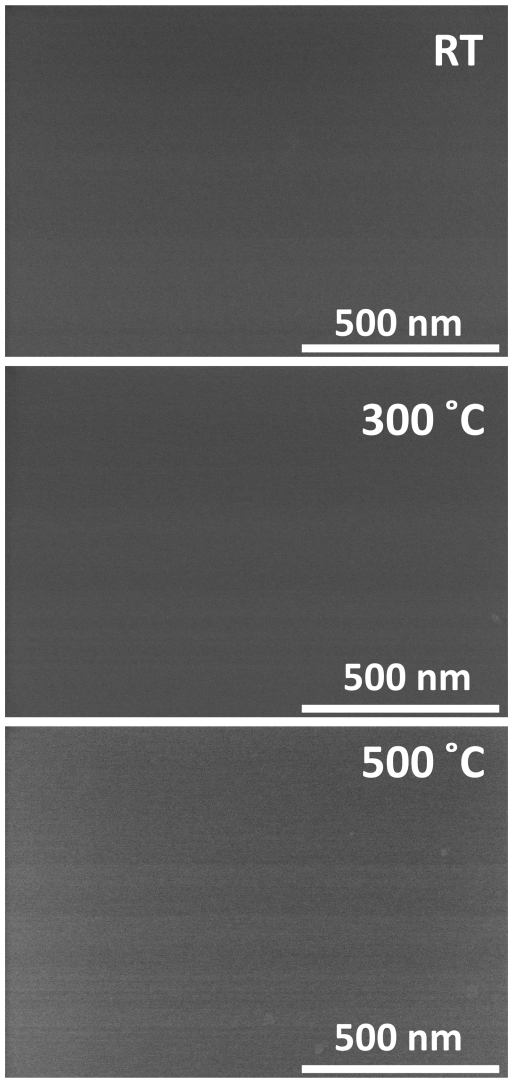

Figure 2. SEM images of W–Ti–O films grown at various temperatures. The images confirm the absence of any particles or crystallites indicating the amorphous nature of the films.

higher concentration of Ti. Our earlier efforts indicated that the pure WO_3 films crystallize in monoclinic structure at T_s = 100–200 °C and tetragonal structure above T_s = 300 °C.[56] Therefore, the result obtained in the present work indicates that the doping of Ti into WO_3 prevents the crystallization and thus induces the amorphous nature. The chemical analyses (not shown) indicate that the effective incorporation of Ti in the films is slightly lower than that of the target. Instead of 80:20 ratio of W/Ti = 80:20 in the bulk of the target, W/Ti ≈ 80:15 was found in the films. The relative difference in the sputtering rates of the elements under the sputtering and reactive gas pressure can account for the observed variation.

Having established the amorphous nature of the grown W–Ti–O films, the attention is now to demonstrate their transparent nature. The optical transmittance spectra of W–Ti–O films are shown in Figure 5. The differences in the spectral transmission curves is due to interference in W–Ti–O films. The spectral transmission curves reveal that the W–Ti–O films in general show a high transparency in the spectral region except where the incident radiation is absorbed across the band gap (E_g). This observation indicates the high-quality and transparent nature of W–Ti–O films. No evident

dx.doi.org/10.1021/am4006258 | ACS Appl. Mater. Interfaces 2013, 5, 4659–4666

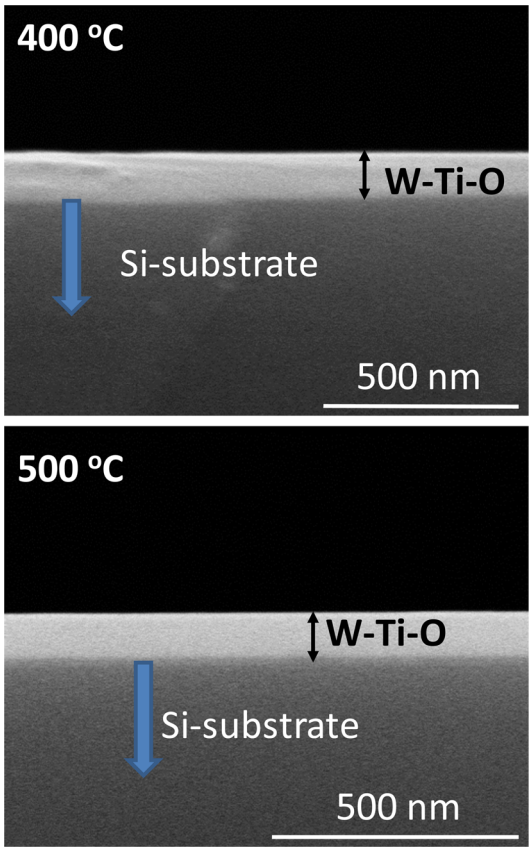

Figure 3. Cross-sectional SEM images of representative W−Ti−O films. The images shown in the upper and lower panel are samples grown at 400 and 500 °C, respectively. The film and substrate regions are as indicated.

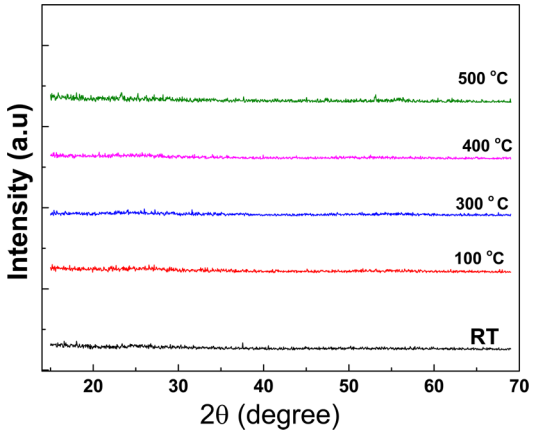

Figure 4. GIXRD patterns of W−Ti−O films grown at various temperatures. The patterns confirm the absence of any diffraction peaks indicating the characteristic amorphous nature of the films grown at all temperatures.

absorption edge shift is noted for W−Ti−O films indicating that there is no significant change in the band gap of the materials fabricated. Optical absorption coefficient and band gap of the W−Ti−O films can be obtained from the spectra shown in Figure 5. The optical absorption coefficient, α, of the films is evaluated using the relation:[56,63,64]

$$\alpha = [1/t] \ln[T/(1 - R)^2] \quad (4)$$

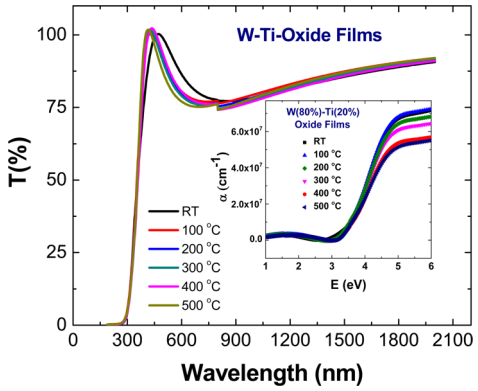

Figure 5. Spectral transmittance characteristics of W−Ti−O films as a function of T_s. Inset shows the optical absorption coefficient of W−Ti−O films.

where T is the transmittance, R the reflectance, and t the film thickness. The average film thickness values determined from both SEM and SE data were employed to obtain the optical absorption coefficient of W−Ti−O films. Also, for transparent films, the R^2 values are extremely small and can be safely neglected to obtain α values. The inset of Figure 5 shows the variation of the optical absorption coefficient of W−Ti−O films grown at various T_s. It is well-known that the optical absorption below E_g follows an exponential behavior.[1,5,56] The absorption, therefore, is exponentially dependent on the energy ($h\nu$) of incident photon in that region. For WO_3, in the E_g region (high absorption) or above the fundamental absorption edge, the absorption follows a power law of the form:[1,5,56,64]

$$(\alpha h\nu) = B(h\nu - E_g)^2 \quad (5)$$

where $h\nu$ is the energy of the incident photon, α the absorption coefficient, B the absorption edge width parameter, and E_g the band gap. Since the Ti is a dopant and the host-matrix is mainly WO_3, the same analysis has been carried out for the optical data of W−Ti−O films. The absorption data and the plots obtained for W−Ti−O films are shown in Figure 6. It is evident that $(\alpha h\nu)^{1/2}$ vs $h\nu$ results in linear plots in the high absorption region suggesting indirect allowed transitions across E_g of W−Ti−O films. Regression analysis and extrapolating the linear region of the plot to $h\nu = 0$ provide the band gap value as indicated with an arrow in Figure 6. The E_g obtained for W−Ti−O films is ~3.1 (±0.05) eV, which is almost constant for all

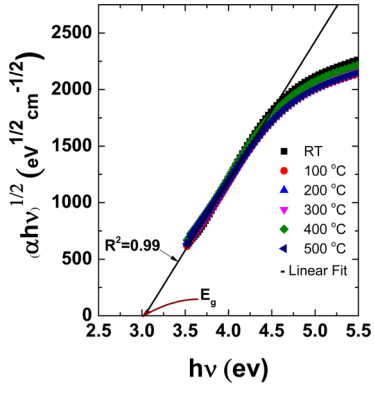

Figure 6. $(\alpha h\nu)^{1/2}$ vs $h\nu$ plots for amorphous W−Ti−O films grown at various substrate temperatures. Extrapolating the linear region of the plot to $h\nu = 0$ provide the band gap value as indicated with an arrow.

the films. While no effect of T_s on the band gap can be due to the fact all the W−Ti−O films are amorphous, the band gap energy agrees well with that reported for sputter-deposited amorphous WO_3 films.[56]

Finally, we now consider the optical constants of Ti-doped WO_3 films probed by SE. The spectral dependencies of the ellipsometric parameters, Ψ and Δ, determined for Ti-doped WO_3 films grown at various temperatures are shown in Figure 7. The spectral dependencies of ellipsometric parameters Ψ

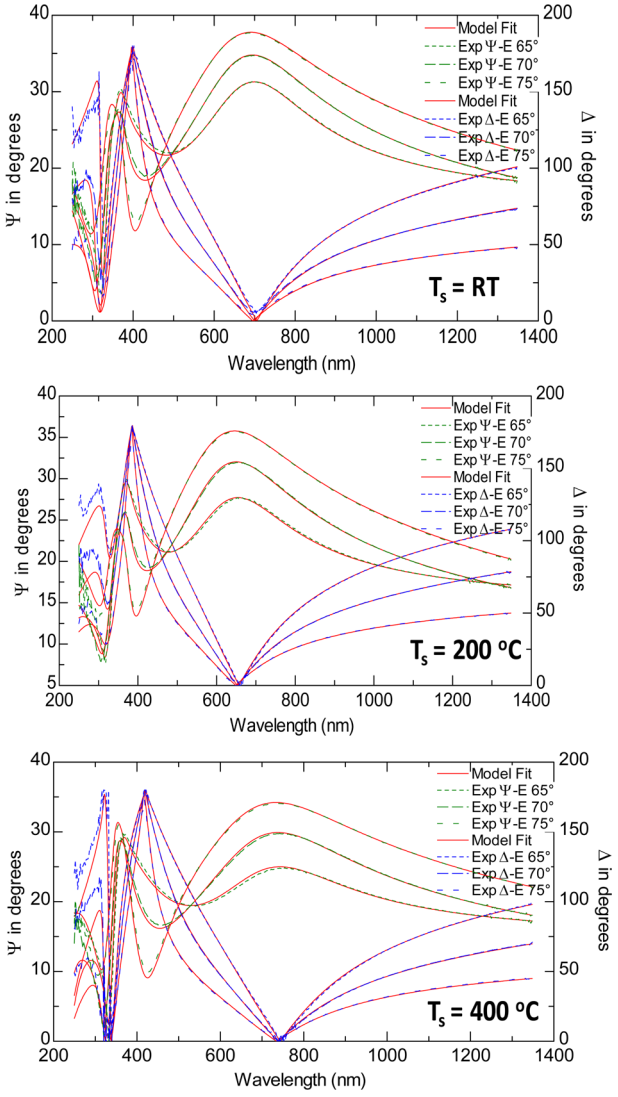

Figure 7. Spectral dependence of Ψ and Δ for Ti-doped WO_3 films grown at various temperatures. The experimental data obtained and modeling curves are shown.

(azimuth) and Δ (phase change) are fitted with appropriate models (discussed in section III) to extract film thickness and the optical constants, i.e., the refractive index (n) and extinction coefficient (k), based on the best fit between experimental and simulated spectra.[59,60] The curves obtained for Ti-doped WO_3 films indicate (Figure 7) a reasonable agreement between the experimental and simulation data.

Considering the optical model (stack model shown in Figure 1), the set of W−Ti−O films were modeled with Tauc−Lorentz (TL) oscillators. Furthermore, the pole magnitude, the E_1 (ε_1) offset constant, and the thickness of the film were fitted, as well as the parameters associated with the individual oscillators employed, simultaneously while attempting to locate the best fit for the data by minimizing the MSE. The modeling parameters are listed in Table 1. The governing oscillator of the genosc layer, the TL oscillator has 4 unique parameters associated with it and they are the amplitude (A_L) of the ε_2 peak, the half width (C) of the ε_2 peak, fixed center energy (E_0) of the TL peak, and the Tauc gap (E_g) of amorphous materials. This particular model employed for the set of titanium doped WO_3 amorphous films has been proven effective, in the literature, to model reasonably transparent conducting oxides.[60,65−67] Furthermore, it should be noted that the E_g values obtained from SE analysis and documented in Table 1 are in excellent agreement with that obtained from the analysis of spectrophotometry data for transparent, amorphous W−Ti−O films.

The microstructure information, specifically, film thickness and interfacial oxide thickness of Ti-doped WO_3 films were also determined from SE analysis. The variation of film thickness as a function of growth temperature is shown in Figure 8. It is evident that the film thickness is more or less constant with increasing growth temperature. Most important is that the interfacial oxide (SiO_2) is limited to 2−3 nm at the interface. This result was consistent with our earlier reports for pure WO_3 films, where there was no significant interfacial oxide growth.[68] Inset of Figure 8 shows the variation of surface roughness of the Ti-doped WO_3 films determined from SE analysis. The roughness as determined from SE analysis is very low (<1 nm) for films grown at temperatures 25−100 °C and are not included. To validate the SE analysis and microstructure, the film thickness values obtained from cross-sectional SEM values are also plotted in Figure 8. It can be seen that the film thickness obtained from SE and X-SEM are in good agreement with each other for all the amorphous W−Ti−O films. This observation indicates that the model(s) and SE analysis adopted can reasonably simulate the microstructure and, hence, optical properties of the sputter-deposited W−Ti−O amorphous films.

The spectral dependence of the extinction coefficient (k) determined from SE data for Ti-doped WO_3 films is shown in Figure 9. It is evident that the extinction coefficient values are low and very close to zero in most parts of the spectrum (Figure 9) which indicates very low optical losses due to absorption. The onset or sharp increase in k at short wavelengths is due to the fundamental absorption across the band gap. An understanding of the structural quality of Ti-doped WO_3 films can also be derived from the dispersion profiles of $k(\lambda)$. Specifically, the curves (Figure 8) indicate that the k value of the Ti-doped WO_3 films is almost zero in the visible and near-infrared spectral regions, while for photon energies toward the ultraviolet region, the extinction coefficient increases sharply. The $k(\lambda)$ behavior is obviously related to the optical quality of the films. Strong absorption with no weak shoulders or tailing behavior for the Ti-doped WO_3 films can be attributed to the high quality of the grown layers with a very high transparency, which is also confirmed by the spectrophotometry analysis of films shown above (Figure 5).

The dispersion profiles of index of refraction (n) determined from SE data for Ti-doped WO_3 films are shown in Figure 10. The results indicate a similar behavior as noted in k curves. The "n" dispersion curves also indicate a sharp increase at shorter wavelengths corresponding to fundamental absorption of energy across the band gap. However, the effect of growth

Table 1. Ellipsometry Modelling Parameters of W−Ti−O Films

temperature (°C)	RT	200	300	400	500
			Modeling Parameters		
Pole Mag.	8.7786 ± 8.8	481.04 ± 49	525.03 ± 26.2	997.15 ± 152	8.948 ± 10.2
E_1 offset	2.0605 ± 0.0994	−0.92686 ± 0.364	−1.1766 ± 0.188	−4.804 ± 2.89	3.151 ± 29.8
Oscillator 1	Tauc−Lorentz	Tauc−Lorentz	Tauc−Lorentz	Tauc−Lorentz	Tauc−Lorentz
A_L	166.02 ± 8.31	115.67 ± 6.9	114.05 ± 4.15	78.854 ± 4.49	137.49 ± 15.6
E_0	4.0422 ± 0.0139	4.0373 ± 0.0139	4.0422 ± 0.0139	4.0237 ± 0.0165	3.9421 ± 0.0332
C	2.3934 ± 0.109	1.368 ± 0.0417	1.368 ± 0.417	1.0462 ± 0.0439	1.297 ± 0.125
E_g	3.2439 ± 0.00865	3.1687 ± 0.0851	3.1687 ± 0.0085	3.142 ± 0.0168	3.2127 ± 0.0166

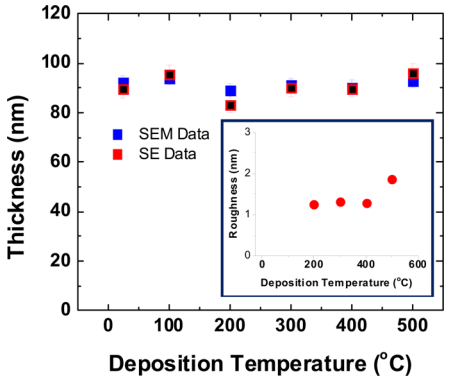

Figure 8. Thickness of Ti-doped WO_3 films grown at various temperatures. Insert shows the variation of surface roughness of the films with growth temperature.

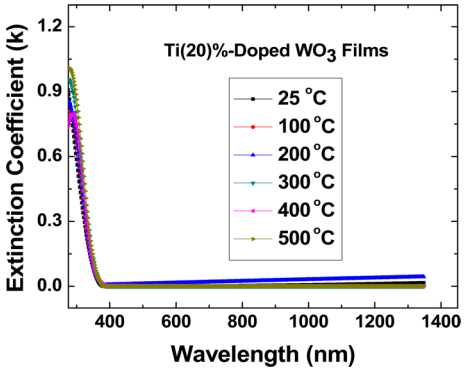

Figure 9. $k(\lambda)$ curves of Ti(20%)-doped WO_3 films grown at various temperatures. The extremely low values of k at λ > 400 nm can be attributed to the transparent nature.

temperature is evident in the dispersion curves (Figure 10), where there is an increase in "n" values with increasing temperature.

In order to understand the chemistry and physics of Ti-doped WO_3 films and the effect of growth temperature on their optical constants, the refractive index variation of the films at λ = 550 nm with growth temperature is shown in the inset of Figure 10. The "n" values of the bulk WO_3 and TiO_2 are as indicated in Figure 10. At a λ = 550 nm, the "n" values increase from 2.17 to 2.31 with increasing growth temperature from 25 to 500 °C. For comparison, at 550 nm, the "n" values of bulk, crystalline WO_3[1,69] and TiO_2[70] are 2.2 and 2.5, respectively. It can be seen (inset, Figure 10) that the data fits a linear dependence on growth temperature indicating the effect of temperature in enhancing the refractive index of Ti-doped WO_3 films. However, it appears that the index of refraction of

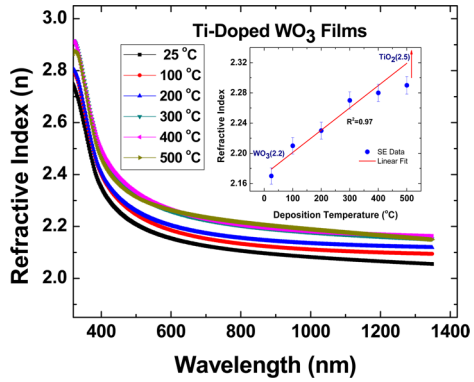

Figure 10. Dispersion profiles of index refraction of Ti(20%)-doped WO_3 films grown at various temperatures. The sharp increase in the index of refraction at $\lambda \leq$ 400 nm is due to fundamental absorption across the band gap of the films. Inset shows the functional dependence of index of refraction measured at λ = 550 nm on the growth temperature of Ti(20%)-doped WO_3 films. The data is compared with that of pure WO_3 and TiO_2. A gradual increase in index of refraction suggests improved packing density of the films with increasing growth temperature.

amorphous W−Ti−O films grown in the temperature range of 400−500 °C is saturated as it is almost constant with a nominal increase. This is evident in both the dispersion curves and the specific "n" values at λ = 550 nm. Further improvement or changes may be possible only if the film is fully crystallized or if a structural transformation occurs.

A simple model can be formulated to explain the observed functional relationship between the optical constants and growth conditions in Ti-doped WO_3 films. Evident from the results, the dispersion of optical constants depend on the growth temperature. XRD measurements demonstrated that the Ti-doped WO_3 films grown at 25−500 °C are completely amorphous. The observed increase in n values when Ti-doped WO_3 films are grown at higher temperatures can be attributed to the improved packing density of the films. However, we believe that the packing density slightly improves but not significantly. Perhaps, the temperature is not enough to promote the structural order but is sufficient to increase the mobility of ad-atoms to join together to increase the packing density of the materials in the films leading to observed increase in "n" values. In order to confirm the validity of this, the relative density (which is the ratio of film density to that bulk of the material) Ti-doped WO_3 films can be approximated from the Lorentz−Lorentz relation[71] using the measured index of refraction values. The functional dependence of the relative density of Ti-doped WO_3 films on the growth temperature is shown in Figure 11. It can be seen that there is a direct

dx.doi.org/10.1021/am4006258 | ACS Appl. Mater. Interfaces 2013, 5, 4659−4666

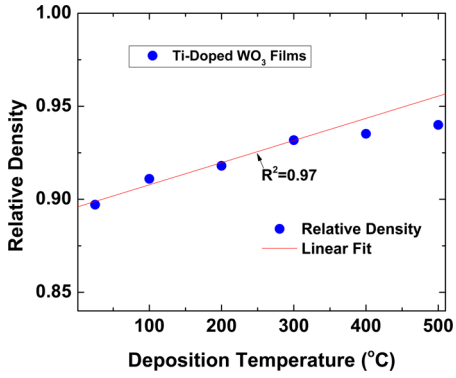

Figure 11. Functional dependence of relative density of the Ti(20%)-doped WO_3 films on the growth temperature. The relative density values were calculated from the Lorentz−Lorentz model.

correlation between the index of refraction, relative density, and growth temperature suggesting that the improved packing density accounts for the observed optical constants and their behavior in Ti-doped WO_3 films.

V. CONCLUSIONS

Ti-doped WO_3 films were fabricated using sputter-deposition by varying deposition temperature in the range of 25−500 °C. The structure and optical properties of the grown W−Ti−O films were evaluated as a function of growth temperature. Crystal structure and surface morphology analyses using GIXRD and SEM, respectively, confirm that Ti-doped WO_3 films were amorphous at all growth temperatures. The effect Ti-incorporation and associated amorphization is dominant in the entire range (25−500 °C) of growth temperatures. Spectrophotometry analyses indicate that grown W−Ti−O films are transparent in nature. Optical constants and a correlation between growth temperature and optical property of the grown films were evaluated using spectroscopic ellipsometry. The stack model containing, from top, Ti-doped WO_3 film, SiO_2 interface, and Si substrate coupled with the Tauc−Lorentz model, where empirical parametrization is based on the Tauc expression for the imaginary part (ε_2) of the dielectric function, reasonably simulates the microstructure and optical properties of the grown W−Ti−O films. The results indicate that the Ti-doped WO_3 films grown at T_s = 25−500 °C are highly transparent and exhibit low optical losses in the visible and near-infrared regions. A correlation between the energy absorption and associated transitions is noted in spectrophotometry and SE analyses confirming the validity of optical behavior of the W−Ti−O films derived from both methods. While there is no significant improvement in the structural order noted, the SE data indicate that the index of refraction of the samples increases from 2.17 to 2.31 with increasing growth temperature from 25 to 500 °C. The increased packing density in the films with increasing temperature is attributed to the linear trend observed in the index of refraction.

AUTHOR INFORMATION

Corresponding Author

*E-mail: rvchintalapalle@utep.edu.

Notes

The authors declare no competing financial interest.

ACKNOWLEDGMENTS

This work is supported by the National Science Foundation (NSF) with NSF-PREM Grant No. DMR-1205302. The Hitachi 4800 SEM used for the morphology and X-ray chemical analysis of the samples in this work was acquired through the support from NSF (Grant NSF-DMR-0521650).

REFERENCES

(1) Granqvist, C. G. *Handbook of Inorganic Electrochromic Materials*; Elsevier: New York, 1995; pp 5−7.
(2) Zhang, Y.; Lee, S. H.; Mascarenha, A.; Deb, S. K. *Appl. Phys. Lett.* **2008**, *93*, 203508−203508-2.
(3) Ramana, C. V.; Utsunomiya, S.; Ewing, R. C.; Julien, C. M.; Becker, U. *J. Phys. Chem. B* **2006**, *110*, 10430−10435.
(4) Berggren, L.; Jonsson, J. C.; Niklasson, G. A. *J. Appl. Phys.* **2007**, *102*, 083538−083538−7.
(5) Lin, Y. S.; Chen, H. T.; Lai, J. Y. *Thin Solid Films* **2009**, *518*, 1377−1381.
(6) Lu, D.; Chen, J.; Chen, H. J.; Gong, J.; Deng, S. Z.; Xu, N. S.; Liu, Y. L. *Appl. Phys. Lett.* **2007**, *90*, 041919−041919-3.
(7) Lee, D. S.; Han, S. D.; Lee, D. D. *Sens. Actuators, B* **1999**, *60*, 57−63.
(8) Baeck, S. H.; Jaramillo, T.; Stucky, G. D.; McFarland, E. W. *Nano Lett.* **2002**, *2*, 831−834.
(9) Lee, D. S.; Nam, K. H.; Lee, D. D. *Thin Solid Films* **2000**, *375*, 142−146.
(10) Wang, L.; Teleki, S. E.; Pratsinis, S. E.; Gouma, P. I. *Chem. Mater.* **2008**, *20*, 4794−4796.
(11) Kawasaki, H.; Namba, J.; Iwatsuji, K.; Suda, Y.; Wada, K.; Ebihara, K.; Ohshima. *Appl. Surf. Sci.* **2002**, *197−198*, 547−551.
(12) Ionescu, R.; Llobet, E.; Brezmes, J.; Vilanova, X.; Correig, X. *Sens. Actuators, B* **2003**, *95*, 177−182.
(13) Moulzolf, S. C.; Ding, S.; Lad, R. J. *Sens. Actuators, B* **2001**, *77*, 375−382.
(14) Satnkova, M.; Vilanova, X.; Llobet, E.; Calderer, J.; Bittencourt, C.; Pireaux, J. J.; Correig, X. *Sens. Actuators, B* **2005**, *105*, 271−277.
(15) Xie, G.; Yu, J.; Chen, X.; Jiang, Y. *Sens. Actuators, B* **2007**, *123*, 909−914.
(16) Santucci, S.; Cantalini, C.; Crivellari, M.; Lozzi, L.; Ottaviano, L.; Passacantanso, M. J. *J. Vac. Sci. Technol. A* **2000**, *18*, 1077−1082.
(17) Gouma, P. I.; Kalyanasundaram, K. *Appl. Phys. Lett.* **2008**, *93*, 244102−244102-3.
(18) Huelser, T. P.; Lorke, A.; Ifeacho, P.; Wiggers, H.; Schulz, C. J. *J. Appl. Phys.* **2007**, *102*, 124305−124305−7.
(19) Marsen, B.; Miller, E. L.; Paluselli, D.; Rocheleau, R. E. *Int. J. Hydrogen Energy* **2008**, *32*, 3110−3115.
(20) Paluselli, D.; Marsen, B.; Miller, E. L.; Rocheleau, R. E. *Electrochem. Solid-State Lett.* **2005**, *8*, G301−G303.
(21) Sun, Y.; Murphy, C. J.; Reyes-Gil, K. R.; Reyes-Garcia, E. A.; Thornton, J. M.; Morris, N. A.; Raftery, D. *Int. J. Hydrogen Energy* **2004**, *34*, 8476−8484.
(22) Zheng, H.; Tachibana, Y.; Kalantar-Zadeh, K. *Langmuir* **2010**, *26*, 19148−19152.
(23) Zheng, H.; Ou, J. Z.; Strano, M. S.; Kaner, R. B.; Mitchell, A.; Kalantar-Zadeh, K. *Adv. Funct. Mater.* **2011**, *21*, 2175−2196.
(24) Ou, J. Z.; Balendhran, S.; Field, M. R.; McCulloch, D. G.; Zoolfakar, A. S.; Rani, R. A.; Zhuiykov, S.; O'Mullane, A. P.; Kalantar-Zadeh, K. *Nanoscale* **2012**, *4*, 5980−5988.
(25) Waller, M. R.; Townsend, K. T.; Zhao, J.; Sabio, E. M.; Chamousis, R. L.; Browning, N. D.; Osterloh, F. E. *Chem. Mater.* **2012**, *24*, 698−704.
(26) Wang, S. J.; Lu, W. J.; Cheng, G.; Cheng, K.; Jiang, X. H. *Appl. Phys. Lett.* **2009**, *94*, 263106−263106-3.
(27) Ha, J. H.; Muralidharan, P.; Kim, D. K. *J. Alloys Compd.* **2009**, *475*, 446−451.
(28) Zhang, J.; Tu, J.; Xia, X.; Wang, X.; Gu, C. *J. Mater. Chem.* **2011**, *21*, 5492−5498.

(29) Jiao, Z.; Sun, X. W.; Wang, J.; Ke, L.; Demir, H. V. *J. Phys. D: Appl. Phys.* **2010**, *43*, 285501−285501-6.
(30) Wang, J.; Khoo, E.; Lee, P. S.; Ma, J. *J. Phys. Chem.* **2008**, *112*, 14306−14312.
(31) Ma, D.; Shi, G.; Wang, H.; Zhang, Q.; Li, Y. *J. Mater. Chem. A* **2013**, *1*, 684−691.
(32) Phuruangrat, A.; Ham, D. J.; Hong, S. J.; Thongtem, S.; Lee, J. S. *J. Mater. Chem.* **2010**, *20*, 1683−1690.
(33) Su, J.; Feng, X.; Sloppy, J. D.; Guo, L.; Grimes, C. A. *Nano Lett.* **2011**, *11*, 203−208.
(34) Li, L.; Zhang, Y.; Fang, X.; Zhai, T.; Liao, M.; Sun, X.; Koide, Y.; Bando, Y.; Golberg, D. *J. Mater. Chem.* **2011**, *21*, 6525−6530.
(35) Lai, C. W.; Sreekantan, S. *Int. J. Hydrogen Energy* **2013**, *38*, 2156−2166.
(36) Kwong, W. L.; Savvides, N.; Sorrell, C. C. *Electrochim. Acta* **2012**, *75*, 371−380.
(37) Vidyarthi, V. S.; Hofmann, M.; Savan, A.; Sliozberg, K.; Konig, D.; Beranek, R.; Schuhmann, W.; Ludwig, A. *Int. J. Hydrogen Energy* **2011**, *36*, 4724−4731.
(38) Santato, C.; Odziemkowski, M.; Ulmann, M.; Augustynski, J. *J. Am. Chem. Soc.* **2001**, *123*, 10639−10649.
(39) Kirchgeorg, R.; Berger, S.; Schmuki, P. *Chem. Commun.* **2011**, *47*, 1000−1002.
(40) Chen, H. J.; Xu, N. S.; Deng, S. Z.; Lu, D. Y.; Li, Z. L.; Zhou, J.; Chen, J. *Nanotechnology* **2007**, *18*, 205701.
(41) Jerman, M.; Mergel, D. *Thin Solid Films* **2007**, *515*, 6904−6908.
(42) Jerman, M.; Qiao, Z.; Mergel, D. *Appl. Opt.* **2005**, *44*, 3006−3012.
(43) Mergel, D. *Thin Solid Films* **2001**, *397*, 216−222.
(44) Mahanthi, M.; Ghosh, T.; Basak, D. *Nanoscale* **2011**, *3*, 4427−4433.
(45) Xieo, M. W.; Wang, L. S.; Huang, X. J.; Wu, Y. D.; Dang, Z. *J. Alloys Compd.* **2009**, *470*, 486−491.
(46) Hong Pan, J.; Lee, W. I. *Chem. Mater.* **2006**, *18*, 847−853.
(47) Keller, V.; Bernhardt, P.; Garin, F. *J. Catal.* **2003**, *215*, 129−138.
(48) Kobayashi, M.; Miyoshi, K. *Appl. Catal., B* **2007**, *72*, 253−261.
(49) Higashimoto, S.; Sakiyama, M.; Azuma, M. *Thin Solid Films* **2006**, *503*, 201−206.
(50) Smith, W.; Zhao, Y. *J. Phys. Chem. C* **2008**, *112*, 19635−19641.
(51) Smith, W.; Wolcott, A.; Fitzmorris, R. C.; Zhang, J. Z.; Zhao, Y. *J. Mater. Chem.* **2011**, *21*, 10792−10800.
(52) Ferroni, M.; Boscarino, D.; Comini, E.; Gnani, D.; Guidi, V.; Martinelli, G.; Nelli, P.; Rigato, V.; Sberveglieri, G. *Sens. Actuators, B* **1999**, *58*, 289−294.
(53) Gerlich, M.; Kornely, S.; Fleischer, M.; Mixner, H.; Kassing, R. *Sens. Actuators, B* **2003**, *93*, 503−508.
(54) Kalidindi, N. R.; Manciu, F. S.; Ramana, C. V. *ACS Appl. Mater. Interfaces* **2011**, *3*, 863−868.
(55) Kalidindi, N. R.; Kamala Bharathi, K.; Ramana, C. V. *Appl. Phys. Lett.* **2010**, *97*, 142107−142107-3.
(56) Gullapalli, S. K.; Vemuri, R. S.; Ramana, C. V. *Appl. Phys. Lett.* **2010**, *96*, 171903−171903-3.
(57) Vemuri, R. S.; Kamala Bharathi, K.; Gullapalli, S. K.; Ramana, C. V. *ACS Appl. Mater. Interfaces* **2010**, *2*, 2623−2628.
(58) *Guide to Using WVASE32 Spectroscopic Ellipsomtry Data Acquisition and Analysis Software*; J. A. Woollam Co., Inc.: Lincoln, NE, 2008.
(59) Jellison, G. E., Jr. *Thin Solid Films* **1996**, *290−291*, 40−45.
(60) Fujiwara, H. *Spectroscopic Ellipsometry: Principles and Applications*; John Wiley & Sons Inc.: Chichester, U.K., 2007; pp147−265.
(61) Ramana, C. V.; Utsunomiya, S.; Ewing, R. C.; Becker, U.; Atuchin, V. V.; Aliev, V.Sh.; Kruchinin, V. N. *Appl. Phys. Lett.* **2008**, *92*, 011917−011917-3.
(62) Mudavakkat, V. H.; Atuchin, V. V.; Kruchinin, V. N.; Kayani, A.; Ramana, C. V. *Opt. Mater.* **2012**, *34*, 893−900.
(63) Tyagi, P.; Vedeshwar, A. G. *Phys. Rev. B* **2002**, *66*, 075422.
(64) Vemuri, R. S.; Engelhard, M. H.; Ramana, C. V. *ACS Appl. Mater. Interfaces* **2012**, *4*, 1371−1377.
(65) Tauc, J.; Grigorovici, R.; Vancu, A. *Phys. Status Solidi B* **1966**, *15*, 627−637.
(66) Rovira, P. I.; Collins, R. W. *J. Appl. Phys.* **1999**, *85*, 2015−2015-11.
(67) Fujiwara, H.; Kondo, M. *Phys. Rev. B* **2005**, *71*, 075109−075109−10.
(68) Manciu, F. S.; Enriquez, J. L.; Durrer, W. G.; Yun, Y.; Ramana, C. V.; Gullapalli, S. K. *J. Mater. Res.* **2010**, *25*, 2401−2404.
(69) Hong, K.; Kim, K.; Kim, S.; Lee, I.; Cho, H.; Yoo, S.; Choi, H. W.; Lee, N.-Y.; Tak, Y.-H.; Lee, J.-L. *J. Phys. Chem. C* **2011**, *115*, 3435.
(70) Diebold, U. *Surf. Sci. Rep.* **2003**, *48*, 53−229.
(71) Born, M. and Wolf, E. In *Principles of Optics*, 7th ed.; Cambridge University Press: Cambridge, U.K., 1999; p98.

J Mater Sci (2012) 47:6593–6600
DOI 10.1007/s10853-012-6591-z

Comparative microscopic and spectroscopic analysis of temperature-dependent growth of WO_3 and $W_{0.95}Ti_{0.05}O_3$ thin films

Felicia S. Manciu · Young Yun · William G. Durrer · James Howard · Ute Schmidt · Chintalapalle V. Ramana

Received: 8 March 2012 / Accepted: 17 May 2012 / Published online: 30 May 2012

Abstract We present a comparative microscopic and spectroscopic study of the morphology and composition of WO_3 and $W_{0.95}Ti_{0.05}O_3$ thin films, grown by radio-frequency magnetron reactive sputtering at substrate temperatures varied from room temperature to 500 °C, using atomic force microscopy (AFM), Raman spectroscopy, and X-ray photoelectron spectroscopy (XPS). With increasing growth temperature, the AFM results show increase in the average crystallite size and in the surface roughness for both undoped and doped samples. The AFM data, along with the Raman results, clearly indicate that for the given set of experimental conditions, higher growth temperatures are required to obtain crystalline Ti-doped WO_3 films than for WO_3 films. Also, the Raman results suggest a potential phase transformation from a monoclinic WO_3 structure to an orthorhombic, but more probably a tetragonal, configuration in the $W_{0.95}Ti_{0.05}O_3$ thin films. This remark is based on the observed shifting, with Ti doping, to lower frequencies of the Raman peaks corresponding to W–O–W stretching modes of WO_3 at 806 and 711 cm^{-1} to 793 and 690 cm^{-1}, respectively. XPS data indicate that the doped material has a reduced WO_{3-x} stoichiometry at the surface, with the presence of W^{6+} and W^{5+} oxidation states; this observation could also be related to the existence of a different structural phase of this material, corroborating with the Raman measurements.

F. S. Manciu (✉) · Y. Yun · W. G. Durrer · J. Howard
Department of Physics, University of Texas at El Paso, El Paso, TX 79968, USA
e-mail: fsmanciu@utep.edu

U. Schmidt
WITec GmbH, 89081 Ulm, Germany

C. V. Ramana
Department of Mechanical Engineering, University of Texas at El Paso, El Paso, TX 79968, USA

Introduction

Although pure WO_3 is a recognized candidate for gasochromic, electrochromic, and photochromic devices, its morphological characteristics are strongly dependent on the conditions and methods used in its fabrication, as revealed in the literature [1–10]. An improvement in its gasochromic detection sensitivity and in its increased temperature range of operation as a sensor, which for undoped thin films of WO_3 grown by radio-frequency (RF) magnetron sputtering are achieved at a deposition temperature of ~200 °C [9, 10], as well as in its electrochromic and photocatalytic properties, has been achieved by doping with appropriate metals or by addition of metal/metal oxide additives [7–18]. Due to electron transfer from the metal oxide to the added metal on its surface, a decrease in the electron concentration in the metal oxide surface layer occurs. The underlying mechanism, which is especially active at elevated temperature, is as follows: if the metal on the surface is covered with oxygen adsorbates (oxidation of the metal), the oxygen adsorbates will extract electrons from the metal, which in turn will extract electrons from the metal oxide [13, 15]. Thus, the enhancement in the sensitivity of the material will be promoted by the change in the oxidation state of the loaded material. The results of analytical techniques such as X-ray photoelectron spectroscopy (XPS) can make important contributions in confirming these changes when used in conjunction with atomic force microscopy (AFM) and Raman spectroscopy, as will be seen below.

Also, due to TiO_2 structural characteristics such as high-chemical stability and good mechanical properties, when

doped with titanium (Ti) or mixed with TiO_2 nanoparticles, WO_3 exhibits a longer cycle lifetime, shows absorbance at short wavelengths ($\sim$346 nm), and has better photocatalytic activity under visible light than the unsensitized material [12, 16, 17]. Furthermore, doping with a small amount of Ti ($\sim$5 % as in the current work) not only increases the stability of the resultant material, but it also promotes structural phase modifications [12, 18]. As suggested by Depero et al. [18], the distorted phase will contain randomly oriented edged-sharing octahedra as opposed to the characteristic network of corner-sharing octahedra of the WO_3 structure. Edge-sharing octahedra in the newly formed structural phase is preferential since the Ti^{4+} ion, which has a lower oxidation state, substitutes for the W^{6+} ion and decreases the electrostatic repulsion between adjacent cations [12]. The occurrence of the substitutional process in the WO_3 structure instead of Ti occupying interstitial sites, as is typically encountered for doping elements [19], is the reason that no ordered phase of W–Ti–O mixed oxide has yet been reported.

This research places particular emphasis on understanding, from a comparative microscopic and spectroscopic perspective (i.e., using AFM, Raman spectroscopy, and XPS investigations), the changes that might occur in the microstructure of pure and Ti-doped tungsten oxide (WO_3), especially at high temperatures. The outcomes of the current work, together with our previously reported results obtained by scanning electron microscopy (SEM) and X-ray diffraction (XRD) [1–3], provide a detailed and complete characterization of the materials under study and, consequently, of their future potential technical applicability. In addition, since the effect of crystallite size on the physical and chemical properties of solids plays a crucial role in the ongoing quest to improve and optimize material properties, and in view of the fact that there is increased interest in W–Ti–O thin films as new sensing materials, this study demonstrates the value of applying sensitive techniques for observing small structural modifications and for providing useful information on the inherent complexity of Ti-doped WO_3 samples, which have structural properties that are far from being completely clarified in the literature.

The optical and surface spectroscopic measurements that we performed on WO_3 samples made essential contributions to confirming morphological changes for different substrate temperatures, enabling us to optimize the growth conditions [3]. These confocal Raman, infrared absorption, and XPS results indicate structural changes of WO_3 films from an amorphous phase to a monoclinic structure [3]. Since an important question to consider is the degree to which doping can affect the porosity of the WO_3 film structure and/or its chemistry, which can have an influence on the effective surface area and ultimately can determine the number of surface active sites for oxygen adsorption (our previously reported SEM and XRD measurements on the 5 % doped WO_3 [1, 2] revealed explicit structural changes for $W_{0.95}Ti_{0.05}O_3$ thin films), an analysis of these samples at a molecular level could bring additional valuable insights.

Experimental details

WO_3 and $W_{0.95}Ti_{0.05}O_3$ thin films were deposited by RF (13.56 MHz) magnetron sputtering onto sapphire and quartz substrates, respectively, in a reactive O_2–Ar atmosphere. For the growth of the WO_3 set of samples, a W metal target (Plasmaterials, Inc.) of 99.95 % purity and 3″ diameter was employed. The $W_{0.95}Ti_{0.05}O_3$ thin films were obtained using a 2″ diameter custom made W–Ti alloy-target (Plasmaterials Inc.) with a 95.5 at.% weight. The substrates were thoroughly cleaned with isopropyl alcohol and dried with nitrogen before introducing them into the vacuum chamber, which was initially evacuated to a base pressure of $\sim 10^{-6}$ Torr.

In both scenarios, the targets were placed at a distance of 8 cm from the substrate. A sputtering power of 40 W was initially applied to the targets while introducing high-purity argon (Ar) into the chamber to ignite the plasma. Once the plasma was ignited, the power was increased to 100 W, and oxygen (O_2) was released into the chamber for reactive deposition. The sputtering atmosphere consisted of Ar–O_2 mixed gases, and their flow rates were controlled with MKS mass flow meters to provide an optimum Ar:O_2 flow ratio of 1:6 for the deposition of WO_3 samples and a flow ratio of 1:9 for the deposition of $W_{0.95}Ti_{0.05}O_3$ samples. Also, before each deposition, targets were pre-sputtered for 10 min using Ar alone with the shutter above the gun closed. The substrate growth temperature was varied from room temperature (RT) to 500 °C, in increments of 100 °C by heating the substrates with halogen lamps and controlled with an Athena X25 temperature controller.

Atomic force microscopy and Raman measurements were performed in ambient conditions at room temperature with a modular *WITec alpha300 RA* system combining both confocal Raman and AFM. The surface topography of an area of 1×1 μm^2 was measured in AFM AC mode on all studied films. For all AFM experiments, "Arrow Force Modulation" cantilevers purchased from Nanoworld with a nominal spring constant of 2.8 N/m and resonance frequencies in the range of 65–80 kHz were used. For the acquisition of Raman spectra, the *WITec alpha 300 RA* was equipped with a frequency doubled Nd:YAG laser ($\lambda = 532$ nm) and a 100× air objective (NA = 0.9). Each Raman spectrum presented was measured with an acquisition time of 5 s.

The binding energies of the atomic constituents and their chemical oxidation states were evaluated through XPS

measurements, which were performed on sample surfaces using MgK_{α} X-rays in a Perkin-Elmer Phi 560 ESCA/SAM system.

Results and discussion

The AFM topography images shown in Fig. 1a–e were recorded from the WO_3 films prepared at various substrate temperatures. They are presented in a 3D view, all using the same z-scale for easy comparison. They indicate an obvious surface morphology evolution in WO_3 thin films as a function of substrate temperature, especially at higher growth temperatures. The WO_3 film grown at room temperature (Fig. 1a) shows the presence of only very small particles, revealing the amorphous character of this sample. In RF sputtering, the substrate temperature is an important parameter in achieving optimum growth conditions, besides Ar:O_2 ratio, total pressure, and RF power settings [9, 11, 14]. Since all these factors influence the microstructure of the thin films and, consequently, their properties, we experimentally identified them elsewhere [20]. For example, a decrease in the energy of the sputtering species was observed with increasing oxygen pressure, resulting in the growth of thinner films [20]. Furthermore, at low temperatures, because the thermal energy does not give sufficient mobility to the reactive species as they condense on the substrate surface, they may remain stuck to the regions where they land, thus leading to an amorphous film as seen, in this case, for the sample grown at room temperature. Since the species' mobility on the surface increases with increasing temperature, there are slight increases in the sizes of the film surface grains for the WO_3 sample grown at a substrate temperature of 100 °C (Fig. 1b). Small, isolated particles, almost spherical in their shapes, can be seen in the AFM images for WO_3 films grown at 100 and 300 °C (see Fig. 1b, c). These two images show a fine, almost uniform microstructure distribution with an average particle size of 10−14 nm. The increase in the substrate temperature leads to an increase in the particle size (larger than 30 nm) as observed for the sample grown at a substrate temperature of 400 °C. The largest average particle size ($\sim$60 nm) is measured for WO_3 films grown at 500 °C. It can also be seen in Fig. 1d, e that the distribution of particles becomes random at high temperatures ($T > 400$ °C), and the almost spherical morphology noticed for WO_3 films grown at $T \leq 300$ °C also changes with an increase in temperature above 300 °C. Not only an increase in the average particle size with increasing growth temperature is observed, but also the surface roughness is increased. If, for a growth temperature of 25 °C (room temperature), the WO_3 film has a roughness of 4 nm, then at a growth temperature of 500 °C, the roughness becomes 12 nm.

The AFM topography images for $W_{0.95}Ti_{0.05}O_3$ samples, which were grown using temperature conditions identical to those applied to the WO_3 thin films, are presented in Fig. 2a–d. Comparison of these images with previously analyzed WO_3 samples shows that a higher temperature of at least 300 °C is required to obtain a noticeable microstructure for Ti-doped WO_3 films than for WO_3 films. Since no definite grain features can be observed in the AFM image of the sample grown at a substrate temperature of 100 °C (see Fig. 2a), for a lower growth temperature such as RT, there would be an even higher probability for this sample to be amorphous, too. Therefore, we do not present here the RT AFM image. Also, a smaller average size of Ti-doped WO_3 nanoparticles is obtained, at the same high temperatures, than for undoped WO_3 materials, e.g., at a substrate temperature of 500 °C the average size observed in the image of the $W_{0.95}Ti_{0.05}O_3$ sample is $\sim$30 nm as compared to the value of $\sim$60 nm seen for the AFM image of the undoped sample. These observations, which imply a disordering effect induced by the Ti-doping on the microstructure and grain-distribution characteristics of WO_3, are in good agreement with our previously reported SEM results [1, 2].

The Raman results of the $W_{0.95}Ti_{0.05}O_3$ samples, which are presented in Fig. 3, reveal only broadband profiles centered around 267, 690, 793, and 987 cm^{-1}; again an indicator of induced disorder in the structure of these samples. Similar results have been reported in the literature for Ti-doped WO_3 samples that were synthesized by other methods [13–16]. The Raman spectra of Fig. 3 also indicate continuing crystallization with increasing temperature; this remark is based on the faster increase and sharpening of the 267, 690, and 793 cm^{-1} peak intensities, which are associated with the bending and stretching vibrations of WO_6 octahedra [7, 8, 12]. The vibration at 987 cm^{-1} is due to W=O terminal bonds [7, 8, 12].

An example of a suitable fitting of these broad asymmetric bands to the Raman spectrum of the sample grown at the 500 °C substrate temperature is presented in the inset of Fig. 3. The Lorentzian line deconvolution reveals that the inherent asymmetries at the higher and lower frequency sides of the 267 and 690 cm^{-1} peaks, respectively, originate from vibrational bands centered around 404 and 634 cm^{-1}. However, a perfect fitting cannot be obtained with these Lorentzian lines only; there is another distinct scattering contribution between these features that is fitted with a line at 518 cm^{-1}. While the 404 and 518 cm^{-1} bands can be attributed to the presence of noncrystalline TiO_2 in these samples, the 634 cm^{-1} can be assigned to either the confined size of the TiO_2 and/or the orthorhombic WO_3 phase [14, 18, 21].

A more obvious morphological change induced by the Ti cations into the metal oxide structure can be depicted

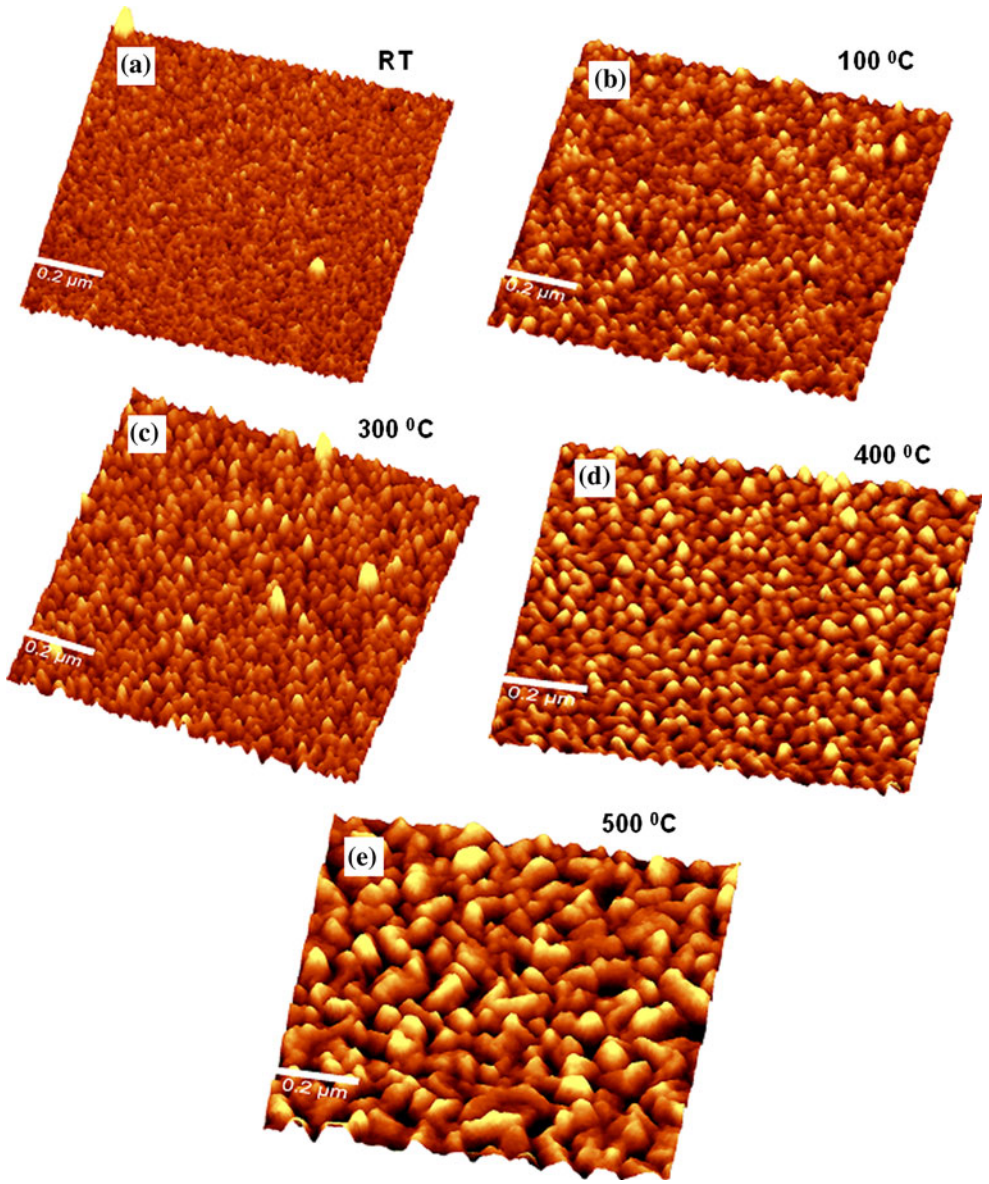

Fig. 1 AFM images of WO_3 thin films grown at different substrate temperatures, as labeled

by direct comparison of the Raman spectra of WO_3 and $W_{0.95}Ti_{0.05}O_3$ samples, a comparison presented in Fig. 4 (with red line spectra corresponding to WO_3 samples and black line spectra corresponding to $W_{0.95}Ti_{0.05}O_3$ samples). These spectra not only demonstrate, for identical substrate growth temperatures, a more rapid crystallization process for WO_3 samples than for Ti-doped WO_3 material (faster increase and sharpening of the Raman vibrational lines in the former material), an observation consistent with the AFM images presented above, but, more importantly, they reveal shifting, to lower frequencies, of the Raman peaks corresponding to W–O–W stretching modes of WO_3 at 806 and 711 cm^{-1} to 793 and 690 cm^{-1}, respectively, for the doped material. These shifts suggest that, with Ti doping, W–O bonds are affected in the new metal oxide structure; they get longer or, in extreme cases they could even break. Furthermore, for samples grown at high temperatures (e.g., at 400 °C in Fig. 4), the intensity of the 987-cm^{-1} feature, which corresponds to W=O bonds, increases in the spectrum of $W_{0.95}Ti_{0.05}O_3$ as compared with that of WO_3. Similar results have been observed before by Hu et al. [16] and have been explained based on the fact that in the newly doped structural network, W–O–W bonds break down to allow the formation of W=O bonds, which, in turn, favor the injection of other ions.

It has also been suggested that, during thermal treatment, Ti plays a relevant role in stabilizing the orthorhombic WO_3 phase [12]. While Sangaletti et al. [14] attributed vibrational lines at 640 and 690 cm^{-1} to the

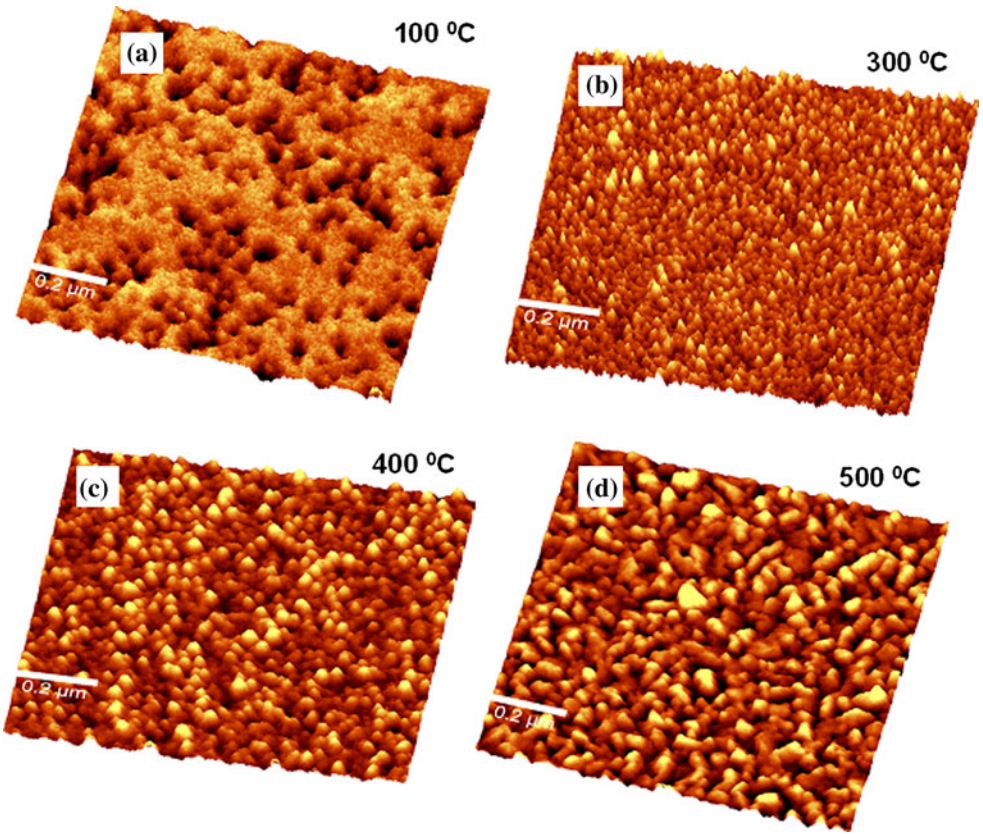

Fig. 2 AFM images of $W_{0.95}Ti_{0.05}O_3$ samples grown at different substrate temperatures, as labeled

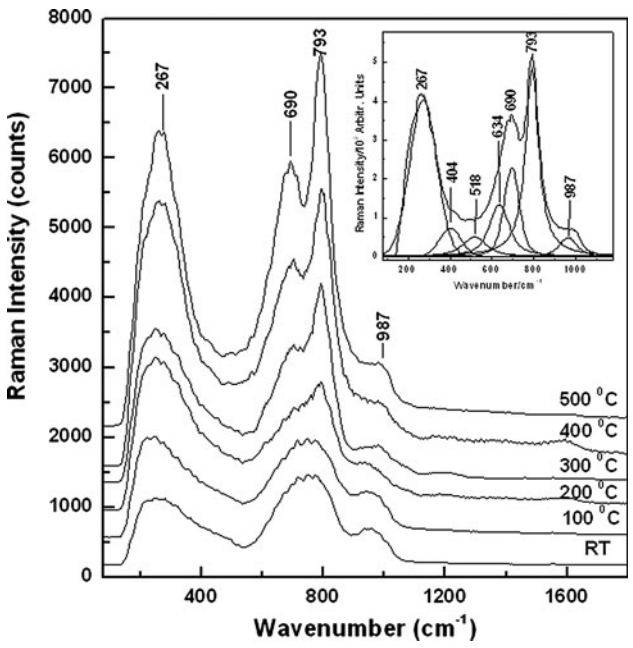

Fig. 3 Raman spectra of Ti-doped WO_3 samples grown at quartz substrate temperatures ranging between RT and 500 °C

orthorhombic WO_3 phase, features near the same frequency region as those observed in our Raman spectra (e.g., 690 and 793 cm^{-1}) have been considered by Boulova and Lucazeau [5] to belong to a tetragonal WO_3 structure. Thus, while the 690 cm^{-1} Raman vibration could be associated with either the orthorhombic or the tetragonal structure, the 640 cm^{-1} feature could correspond to the orthorhombic morphology or to the existence of TiO_2 in our samples, as mentioned above. Therefore, from the Raman perspective, an exact assignment for the new structural configuration of the Ti-doped thin films is controversial: it may be associated with a structural change from monoclinic WO_3 to orthorhombic $W_{0.95}Ti_{0.05}O_3$, or with the existence of tetragonal structure in the $W_{0.95}Ti_{0.05}O_3$ films, or with both. Although the possibility of a phase transition to an orthorhombic morphology is in good agreement with the previously reported literature results, which affirm that for bulk WO_3 a complete transformation is expected for temperatures ranging between 330 and 740 °C, it has also been demonstrated that, with doping, lower temperatures are encountered for phase transitions [12, 14, 16].

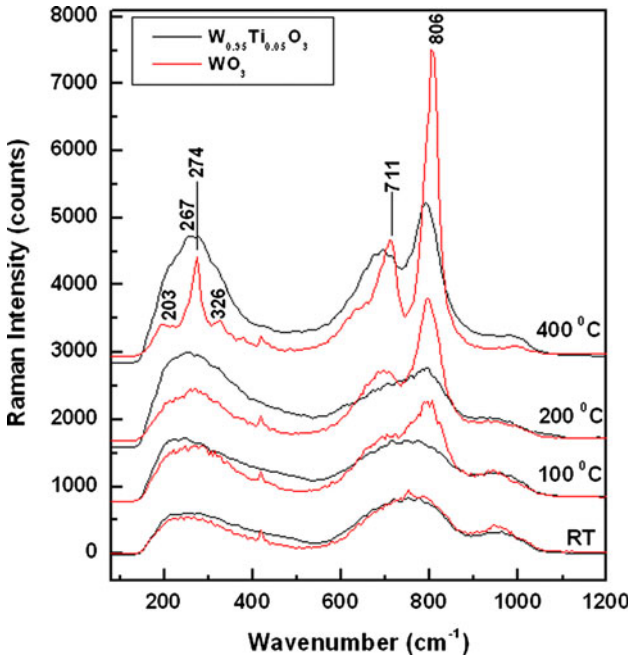

Fig. 4 Comparison of Raman spectra of undoped and Ti-doped WO_3 samples grown at substrate temperatures ranging between RT and 400 °C

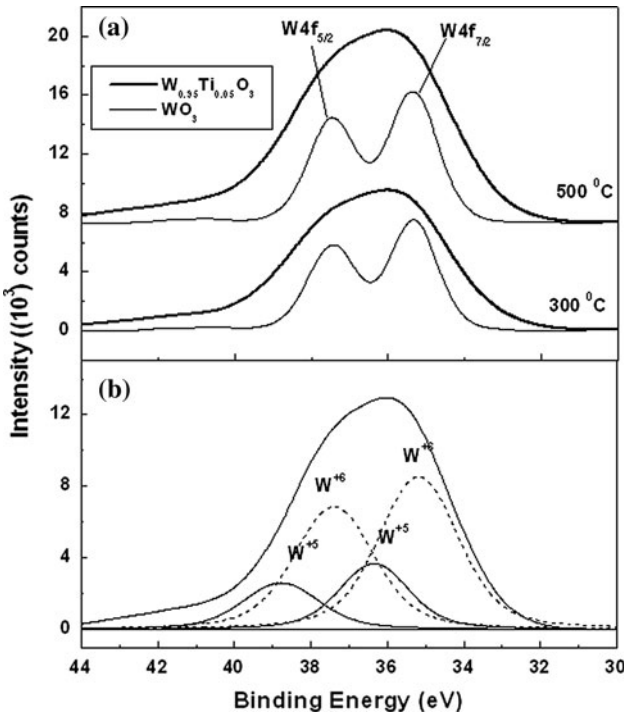

Fig. 5 **a** XPS spectra of W4f peaks for WO_3 and $W_{0.95}Ti_{0.05}O_3$ samples deposited at 300 and 500 °C substrate temperatures, as indicated (the spectra are vertically translated for clarity) and **b** decomposition of XPS spectrum of $W_{0.95}Ti_{0.05}O_3$ sample grown at 500 °C into contributions from W^{6+} and W^{5+}

Furthermore, our previously reported X-ray diffraction results performed on these samples indicate a tetragonal structure for $W_{0.95}Ti_{0.05}O_3$ films grown at temperatures $\geq$300 °C [1, 2]. However, it is worth pointing out that there is still a debate in the literature regarding XRD structural assignments to higher symmetry phases such as the tetragonal one, for doped, as well as for undoped WO_3 materials [14, 18, 22]. One main reason for this difference of opinion is the fact that the strongest diffraction peaks for monoclinic, orthorhombic, and tetragonal structures are very slightly separated, with 2θ values ranging from about 23° to 25°. If thin films versus powder samples are considered, the assignment is even more difficult due to the broadness of the peaks and to the film preferential growth direction. The change seen in our XRD results [1, 2, 20] corroborates the current shifts observed in the Raman peak positions, both suggesting a structural modification of the material with doping.

The XPS survey scans, not presented here, confirm that the main constituent elements of the films were tungsten, oxygen, and titanium atoms. Except for the C peak at 284.6 eV, which was used as an internal standard for calibration of the binding energies and originates from surface adsorbed carbon moieties, there was no other discernable impurity in the samples.

Figure 5a shows the XPS measurements of the W4f level for WO_3 and $W_{0.95}Ti_{0.05}O_3$ samples grown at substrate temperatures of 300 and 500 °C. While the spectra of undoped thin films reveal well-resolved doublet peaks corresponding to $W4f_{5/2}$ and $W4f_{7/2}$, with binding energies at 37.47 and 35.34 eV, respectively, and indicate that the film surface is close in its chemical stoichiometry to that of WO_3 [23], in the spectra of $W_{0.95}Ti_{0.05}O_3$ samples only a very broad peak is observed. The appropriate deconvolution of this peak (Fig. 5b) demonstrates that besides the W^{6+} contribution, there is a second doublet formed with binding energies at 39.48 and 36.85 eV, which is assigned to W^{5+}. Thus, due to the presence of Ti, the doped films have a reduced WO_{3-x} stoichiometry at the surface; an observation that could be related to a change in the structural phase of this material, which is in good agreement with the above Raman measurements.

Comparison of XPS data for O1s for the doped and undoped samples is presented in Fig. 6a. These results reveal, for the WO_3 samples, main O1s peaks at 529.6 eV for the sample grown at a substrate temperature of 300 °C, and at 529.3 eV for the sample grown at a substrate temperature of 500 °C, plus a weak feature at 532.4 eV, which is attributed to surface oxygen contamination. With the temperature varying between RT and 500 °C, there is also a slight shift of about 0.5 eV towards lower binding energies in the position of the O1s feature for WO_3 samples. On the other hand, the spectra of the $W_{0.95}Ti_{0.05}O_3$ samples show a very broad peak with a FWHM of 3.4 eV centered

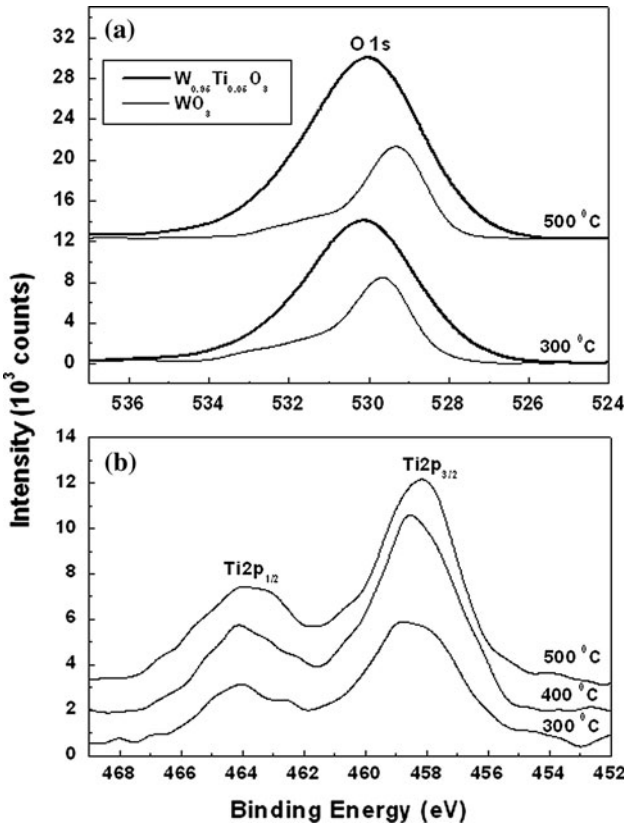

Fig. 6 **a** XPS spectra of O1s peaks for WO_3 and $W_{0.95}Ti_{0.05}O_3$ samples deposited at 300 and 500 °C substrate temperatures. **b** XPS spectra of Ti2p peaks for $W_{0.95}Ti_{0.05}O_3$ samples deposited at 300, 400, and 500 °C substrate temperatures, as indicated. The spectra are vertically translated for clarity

at 530.1 eV. While this binding energy falls between those of the main O1s peaks of the WO_3 samples and that observed in the literature for TiO_2, it is worth pointing out that its position is closer to the one observed for TiO_2 [24]. However, the broadness of this feature suggests the contribution of different oxidation states corresponding to multiple W and Ti environments such as W^{6+}, W^{5+}, and Ti^{4+} (see Figs. 5b, 6b). Figure 6b shows the Ti2p XPS spectra displaying the Ti2p$_{3/2}$ and Ti2p$_{1/2}$ lines at 458.2 and 464.1 eV, respectively, as expected for stoichiometric anatase TiO_2.

Summary and conclusions

Microscopic and spectroscopic investigations of the growth temperature dependence and oxidation states of W and Ti have been carried out on WO_3 and $W_{0.95}Ti_{0.05}O_3$ thin films grown at temperatures varied from RT to 500 °C. Since the purpose of these investigations is to find confirmation, by a comparative approach, that the growth temperature influences the morphology of the material, such as the roughness, the mean grain size of the nanoparticles on the surface layer of undoped and doped WO_3 thin films, and the crystallinity of the material, we pursued microscopic and spectroscopic analysis by AFM, which provides information about the first two issues, and by Raman scattering, which gives information about the crystallinity of the metal oxides. Furthermore, since with doping the oxidation states of the elemental constituents of the WO_3 samples could change, we investigated by XPS these potential changes when Ti(5 %) doping is applied.

Comparison of the AFM and Raman results shows that a higher temperature is required to obtain crystalline microstructure for Ti-doped WO_3 films than for WO_3 films. With increasing growth temperature, the AFM results for WO_3 films show increases in the average grain size from 10 to 14 nm at RT to $\sim$60 nm at 500 °C, and in the surface roughness from 4 nm at RT to about 12 nm at 500 °C. Much smaller average grain sizes are attained for $W_{0.95}Ti_{0.05}O_3$ samples grown at the same high temperatures as the WO_3 material, e.g., at 500 °C, a $\sim$30 nm average grain size is observed for the Ti-doped samples versus the $\sim$60 nm average grain size for pure WO_3 thin films. This remark corroborates with the greater broadness of the Raman bands observed in the spectra of the $W_{0.95}Ti_{0.05}O_3$ material, broadness that could be explained by the formation of smaller crystallites. Also, the shifting, with Ti doping, of the Raman peaks corresponding to W–O–W stretching modes of WO_3 at 806 and 711 cm^{-1}, to 793 and 690 cm^{-1}, respectively, suggests, besides a modification of W–O–W bonds, a potential phase transformation of monoclinic WO_3 to an orthorhombic, but more probably to a tetragonal, configuration in the doped material.

While the XPS measurements of the W4f level for doped material show a reduced WO_{3-x} stoichiometry at the surface, with the presence of W^{6+} and W^{5+} tungsten oxidation states, the O1s XPS data reveal a very broad peak with a FWHM of 3.4 eV and centered at 530.1 eV, which contains the contribution of different oxygen states for the multiple W and Ti environments present. The Ti2p XPS spectra resemble those of stoichiometric anatase with characteristic lines at 458.2 eV (Ti 2p$_{3/2}$) and 464.1 eV (Ti 2p$_{1/2}$). However, it is worth noting that, since in this work the Ti incorporation was performed by RF sputtering using a W–Ti alloy target, the films studied are not only free of additional impurities, as confirmed by XPS analysis, but, they are uniform with no separated WO_3 and TiO_2 crystalline phases present, as revealed by the current Raman investigations.

As high-quality materials with excellent ordered structure and narrower particle-size distributions, which can also withstand high-temperature technological environments such as those encountered in furnaces and coal

gasification systems without their structure being affected by phase transformations, are needed for developing new, more sensitive sensors, the research presented here demonstrates that W–Ti–O thin films grown by RF sputtering could be valuable candidates. The observed favorable crystallite size distribution with characteristics of higher structural symmetry (e.g., possible tetragonal morphology) for the samples grown at 500 °C is indicative of the future potential of these films in such applications.

Acknowledgements This work was supported by Department of Energy Grant # DE-P26-08NT00198 and National Science Foundation, MRI Grant # 0723115.

References

1. Kalidindi NR, Bharathi KK, Ramana CV (2010) Appl Phys Lett 97:142107
2. Kalidindi NR, Manciu FS, Ramana CV (2011) ACS Appl Mater Interfaces 3:863
3. Manciu FS, Enriquez JL, Durrer WG, Yun Y, Ramana CV, SK Gullapalli SK (2010) Spectroscopic analysis of tungsten oxide thin films. J Mater Res 25:2401
4. Zhou L, Ren Q, Zhou X, Tang J, Chen Z, Yu C (2008) Microporous Mesoporous Mater 109:248
5. Boulova M, Lucazeau G (2002) J Solid State Chem 167:425
6. Ramana CV, Utsunomiya S, Ewing RC, Julien CM, Becker U (2006) J Phys Chem B 110:10430
7. Stankova M, Vilanova X, Calderer J, Llobet E, Brezmes J, Gracia I, Cane C, Correig X (2006) Sens Actuators, B 113:241
8. Lee SH, Cheong HM, Liu P, Smith D, Tracy CE, Mascarenhas A, Pitts JR, Deb SK (2001) Electrochim Acta 46:1995
9. Smith DJ, Vetelino JF, Falconer RS, Wittman EL (1993) Sens Actuators B Chem 13:264
10. Shen Y, Yamazaki T, Liu Z, Meng D, Kikuta T, Nakatani N (2009) Thin Solid Films 517:2069
11. Kanan SM, El-Kadri OM, Abu-Yousef IA, Kanan MC (2009) Sensors 9:8158
12. Pecquenard B, Lecacheux H, Livage J, Julien C (1998) J Solid State Chem 135:159
13. Shieh J, Feng HM, Hon MH, Juang HY (2002) Sens Actuators B 86:75
14. Sangaletti L, Depero LE, Sberveglieri G, Allieri B, Bontempi E, Groppelli S (1999) J Cryst Growth 198(199):1240
15. Gopel W, Reinhardt W (1996) Metal oxide sensors: new devices through tailoring interfaced on the atomic scale. In: Baltes H, Göpel W, Hesse J (eds) Sensors update sensor technology-application-markets, vol 1, VCH, Weinheim. ISBN 3-527-29329-9, p 49
16. Hu Y, Wang L, Li G (2007) Plasma Sci. Technol 9:452
17. Chai SY, Kim YJ, Lee WI (2006) J Electroceram 17:909
18. Depero LE, Gropelli S, Sora IN, Sangaletti L, Sberveglieri G, Tondello E (1996) J Solid State Chem 121:379
19. Hjelm A, Granqvist CG, Wills JM (1996) Phys Rev B 54:2436
20. Vemuri RS, Engelhard MH, Ramana CV (2012) ACS Appl Mater Interfaces 4:1371
21. Zhang WF, He YL, Zhang MS, Yin Z, Chen Q (2000) J Phys D Appl Phys 33:912
22. Locherer KR, Swainson IP, Salje EKH (1999) J Phys: Condens Matter 11:4143
23. Letheriotis G, Papaefthimiou S, Yianoulis P, Siokou A (2001) Thin Solid Films 384:298
24. Idriss H, Legare P, Maire G (2002) Surf Sci 515:413

ACS APPLIED MATERIALS & INTERFACES

RESEARCH ARTICLE

www.acsami.org

Crystal Structure, Phase, and Electrical Conductivity of Nanocrystalline $W_{0.95}Ti_{0.05}O_3$ Thin Films

N. R. Kalidindi,[†] F. S. Manciu,[‡] and C.V. Ramana*[,†]

[†]Department of Mechanical Engineering, Energy Systems Laboratory (ESL), and [‡]Department of Physics, University of Texas at El Paso, El Paso, Texas 79968, United States

ABSTRACT: $W_{0.95}Ti_{0.05}O_3$ films were fabricated using sputter-deposition onto Si(100) wafers in by varying the growth temperature from room temperature (RT) to 500 °C. X-ray diffraction (XRD), high-resolution scanning electron microscopy (SEM) coupled with energy-dispersive X-ray spectrometry (EDS), and Raman spectroscopy (RS) were performed to investigate the effect of temperature on the growth behavior, crystal structure, texturing, surface morphology, and chemical bonding of $W_{0.95}Ti_{0.5}O_3$ films. The results indicate that the effect of temperature is significant on the growth and microstructure of $W_{0.95}Ti_{0.05}O_3$ films. XRD results indicate that the effect of Ti is remarkable on the crystallization of WO_3. $W_{0.95}Ti_{0.05}O_3$ films grown at temperatures <300 °C are amorphous compared to pure WO_3 crystalline films crystallizing at 200 °C. Phase transformation is induced in $W_{0.95}Ti_{0.05}O_3$ resulting in tetragonal structure at ≥300 °C. The structural changes were also reflected in the intensities of −W−O−W− vibrational modes in RS measurements. The SEM imaging analysis indicates that the phase transformations are accompanied by a characteristic change in surface morphology. Room temperature electrical conductivity of $W_{0.95}Ti_{0.05}O_3$ films increases from 0.63 to 27 $(\Omega\ m)^{-1}$ with increasing temperature from RT to 400 °C due to improved structural order. Electrical conductivity exhibit a decrease at 500 °C (7.4 $(\Omega\ m)^{-1}$) due to disordering induced by Ti segregation, which is confirmed by XRD and RS measurements.

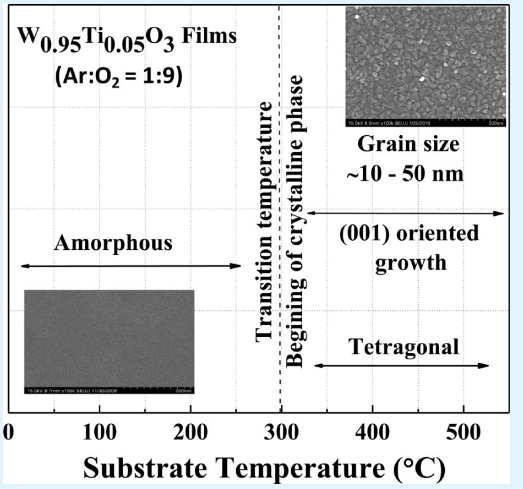

KEYWORDS: WO_3, Ti-doping, microstructure, phase transformations, H_2S sensors

1. INTRODUCTION

Semiconducting oxides have received significant recent attention as sensor materials because of their remarkable electrical properties sensitive to oxidative or reductive type of gases.[1−5] Currently, there has been a great deal of interest in WO_3 low-dimensional structures for a wide variety of applications in chemical and mechanical sensors, selective catalysis, electrochemical industry and environmental engineering.[1−7] It has been demonstrated that the sensing properties of WO_3 films will have numerous applications in environmental and industrial pollution monitoring. WO_3 films exhibit excellent functional activity to various gases, such as H_2S, NO_x, trimethylamine, and other organics, and are suitable for integrated sensors.[6−9] Most importantly, WO_3 nanocrystalline films have been established as one of the best gas sensors for the reducing gases such as NO_2, H_2, and CO and the results evidenced the role of the microstructure specifically the grain size.[6−9]

The search for novel materials for chemical sensors with enhanced performance has led the scientific community that works in the field to consider ternary compounds of metal-oxide semiconductors as potential candidates.[10] A leading criterion would be starting with a metal-oxide semiconductor that has already proven sensing capability, such as WO_3 in this case, and adding another properly chosen metal. Searching for new materials should be accompanied by a thorough study of the microstructural and electronic properties of the materials under consideration. In the context of the effort described herein, the present work was performed on the Ti-doping effects in a small and controlled amount into WO_3 to produce $W_{0.95}Ti_{0.05}O_3$. The focus of the investigation was to explore the effects of Ti and temperature on the growth behavior, microstructure, and electrical characteristics. The details of growth behavior, microstructure and electronic properties of pure WO_3 films and preliminary results on the Ti-doping effects were reported elsewhere.[11−14]

W−Ti alloy films have already been proven to exhibit low electrical resistance, thermal stability, oxidation resistance, inertness, good adhesion towards metal contact and the substrate, and high refractive index.[15−17] Therefore, investigating the fundamental aspects of microstructure evolution and structure−property relationships in W−Ti−O films may provide opportunities to tailor the microstructure and properties of the materials for the desired application, as well as optimization for chemical sensors. Interestingly, we found that Ti inhibits the crystallization, increases the temperature for crystal growth, and inhibits the

Received: December 8, 2010
Accepted: January 24, 2011
Published: February 16, 2011

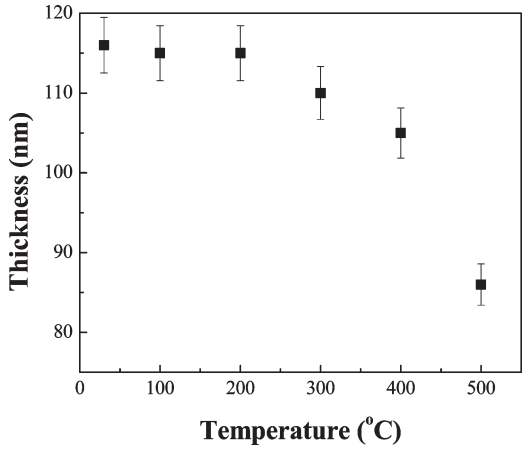

Figure 1. $W_{0.95}Ti_{0.05}O_3$ film thickness variation with substrate temperature. It is evident from the curve that the films grown at RT−200 °C exhibit more or less constant thickness. A decrease in film thickness at $T_s \geq 300$ °C is due to crystallization and improved density.

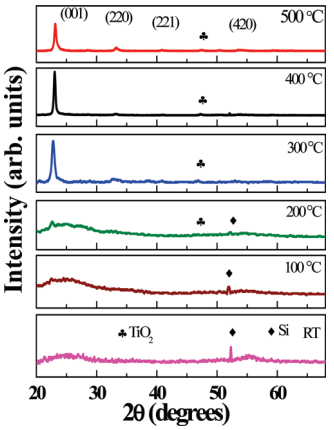

Figure 2. XRD patterns of $W_{0.95}Ti_{0.05}O_3$ films. It is evident from the curves that the films grown at RT-300 °C are amorphous whereas films grown at $T_s \geq 300$ °C are nanocrystalline. $W_{0.95}Ti_{0.05}O_3$ films crystallize in tetragonal phase as indicated by the XRD patterns for $T_s \geq 300$ °C.

grain growth compared to pure WO_3 films. The results obtained are presented and discussed in relation to microstructure and electrical properties in $W_{0.95}Ti_{0.05}O_3$ films.

2. EXPERIMENTAL SECTION

A. Fabrication. $W_{0.95}Ti_{0.05}O_3$ thin films were deposited onto silicon (Si) (100) wafers by radio-frequency (RF) (13.56 MHz) magnetron sputtering. The Si(100) substrates were cleaned by RCA (Radio Corporation of America) cleaning. All the substrates were thoroughly cleaned and dried with nitrogen before introducing them into the vacuum chamber, which was initially evacuated to a base pressure of $\sim 1 \times 10^{-6}$ Torr. Tungsten−titanium ($W_{0.95}Ti_{0.05}$) alloy target (Plasmaterials Inc.) of 2 in. diameter and 99.95% purity was employed for reactive sputtering. $W_{0.95}Ti_{0.5}$-target was placed on a 2-inch sputter gun, which is placed at a distance of 8 cm from the substrate. A sputtering power of 40 W was initially applied to the target while introducing high purity argon (Ar) into the chamber to ignite the plasma. Once the plasma was ignited the power was increased to 100 W and oxygen (O_2) was released into the chamber for reactive deposition. The flow of the Ar and O_2 and their ratio was controlled using MKS mass flow controllers. Before each deposition, $W_{0.95}Ti_{0.05}$ target was pre-sputtered for 10 min using Ar alone with shutter above the gun closed. The deposition was made for 1 h. The samples were grown at different temperatures (T_s) varying from room temperature (RT) to 500 °C. The substrates were heated by halogen lamps and the desired temperature was controlled by Athena X25 controller.

B. Characterization. The grown $W_{0.95}Ti_{0.5}O_3$ films were characterized by performing structural and electrical measurements. X-ray diffraction (XRD) measurements on $W_{0.95}Ti_{0.5}O_3$ films were by performed using a Bruker D8 Advance X-ray diffractometer. All the measurements were made ex situ as a function of growth temperature. XRD patterns were recorded using Cu Kα radiation (λ = 1.54056 Å) at RT. The coherently diffracting domain size (d_{hkl}) was calculated from the integral width of the diffraction lines using the well known Scherrer's equation after background subtraction and correction for instrumental broadening. The Scherrer equation is[18]

$$d_{hkl} = 0.9\lambda/\beta\cos\theta \quad (1)$$

where d_{hkl} is the size, λ is the wavelength, β is the width of a peak at half of its intensity, and θ is the angle of the peak.

Surface imaging analysis was performed using a high-performance and ultra high resolution scanning electron microscope (Hitachi S-4800). The secondary electron imaging was performed on $W_{0.95}Ti_{0.05}O_3$ films grown on Si wafers using carbon paste at the ends to avoid charging problems. The grain detection, size-analysis and statistical analysis was performed using the software provided with the SEM.

The Raman measurements were acquired at ambient conditions with an *alpha 300 WITec* confocal Raman system, using the 532 nm excitation of a Nd:YAG laser. An acquisition time of 5s for each spectrum and a 100× objective lens with a NA = 0.95 was used in all experiments.

DC electrical resistivity measurements were carried out under the vacuum of 1×10^{-2} Torr by two-probe method in a home-made setup. Resistance was measured by employing a Keithley electrometer. The point contacts were made by soldering the indium metal at the corners of the films.

3. RESULTS AND DISCUSSION

A. Film Thickness. $W_{0.95}Ti_{0.05}O_3$ thin films were found to be uniform and well-adherent to the substrate surface. All the samples exhibit a mixed yellowish-blue color. $W_{0.95}Ti_{0.05}O_3$ film thickness variation with T_s is shown in Figure 1. It is evident that the film thickness is not very sensitive to T_s until 300 °C, at which point thickness decreases slightly as T_s increases to 500 °C. We attribute this observed characteristic feature to the structural modifications in the grown films as function of T_s. $W_{0.95}Ti_{0.05}O_3$ film thickness is almost constant at T_s = RT−200 °C. However, a marked decrease in film thickness can be noted at $T_s \geq 300$ °C. From XRD and SEM measurements discussed in the later sections, the $W_{0.95}Ti_{0.05}O_3$ thin films in the constant thickness up to 200 °C were amorphous while those grown at $T_s \geq 300$ °C were crystalline. This suggests that the observed change in film thickness is due to crystallization and densification with increasing substrate temperature.

B. Crystal Structure. X-ray diffraction patterns of $W_{0.95}Ti_{0.05}O_3$ thin films are shown in Figure 2 as a function of T_s. The XRD curve (Fig. 2) of $W_{0.95}Ti_{0.05}O_3$ films grown at T_s = RT−200 °C did not show any peaks indicating their characteristic amorphous (a-$W_{0.95}Ti_{0.05}O_3$) nature. The diffraction peak begins to appear in XRD pattern when T_s = 300 °C indicating the film crystallization at this temperature. The intense peak corresponds to the tetragonal phase of WO_3 indicating that the $W_{0.95}Ti_{0.05}O_3$ films crystallize in tetragonal structure. The crystallization temperature noted for Ti-doped WO_3 films is higher when compared to that of pure WO_3 films grown using sputter-deposition.[11−13] We reported

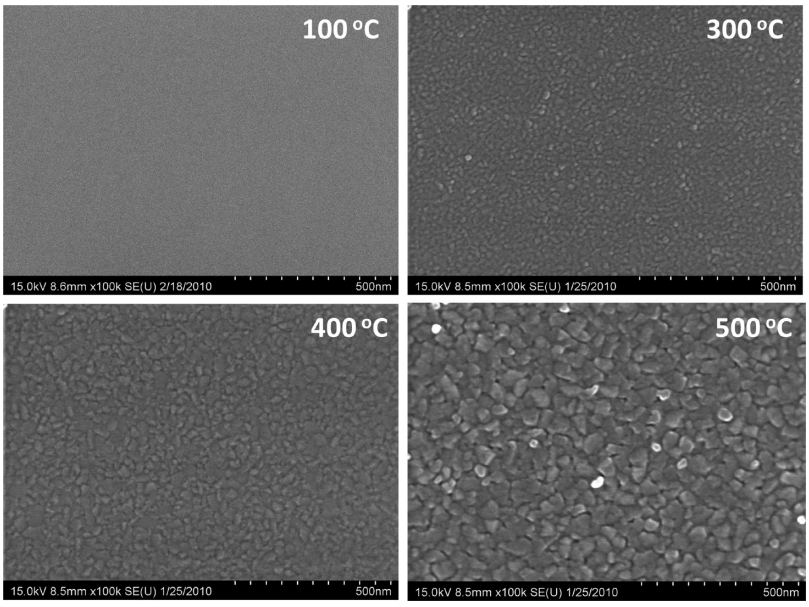

Figure 3. The high-resolution SEM images of $W_{0.95}Ti_{0.05}O_3$ films as a function of substrate temperature. It is evident from the images that the surface morphology of $W_{0.95}Ti_{0.05}O_3$ films is sensitive to the growth temperature. The morphological changes are correlated with the changes in crystal structure and specific phase formation of $W_{0.95}Ti_{0.05}O_3$ films as a function of growth temperature.

previously that pure WO_3 films crystallize at T_s = 100−200 °C.[11−13] The effect of Ti is remarkable in preventing crystallization of WO_3 and raises its crystallization temperature. The XRD peak is rather broad indicating the presence of nanocrystallites. It is evident (Figure 2) that the intensity of the peak which corresponds to diffraction from (001) planes increases with increasing T_s. This is indicative of an increase in the average crystallite-size and preferred orientation of the film along (00l) with increasing T_s. This behavior is quite similar to that observed in pure WO_3 films.[11] The preferred *c*-axis orientation of $W_{0.95}Ti_{0.05}O_3$ films could be due to the growth process minimizing the internal strain-energy in the film.[12,19,20] Anisotropy exists in crystalline materials and the strain energy densities will typically be different for different crystallographic directions. The growth will favor those orientations with low strain energy density.[12,19−21] Therefore, increasing T_s favors the preferred orientation along (00l) while minimizing the strain-energy in the $W_{0.95}Ti_{0.05}O_3$ films. The most important feature that can be noted is the formation of a small amount of TiO_2 phase for the films grown at T_s = 400−500 °C. Note that the peak becomes broad at T_s = 500 °C.

The preferred growth of $W_{0.95}Ti_{0.05}O_3$ films, as seen in XRD, allows calculating the relative strain factor using the XRD data. The strain factor (Γ), which is derived from the lattice mismatch, is calculated using the formula

$$\Gamma = \frac{d_{(100)\mathrm{Si}} - d_{(001)\mathrm{sample}}}{d_{(001)\mathrm{sample}}}\% \qquad (2)$$

The strain factor Γ is found to be ∼3% for the samples grown at T_s = 300−500 °C. The observed strain can be understood in terms of the combined effect of two factors. Effective increase in the number of atoms due to surface and interface effects for the reduced dimensions of the nanocrystallites is the first. The stabilization of the crystal formation and lattice parameters with increasing T_s is the later.

C. Surface, Interface Morphology, and Growth Behavior. The high-resolution SEM images of $W_{0.95}Ti_{0.05}O_3$ films as a function of T_s are shown in Figure 3. The amorphous nature resulting from disordering induced by Ti is clearly evident in the SEM images of $W_{0.95}Ti_{0.05}O_3$ films grown at T_s = RT−200 °C. A fine microstructure and uniform distribution of dense spherical particles can be seen in $W_{0.95}Ti_{0.05}O_3$ films grown at T_s = 300−500 °C. The observed average grain size variation with T_s is shown in Figure 4a. It must be emphasized that the grain size indicated at 200 °C is based on the fact that the SEM images have occasionally shown the grains of ≤6 nm which are embedded in the amorphous matrix. However, most of the film volume is amorphous and didn't reveal even a sign of localized structural order with other spectroscopic or X-ray diffraction analysis. Most significant point is the remarkable effect of temperature on the surface morphology of $W_{0.95}Ti_{0.05}O_3$ films. Based on thickness variation, SEM and XRD data as a function of T_s, the growth behavior of $W_{0.95}Ti_{0.05}O_3$ films can be conveniently divided into two zones, where the morphology differences are significant. The first category or zone contains the set of $W_{0.95}Ti_{0.05}O_3$ films grown at temperatures <300 °C. The second is the set of $W_{0.95}Ti_{0.05}O_3$ films grown at temperatures ≥300 °C. No features can be seen for $W_{0.95}Ti_{0.05}O_3$ films grown at RT even at very high magnifications (Figure 3a). This observation is in agreement with the XRD results indicating the complete amorphous nature of the samples. If temperature is low such that the period of the atomic jump process of adatoms on the substrate surface is very large, the condensed species may stay stuck to the regions where they are landing thus leading to an amorphous $W_{0.95}Ti_{0.05}O_3$ films. The adatom mobility on the surface increases with increasing temperature. The small, dense particles spherical in shape can be noticed in SEM images for $W_{0.95}Ti_{0.05}O_3$ films grown at 300−400 °C. The SEM data along with appearance of diffraction peaks in XRD clearly indicate that 300 °C is the critical temperature to promote the growth of nanocrystalline $W_{0.95}Ti_{0.05}O_3$ films. For the given set of experimental conditions, a temperature of 300 °C is, therefore, favorable to provide sufficient energy for $W_{0.95}Ti_{0.05}O_3$ crystallization.

The XRD and SEM results suggest that a further increase in temperature beyond 300 °C results in changes in the crystal

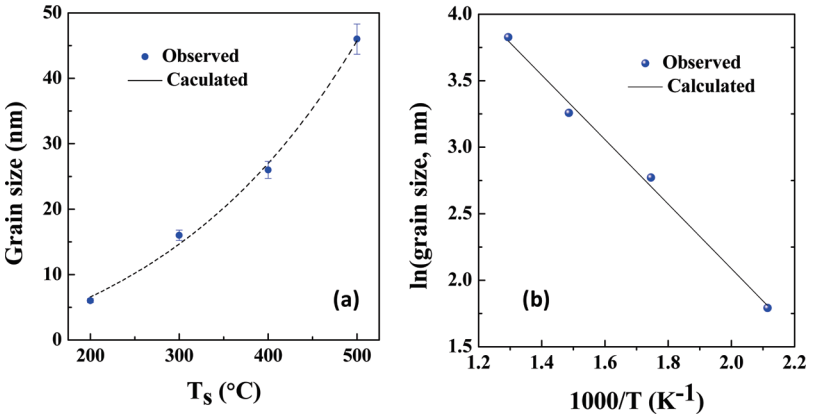

Figure 4. (a) Variation in grain size of $W_{0.95}Ti_{0.05}O_3$ films with substrate temperature. The circles represent the experimental data while the line represents the fit to the exponential function according to eq 3. (b) Ln(grain size) vs $1 \times 10^3/T$ plot for the data shown in panel a. Solid line represents the linear fit. Excellent agreement between the observed data and linear fit suggests the thermally activated growth process of sputter-deposited $W_{0.95}Ti_{0.05}O_3$ films.

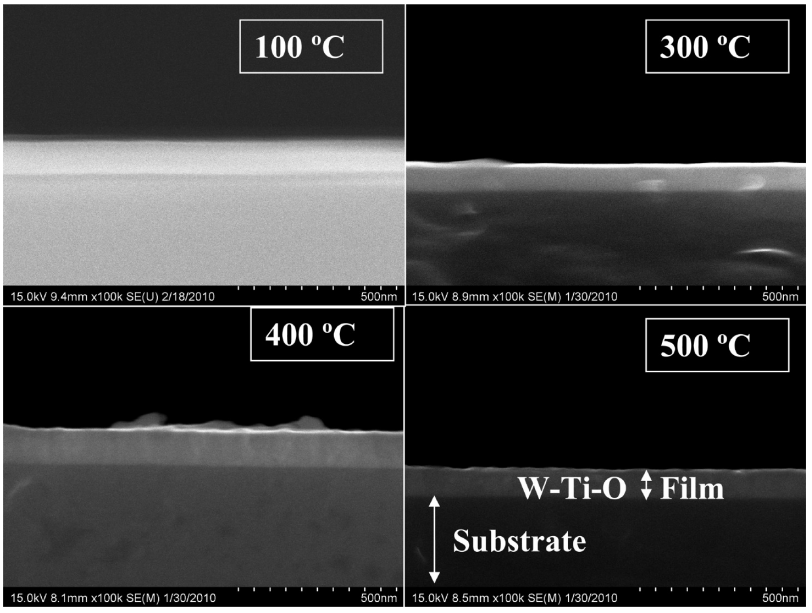

Figure 5. Si−$W_{0.95}Ti_{0.05}O_3$ interface cross-sectional SEM images of $W_{0.95}Ti_{0.05}O_3$ films grown at various temperatures. The Si substrate and $W_{0.95}Ti_{0.05}O_3$ film regions are as indicated.

structure and morphology. $W_{0.95}Ti_{0.05}O_3$ films continue to show preferred growth along with an increase in average particle size with increasing T_s. A functional relationship obtained between the average particle size (L) and the temperature fits to an exponential growth function (Figure 4b). The data supports thermally activated growth process of nanocrystalline $W_{0.95}Ti_{0.05}O_3$ films. Therefore, similar to the diffusion coefficient equation[22,13] L can be expressed as

$$L = L_o \exp(-\Delta E/k_B T) \quad (3)$$

where L is the average particle size, L_0 is a pre-exponential factor or proportionality constant which depends on the specific film, substrate materials involved, ΔE the activation energy, k_B the Boltzmann constant, and T the absolute temperature. The data analysis and Arrehenius plot are presented in Figure 4b, where the data points and a linear fit to the data are shown. It is important to recognize the functional linear relationship which is an indicative of thermally driven growth of nanocrystalline $W_{0.95}Ti_{0.05}O_3$ films. The activation energy derived from the slope of the linear fit (Figure 4b) is ~0.21 eV, which is higher than that reported for pure WO_3 films.[13]

The cross-sectional SEM images of $W_{0.95}Ti_{0.5}O_3$−Si interfaces for $W_{0.95}Ti_{0.5}O_3$ films grown at various temperatures are shown in Figure 5. The $W_{0.95}Ti_{0.5}O_3$ film and Si-substrate regions are as indicated in Figure 5 for a representative sample. The cross-sectional SEM images indicate that the $W_{0.95}Ti_{0.5}O_3$ films grow in a columnar structure on Si surfaces.

D. Local Structure, Chemical Bonding, and Composition. The EDS spectra of representative $W_{0.95}Ti_{0.05}O_3$ films as a function of T_s are shown in Figure 6. The spectra indicate the characteristic X-ray peaks (as labeled in Figure 6) corresponding to W, Ti, and O atoms present in the sample. The absence of any other peaks except those due to W and O indicate that the sample consists exclusively of W−Ti oxide phase. It is well-known that

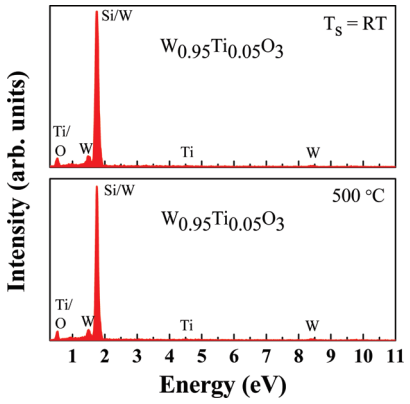

Figure 6. EDS spectra of $W_{0.95}Ti_{0.05}O_3$ films. The peaks due to X-rays emitted from W, Ti, and O present in the films are as labeled.

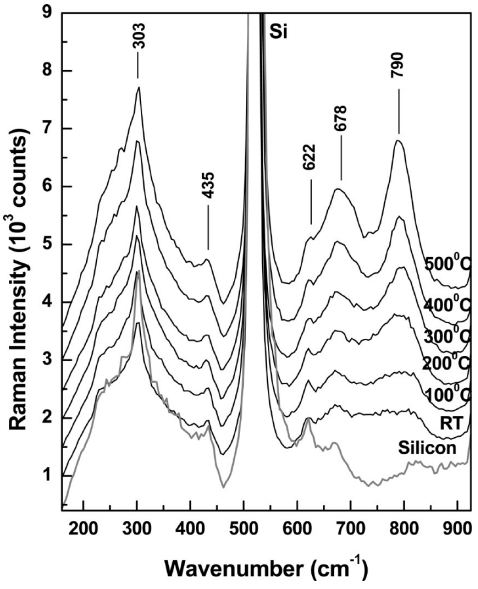

Figure 7. Raman spectra of $W_{0.95}T_{0.i5}O_3$ films grown at various temperatures.

the X-rays generated are characteristic of the atoms.[23,24] Therefore, the detection of x-rays emitted from the sample as a result of sample-electron beam interaction provides the identification of the atoms present in the crystal. The emitted x-ray peaks detected are only from W and O while the peak due to Si substrate is serving as a reference. No other elements were detected, which is a sign of high purity $W_{0.95}Ti_{0.05}O_3$ films without any elemental impurities incorporated from chemical processing or post-preparation handling.

The results of Raman measurements of $W_{0.95}Ti_{0.05}O_3$ samples grown at Si substrate temperatures between RT (bottom spectrum) and 500 °C (top spectrum) are presented in Figure 7. Besides clear spectroscopic evidence of the most intense Si vibration at 522 cm^{-1}, the spectra of $W_{0.95}Ti_{0.05}O_3$ samples also show the existence of Si−O bonds at 303, 435, 622, and 675 cm^{-1}. For easier comparison and association of these latter features with the influence of Si, in Figure 6, we also present the Raman spectrum of the substrate alone (gray line).

Although the spectra of $W_{0.95}Ti_{0.05}O_3$ samples recorded for growth temperatures less than 200 °C largely resemble the Si

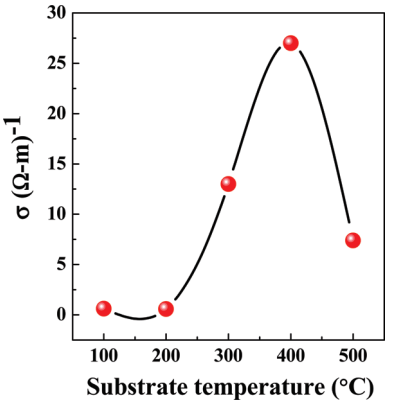

Figure 8. Variation in electrical conductivity of $W_{0.95}Ti_{0.05}O_3$ films with substrate temperature.

spectrum, which demonstrates the amorphous nature of these samples, the slight increase and sharpening at higher temperatures of the intensities of the two broad bands centered around 678 and 790 cm^{-1} reveal a trend towards ordering and crystallization of the material. These features transform into definite Raman peaks at 400 and 500 °C. Not only do Raman data corroborate with our previous observations of continuing crystallization with increasing temperature, but from the position of the 790 cm^{-1} Raman vibration we can infer in our samples a morphological transformation of pure WO_3 with Ti doping. This affirmation is based on an approximately 20 cm^{-1} shift between the 790 cm^{-1} feature and the typical W−O stretching mode of pure WO_3, previously observed in our work around 810 cm^{-1}.[25] Similar behavior, namely a frequency decrease in the position of this Raman peak, was reported in the literature for Ti-doped WO_3.[26] Unfortunately, because of the relatively strong influence of the Si substrate, no detectable Ti−O bonds were observed in our $W_{0.95}Ti_{0.05}O_3$ Raman spectra to confirm the formation of TiO_2 as observed in the XRD measurements.

E. Electrical Characteristics. The room temperature electrical characteristics of $W_{0.95}Ti_{0.05}O_3$ films are shown in Fig. 8. It can be seen that with increasing T_s up to 400 °C the conductivity increases, which is due to improvement in the crystal structure of $W_{0.95}Ti_{0.05}O_3$ films. A small decrease in conductivity value at T_s = 500 °C could be due to the formation of excess TiO_2, as evidenced in XRD data. The electrical resistivity is reported to increase with size-reduction due to the increasing grain boundary volume and associated impedance to the flow of charge carriers.[27−31] If the crystallite size is smaller than the electron mean free path, grain boundary scattering dominates and hence the resistivity increases. The resistivity is also very sensitive to lattice imperfections in solids, such as vacancies and dislocations that are present in nanocrystalline materials.[11] In addition to that, lattice strain and the distortions can affect the motion of charge causing a increase in resistivity.[27−31] The substrate temperature dependence of the conductivity data observed for $W_{0.95}Ti_{0.05}O_3$ can be explained taking these factors into consideration. $W_{0.95}Ti_{0.05}O_3$ films grown at T_s = RT-200 °C are amorphous. The randomness or disordered structure of the films induced by Ti, therefore, accounts for the observed conductivity of a-$W_{0.95}Ti_{0.05}O_3$ films. An increase in conductivity with increasing growth temperature can be attributed to the structural transformation from amorphous to tetragonal phase and the preferred orientation of the film along (001). In addition, a decrease in strain energy of the growing $W_{0.95}Ti_{0.05}O_3$ film, as discussed using the XRD results, with increasing temperature also causes the increase in

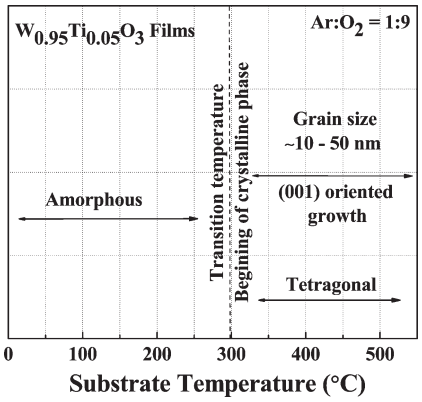

Figure 9. Phase diagram summarizing the microstructure evolution of $W_{0.95}Ti_{0.05}O_3$ films as a function of temperature.

conductivity. Finally, based on the XRD, SEM, EDS, and RS measurements, we propose the phase diagram for the microstructure evolution of $W_{0.95}Ti_{0.05}O_3$ thin films as shown in Figure 9. The phase diagram summarizes the observed structural changes as a function of substrate temperature and could provide a roadmap while considering the $W_{95}Ti_5O_3$ thin films for the desired set of electronic or sensor applications.

4. SUMMARY AND CONCLUSIONS

$W_{95}Ti_5O_3$ thin films were fabricated using sputter-deposition and their structural and electrical properties were investigated in detail. The effect of temperature is significant on the growth behavior, surface morphology, crystal structure and electrical characteristics of $W_{95}Ti_5O_3$ thin films. With increasing temperature, the $W_{95}Ti_5O_3$ films are seen to transform from amorphous to tetragonal structure. The amorphous-to-crystalline transition temperature is 300 °C for $W_{0.95}Ti_{0.5}O_3$ films which is higher than that for pure WO_3 films (200 °C). The structural studies demonstrate that the effect of Ti is remarkable on the crystallization of WO_3. Phase transformation is induced in $W_{0.95}Ti_{0.05}O_3$ resulting in tetragonal structure at ≥300 °C. The morphological changes associated with the structural transformations were confirmed by the Raman spectroscopic measurements. Room temperature electrical conductivity of $W_{0\cdot95}Ti_{0.05}O_3$ films increases from 0.63 to 27 $(\Omega\ cm)^{-1}$ with increasing temperature from RT to 400 °C because of improved structural order. The observed decrease in electrical conductivity at 500 °C (7.4 $(\Omega\ cm)^{-1}$) is due to disordering induced by Ti segregation, which is confirmed by XRD. On the basis of the results obtained in this work, a phase diagram for the microstructure evolution in $W_{0.95}Ti_{0.05}O_3$ thin films is proposed.

AUTHOR INFORMATION

Corresponding Author

*E-mail: rvchintalapalle@utep.edu.

ACKNOWLEDGMENT

This material is based on work supported by the Department of Energy under Award DE-PS26-08NT00198-00. Hitachi 4800 SEM used for the morphology and X-ray chemical analysis of Ti-doped WO_3 samples in this work was acquired through the support from National Science Foundation (NSF-DMR-0521650). The support from National Science Foundation to acquire *alpha 300 WITec* confocal Raman system through Grant 0723115 is gratefully acknowledged.

REFERENCES

(1) Zhu, L.F.; She, J.C.; Luo, J.Y.; Deng, S.H.; Chen., J.; Xu, N.S. *J. Phys. Chem. C* **2010**, *114*, 15504–15509.
(2) Wang, L.; Teleki, S. E.; Pratsinis, S. E.; Gouma, P. I. *Chem. Mater.* **2008**, *20*, 4794–4796.
(3) Wolcott, A.; Kuykendall, T.R.; Chen, W.; Chen, S.; Zhang, J.Z. *J. Phys. Chem. B* **2006**, *110*, 25288–25296.
(4) Li, X.; Lou, T.-J.; Sun, X.-M.; Li, Y.-D. *Inorg. Chem.* **2004**, *43*, 5442–5449.
(5) Wang, X.; Miura, N.; Yamazoe, N. *Sens. Actuators, B* **2000**, *66*, 74–79.
(6) Tatsuma, T.; Saitoh, S.; Ohko, Y.; Fujishima, A. *Chem. Mater.* **2001**, *13*, 2838–2842.
(7) Szilgyi, I.M.; Madarsz, J.; Pokol, G.; Kirly, P.; Trknyi, G.; Saukko, S.; Mizsei, J.; Tth, A.L.; Szab., A.; Varga-Josepovits, K. *Chem. Mater.* **2008**, *20*, 4116–4125.
(8) Meixner, H.; Lampe, U. *Sens. Actuators, B* **1996**, *33*, 198–202.
(9) Baeck, S. H.; Jaramillo, T.; Stucky, G. D.; McFarland, E. W. *Nano Lett.* **2002**, *2*, 831–834.
(10) Ferroni, M.; Guidi, V.; Martinelli, G.; Nelli, P.; Sberveglieri, G. *Sens. Actuators, B* **1997**, *44*, 499–504.
(11) Vemuri, R. S.; Kamala Bharathi, K.; Gullapalli, S. K.; Ramana, C. V. *ACS Appl. Mater. Interfaces* **2010**, *2*, 2623–2628.
(12) Kalidindi, N.R.; Kamala Bharathi, K.; Ramana, C.V. *Appl. Phys. Lett.* **2010**, *97*, 142107.
(13) Gullapalli, S. K.; Vemuri, R. S.; Manciu, F. S.; Enriquez, J. L.; Ramana, C. V. *J. Vac. Sci. Technol., A* **2010**, *28*, 824–828.
(14) Gullapalli, S. K.; Vemuri, R. S.; Ramana, C. V. *Appl. Phys. Lett.* **2010**, *96*, 171903.
(15) Glebovsky, V. G.; Yu, V.; Yaschak; Baranov, V. V.; Sackovich, E. L. *Thin Solid Films* **1995**, *257*, 1–5.
(16) Guidi, V.; Boscarino, D.; Comini, E.; Faglia, G.; Ferroni, M.; Malagu, C.; Martnelli, G.; Rigato, V.; Sberveglieri, G. *Sens. Actuators, B* **2000**, *65*, 264.
(17) Bundaleski, N.; Petrovic, S.; Perusko, D.; Kovac, J.; Zalar, A. *Appl. Surf. Sci.* **2008**, *254*, 6390–6394.
(18) Cullity, B. D.; Stock, S. R., *Elements of X-Ray Diffraction*, 3rd ed.; Prentice-Hall: New York, 2001.
(19) Ramana, C. V.; Smith, R. J.; Julien, C. M. *J. Vac. Sci. Technol., A* **2004**, *22*, 2453–2458.
(20) Ramana, C. V.; Julien, C. M. *Chem. Phys. Lett.* **2006**, *428*, 114–118.
(21) Ramana, C.V.; Smith, R. J.; Hussain, O. M. *Phys. Status Solidi A* **2003**, *199*, R4–7.
(22) Kittel, C., *Introduction to Solid State Physics*; Wiley: New York, 1968.
(23) Ramana, C. V.; Ait-Salah, A.; Utsunomiya, S.; Mauger, A.; Gendron, F.; Julien, C.M *Chem. Mater.* **2007**, *19*, 5319–5324.
(24) Ramana, C. V.; Ait-Salah, C. V.; Utsunomiya, A.; Morhange, S.; Mauger, J. F.; Gendron, A.; Julien, F. *J. Phys. Chem. C* **2007**, *111*, 1049–1054.
(25) Manciu, F.S.; Enriquez, J.L.; Durrer, W.G.; Yun, Y.; Ramana, C. V.; Gullapalli, S.K, *J. Mater. Res.* **2010**, in press.
(26) Hu, Y.; Wang, L.; Li, G *Plasma Sci. Technol.* **2007**, *9*, 432.
(27) Depero, L.E.; Natali Sora, I.; Perego, C.; Sangaletti, L.; Sberveglieri, G. *Sens. Actuators, B* **1996**, *31*, 19–24.
(28) Wu, L.; Tien-Shou, W.; Chung-Chuang, W. *J. Phys. D: Appl. Phys.* **1980**, *13*, 259–266.
(29) Bakonyi, I.; Toth-Kadar, E.; Tarnoczi, T.; Varga, L.; Cziraki, A.; Gerocs, I.; Fogarassy, B. *Nanostruct. Mater.* **1993**, *3*, 155–158.
(30) Ambily, S.; Menon, C. S. *Thin Solid Film* **1999**, *347*, 284–289.
(31) Ajai Gupta, K.; Kumar, V.; Khare, N. *Solid State Sci.* **2007**, *9*, 817–823.

The disordering effect of Ti observed in the microstructure and electrical properties of W 0.95 Ti 0.05 O 3 thin films

N. R. Kalidindi, K. Kamala Bharathi, and C. V. Ramana

Citation: Applied Physics Letters **97**, 142107 (2010); doi: 10.1063/1.3496473
View online: http://dx.doi.org/10.1063/1.3496473
View Table of Contents: http://scitation.aip.org/content/aip/journal/apl/97/14?ver=pdfcov
Published by the AIP Publishing

The disordering effect of Ti observed in the microstructure and electrical properties of $W_{0.95}Ti_{0.05}O_3$ thin films

N. R. Kalidindi, K. Kamala Bharathi, and C. V. Ramana[a)]
Department of Mechanical Engineering, University of Texas at El Paso, El Paso, Texas 79968, USA

(Received 23 July 2010; accepted 13 September 2010; published online 6 October 2010)

We report on the inhibition of WO_3 crystallization by the addition of Ti observed in sputter-deposited $W_{0.95}Ti_{0.05}O_3$ films. The effect of growth-temperature on the crystallization indicates that the $W_{0.95}Ti_{0.05}O_3$ films grown at temperatures <300 °C are amorphous compared to WO_3 crystalline films at 100–200 °C. Phase transformation is induced in $W_{0.95}Ti_{0.05}O_3$ resulting in tetragonal structure at ≥ 300 °C. The corresponding electrical properties exhibit a clear distinction as a function of these structural transformations. Temperature-dependent dc electrical conductivity (80–300 K) shows the semiconducting nature of $W_{0.95}Ti_{0.05}O_3$ films and exhibits two distinct regions indicative of two different types of transport mechanisms. © *2010 American Institute of Physics*. [doi:10.1063/1.3496473]

Currently, there has been a great deal of interest in WO_3 low-dimensional structures for a wide variety of applications in chemical and mechanical sensors, selective catalysis, electrochemical industry, and environmental engineering.[1–8] It has been demonstrated that the sensing properties of WO_3 films will have numerous applications in environmental and industrial pollution monitoring. WO_3 films exhibit excellent functional activity to various gases, such as H_2S, NO_x, trimethylamine, and are suitable for integrated sensors.[4,5]

The search for novel materials for chemical sensors with enhanced performance has lead the scientific community that works in the field to consider ternary compounds of metal-oxide semiconductors as potential candidates.[7] A leading criterion would be starting with a metal-oxide semiconductor that has already proven sensing capability, such as WO_3 in this case, and adding another properly chosen metal. Searching for new materials should be accompanied by a thorough study of the microstructural, electrical, and optical properties of the material under consideration. In the context of the effort described herein, the present work was performed on the Ti-doping effects in a small and controlled amount into WO_3 to produce $W_{0.95}Ti_{0.05}O_3$ and the effects on their microstructure and electrical properties. W–Ti alloy films have already been proven to exhibit low electrical resistance, thermal stability, oxidation resistance, inertness, good adhesion toward metal contact and the substrate, and high refractive index.[9] Therefore, investigating the fundamental aspects of microstructure evolution and structure-property relationships in W–Ti–O films may provide opportunities to tailor the microstructure and properties of the materials for the desired application, as well as optimization for chemical sensors. Interestingly, we found that Ti inhibits the crystallization, increases the temperature for crystal growth and inhibits the grain growth compared to pure WO_3 films. The results obtained are presented and discussed in relation to microstructure and electrical properties in $W_{0.95}Ti_{0.05}O_3$ films.

$W_{0.95}Ti_{0.05}O_3$ thin films were deposited onto silicon (Si) wafers by radio-frequency (rf) (13.56 MHz) magnetron sputtering. The Si(100) substrates were thoroughly cleaned and dried with nitrogen before introducing them into the vacuum chamber, which was initially evacuated to a base pressure of $\sim 10^{-6}$ Torr. A W–Ti ($W_{0.95}Ti_{0.05}$) alloy target (Plasmaterials Inc.) of 2″ diameter and 99.95% purity was employed for reactive sputtering. The $W_{0.95}Ti_{0.05}$-target was placed on a 2 in. sputter gun, which was correspondingly placed at a distance of 8 cm from the substrate. A sputtering power of 40 W was initially applied to the target while introducing high purity argon (Ar) into the chamber causing plasma ignition. Once ignited, the power was increased to 100 W and oxygen (O_2) was released into the chamber for reactive deposition. The flow of the Ar and O_2 and their ratio was controlled using MKS mass flow meters. Before each deposition, the $W_{0.95}Ti_{0.05}$-target was presputtered for 10 min using Ar alone with the shutter above the gun closed. The samples were deposited at different temperatures (T_s) varying from RT to 500 °C. The substrates were heated by halogen lamps and the desired temperature was controlled by an Athena X25 controller.

X-ray diffraction (XRD) measurements on $W_{0.95}Ti_{0.05}O_3$ films were performed by using a Bruker D8 Advance x-ray diffractometer. All the measurements were made ex-situ as a function of growth temperature. XRD patterns were recorded using Cu $K\alpha$ radiation ($\lambda = 1.540\,56$ Å) at RT. The coherently diffracting domain size (d_{hkl}) was calculated from the integral width of the diffraction lines using the well known Scherrer's equation.[8] Surface imaging analysis was performed using a high-performance and ultrahigh resolution scanning electron microscope (SEM) (Hitachi S-4800). dc electrical resistivity measurements were carried out under the vacuum of 10^{-2} Torr by two-probe method in the temperature range 120–300 K by employing a closed cycle refrigerator (CCR). Resistance was measured by employing a Keithley electrometer. The temperature was measured using a silicon diode sensor and employing a Lakeshore temperature controller (Model 330). The film was kept on the cold head of the CCR. The point contacts were made by soldering the indium metal at the corners of the films.

The XRD patterns of $W_{0.95}Ti_{0.05}O_3$ films are shown in Fig. 1 as a function of T_s. The XRD curve (Fig. 1) of $W_{0.95}Ti_{0.05}O_3$ films grown at $T_s = RT - 200$ °C did not show

a)Author to whom correspondence should be addressed. Electronic mail: rvchintalapalle@utep.edu.

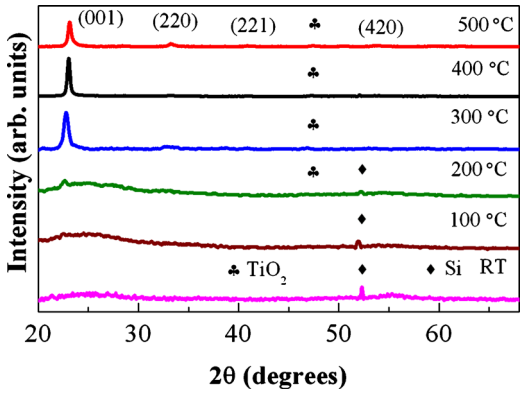

FIG. 1. (Color online) XRD patterns of $W_{0.95}Ti_{0.05}O_3$ films. The peaks due to Si substrate and TiO_2 secondary phase are as labeled. It is evident from the curves that the films grown at T_s=RT–200 °C are amorphous whereas films grown at $T_s \geq 300$ °C are nanocrystalline. $W_{0.95}Ti_{0.05}O_3$ films crystallize in tetragonal structure.

any peaks indicating their characteristic amorphous (a-$W_{0.95}Ti_{0.05}O_3$) nature. The diffraction peak begins to appear in XRD pattern when T_s=300 °C indicating the film crystallization at this temperature. The intense peak corresponds to the tetragonal phase of WO_3 indicating that the $W_{0.95}Ti_{0.05}O_3$ films crystallize in tetragonal structure. The crystallization temperature noted for Ti-doped WO_3 films is higher when compared to that of pure WO_3. We reported previously that pure WO_3 films crystallize at T_s =100–200 °C.[8] The effect of Ti is remarkable in preventing crystallization of WO_3 and raises its crystallization temperature. The XRD peak is rather broad indicating the presence of nanocrystallites. It is evident (Fig. 1) that the intensity of the peak which corresponds to diffraction from (00l) planes increases with increasing T_s. This is indicative of an increase in the average crystallite-size and preferred orientation of the film along (00l) with increasing T_s. This behavior is quite similar to that observed in pure WO_3 films.[8,10] The preferred *c*-axis orientation of $W_{0.95}Ti_{0.05}O_3$ films could be due to the growth process minimizing the internal strain-energy in the film. Anisotropy exists in crystalline materials and the strain energy densities will typically be different for different crystallographic directions. The growth will favor those orientations with low strain energy density. Therefore, increasing T_s favors the preferred orientation along (00l) while minimizing the strain-energy in the $W_{0.95}Ti_{0.05}O_3$ films. The most important feature that can be noted is the formation of a small amount of TiO_2 phase for the films grown at T_s =400–500 °C. Note that the peak becomes broad at T_s =500 °C.

The SEM images of $W_{0.95}Ti_{0.05}O_3$ films as a function of T_s are shown in Fig. 2. The amorphous nature due to disordering induced by Ti is clearly evident for $W_{0.95}Ti_{0.05}O_3$ films grown at T_s=RT–200 °C. A fine microstructure and uniform distribution of dense particles can be seen in $W_{0.95}Ti_{0.05}O_3$ films grown at T_s=300–500 °C.

The electrical characteristics of $W_{0.95}Ti_{0.05}O_3$ films are shown in Fig. 3. The room temperature electrical conductivity (σ) variation in $W_{0.95}Ti_{0.05}O_3$ films with T_s is shown as an inset in Fig. 3. It can be seen that with increasing T_s up to 400 °C the σ increases, which is due to improvement in the crystal structure of $W_{0.95}Ti_{0.05}O_3$ films. A small decrease in σ value at T_s=500 °C could be due to the formation of excess TiO_2, as evidenced in XRD data. The σ is reported to decrease with size-reduction due to the increasing grain boundary volume and associated impedance to the flow of charge carriers.[11,12] If the crystallite size is smaller than the electron mean free path, grain boundary scattering dominates, and hence the conductivity decreases. The σ value is also very sensitive to lattice imperfections in solids, such as vacancies and dislocations that are present in nanocrystalline materials. In addition to that, lattice strain and the distortions can affect the motion of charge causing a decrease σ.[13–15] The σ-T_s data observed for $W_{0.95}Ti_{0.05}O_3$ can be explained taking these factors into consideration. $W_{0.95}Ti_{0.05}O_3$ films grown at T_s=RT–200°C are amorphous in nature, which is induced by Ti, therefore, accounts for the observed low σ of a-$W_{0.95}Ti_{0.05}O_3$ films. An increase in σ with increasing T_s can be attributed to the structural transformation and the preferred orientation. In addition, a decrease in strain energy of the growing $W_{0.95}Ti_{0.05}O_3$ film, as discussed using the XRD results, with increasing T_s also causes the increase in σ.

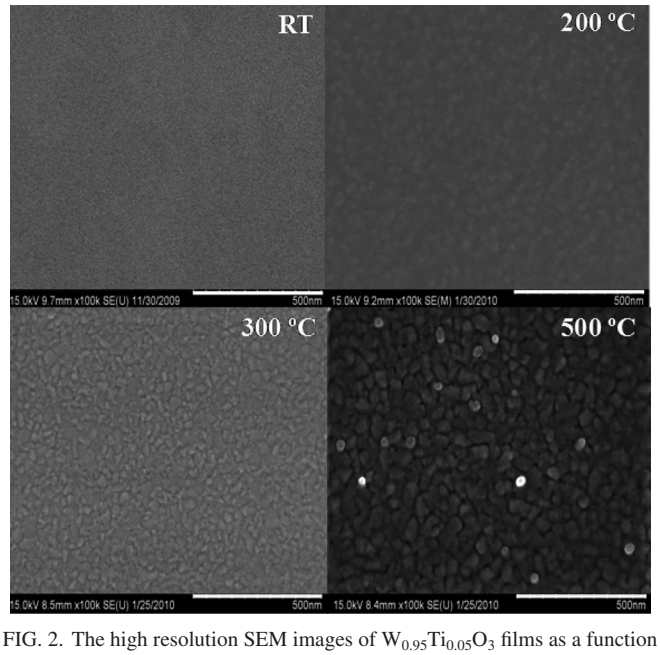

FIG. 2. The high resolution SEM images of $W_{0.95}Ti_{0.05}O_3$ films as a function of T_s. The morphology changes as a function of T_s are evident in the images.

Conductivity decreases exponentially with decreasing temperature from 300 to 80 K, which indicates the semiconducting nature of all the $W_{0.95}Ti_{0.05}O_3$ films (Fig. 3). How-

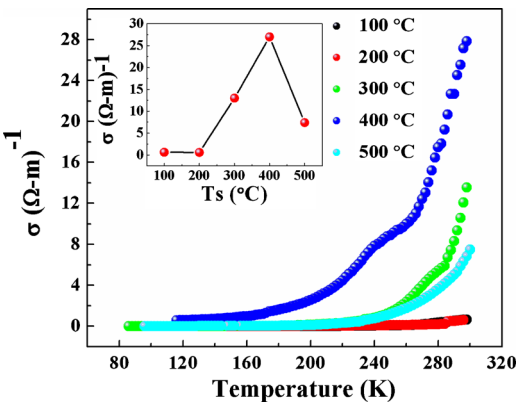

FIG. 3. (Color online) The temperature-dependent electrical conductivity plots of $W_{0.95}Ti_{0.05}O_3$ films. Insert shows the variation in room-temperature electrical conductivity of $W_{0.95}Ti_{0.05}O_3$ films with T_s. A drop in conductivity for $W_{0.95}Ti_{0.05}O_3$ films grown at T_s=500 °C is due to TiO_2 formation.

TABLE I. Activation energy values calculated from the ln σ vs $1000/T$ plots of $W_{0.95}Ti_{0.05}O_3$ thin films for different temperature regions.

T_s (°C)	Activation energy (eV)	
	300–210 K	210–80 K
100	0.35	0.10
200	0.36	0.11
300	0.34	0.08
400	0.34	0.08
500	0.35	0.09

ever, a marked difference in the temperature-dependence of σ can be seen for a-$W_{0.95}Ti_{0.05}O_3$ films when compared to t-$W_{0.95}Ti_{0.05}O_3$ films. This behavior can be attributed to the size and phase transformation. The most remarkable feature of these temperature-dependent electrical conductivity curves is the observation of two distinct regions that are indicative of two different conduction mechanisms operating in the respective temperature regions.[14]

Conductivity in semiconductors is due to both hopping of electrons and charge transport via excited states, and it can be expressed as[15,16]

$$\sigma = A_1 \exp\left(\frac{-E_1}{k_B T}\right) + A_2 \exp\left(\frac{-E_2}{k_B T}\right) + \ldots A_n \exp\left(\frac{-E_n}{k_B T}\right), \quad (1)$$

where E_1 is the activation energy for intrinsic conduction and $E_2, E_3, \ldots, E_n$ are the activation energies needed for hopping conduction. The terms $A_1, A_2, A_3, \ldots, A_n$ are constants and k_B is the Boltzmann constant. The activation energy values at different temperature ranges (300–210 K and 210–80 K) calculated from the ln σ versus $1000/T$ plots are listed in Table I. The activation energy is found to be higher in the 300–210 K temperature region when compared that in the 210–80 K temperature region. Decreasing activation energy with decreasing temperature in transition metal oxides has been explained by small-polaron theory.[16] The variable range hopping (VRH) model of small polarons also predicts continuously decreasing activation energy with decreasing temperature. Small polaron formation occurs when electron–phonon interaction is strong enough, while the polaron transport occurs by a hopping process at sufficiently higher temperatures.[14] The multiphonon hopping process freezes out at lower temperatures and conduction through extended states in a polaron band becomes the dominant mechanism. This tends to lead to a decay of the conductivity and activation energy as the temperature is reduced well below half of the Debye temperature.[17]

A simple model can be formulated to explain the observed results and to derive the microstructure-electrical property relationship in $W_{0.95}Ti_{0.05}O_3$ films. In order to do so, we must consider the simultaneous effect of Ti and T_s. It is clear from structural studies that the Ti incorporation induces the disordering, inhibits the crystal growth and increases the crystallization temperature. Therefore, a-$W_{0.95}Ti_{0.05}O_3$ films grown at T_s=RT–200 °C exhibit a lower electrical conductivity. The physics behind this must be the changes in the chemical bonding and the coordination environment of W. The ideal WO_3 crystal structure can be represented as a cubic ReO_3 structure.[17,18] Therefore, the structure is built up from a three-dimensional network of corner-sharing WO_6 octahedra.[17,18] XRD results indicate the formation of a small amount of the TiO_2 phase at T_s >400 °C. Therefore, the disordering in $W_{0.95}Ti_{0.05}O_3$ can be attributed to breaking the ordering of WO_6 octahedron by Ti via partial substitution for W atoms. The corner sharing Ti ions in WO_6 octahedra segregate to the surface upon increasing T_s, resulting in the formation of a TiO_2 phase. Clear evidence for this hypothesis is the broadening of the XRD peak for $W_{0.95}Ti_{0.05}O_3$ films grown at T_s=500 °C accompanied by a decrease in electrical conductivity. However, the initial rise in conductivity for $W_{0.95}Ti_{0.05}O_3$ films grown at T_s=RT–400 °C is due to improved structural order where the Ti distortion and segregation is not dominant.

Summarizing the results, $W_{0.95}Ti_{0.05}O_3$ films were fabricated using sputter-deposition and their structural and electrical properties were investigated. The disordering effect induced by Ti is evident in microstructure and electrical properties of $W_{0.95}Ti_{0.05}O_3$ films. The effect is pronounced by amorphization and elevating the crystallization temperature of $W_{0.95}Ti_{0.05}O_3$ films. The transformation is characterized by a transition from disordered to tetragonal structure. Associated with the disordering effect and structural transition, a marked difference in the temperature-dependence of conductivity is evident for a-$W_{0.95}Ti_{0.05}O_3$ films when compared to t-$W_{0.95}Ti_{0.05}O_3$ films. The crystal growth inhibiting effect of Ti can be useful to tailor the specific phase and size of WO_3 crystalline films for the desired applications.

This material is based upon work supported by the Department of Energy under Award No. DE-PS26-08NT00198-00.

[1]C. Bittencourt, R. Landers, E. Llobet, X. Correig, and J. Calderer, Semicond. Sci. Technol. **17**, 522 (2002).
[2]P. I. Gouma and K. Kalyanasundaram, Appl. Phys. Lett. **93**, 244102 (2008).
[3]D. Davazoglou and T. Dritsas, Sens. Actuators B **77**, 359 (2001).
[4]Dy Lu, J. Chen, H. J. Chen, J. Gong, S. Z. Deng, N. S. Xu, and Y. L. Liu, Appl. Phys. Lett. **90**, 041919 (2007).
[5]R. Ionescu, E. Llobet, J. Brezmes, X. Vilanova, and X. Correig, Sens. Actuators B **95**, 177 (2003).
[6]Y. Zhang, S. H. Lee, A. Mascarenhas, and S. K. Deb, Appl. Phys. Lett. **93**, 203508 (2008).
[7]M. Ferroni, V. Guidi, G. Martinelli, P. Nelli, and G. Sberveglieri, Sens. Actuators B **44**, 499 (1997).
[8]S. K. Gullapalli, R. S. Vemuri, and C. V. Ramana, Appl. Phys. Lett. **96**, 171903 (2010).
[9]N. Bundaleski, S. Petrovic, D. Perusko, J. Kovac, and A. Zalar, Appl. Surf. Sci. **254**, 6390 (2008).
[10]S. K. Gullapalli, R. S. Vemuri, F. S. Manciu, J. L. Enriquez, and C. V. Ramana, J. Vac. Sci. Technol. A **28**, 824 (2010).
[11]I. Bakonyi, E. Toth-Kadar, T. Tarnoczi, L. Varga, A. Cziraki, I. Gerocs, and B. Fogarassy, Nanostruct. Mater. **3**, 155 (1993).
[12]L. Wu, W. Tien-Shou, and W. Chung-Chuang, J. Phys. D: Appl. Phys. **13**, 259 (1980).
[13]C. V. Ramana, R. J. Smith, and C. M. Julien, J. Vac. Sci. Technol. A **22**, 2453 (2004).
[14]N. F. Mott and E. A. Davis, *Electronic Processes in Non-Crystalline Materials*, 2nd ed. (Clarendon, Oxford, 1979).
[15]S. Ambily and C. S. Menon, Thin Solid Films **347**, 284 (1999).
[16]Y. Z. Wang, G. W. Qiao, X. D. Liu, B. Z. Ding, and Z. Q. Hu, Mater. Lett. **17**, 152 (1993).
[17]C. V. Ramana, S. Utsunomiya, R. C. Ewing, C. M. Julien, and U. Becker, J. Phys. Chem. B **110**, 10430 (2006).
[18]T. Vogt, P. M. Woodward, and P. A. Hunter, J. Solid State Chem. **144**, 209 (1999).